Master's thesis

NTNU
Norwegian University of Science and Technology
Faculty of Natural Sciences
Department of Materials Science and Engineering

Maria Amundsen Mustaparta

Multilayer Coated Aluminium Bipolar Plates for Light-weight Fuel Cells

Master's thesis in Chemical Engineering and Biotechnology
Supervisor: Frode Seland
Co-supervisor: Katie McCay and Sigrid Lædre
June 2022

NTNU
Norwegian University of Science and Technology

Maria Amundsen Mustaparta

Multilayer Coated Aluminium Bipolar Plates for Light-weight Fuel Cells

Master's thesis in Chemical Engineering and Biotechnology
Supervisor: Frode Seland
Co-supervisor: Katie McCay and Sigrid Lædre
June 2022

Norwegian University of Science and Technology
Faculty of Natural Sciences
Department of Materials Science and Engineering

NTNU
Norwegian University of
Science and Technology

Preface

This master's thesis is written during the spring semester of 2022 as part of the course "TMT4900 - Materials Chemistry and Energy Technology, Master's Thesis". The thesis is submitted to the Norwegian University of Science and Technology, NTNU, as the final examination of the MSc degree in Chemical Engineering and Biotechnology.

First of all, I would like to express my thanks to Professor Frode Seland, my supervisor during this work. Thank you for always being available, for your inputs and support during the semester. To my co-supervisors, Dr. Katie McCay and Dr. Sigrid Lædre, thank you so much for helping me interpret the results and providing me with feedback. You guys make a great supervisor team!

The work performed during this thesis builds on the work carried out by the author from August 2021 to December 2021 as part of the specialisation project. The work described in this thesis has been performed from January 2022 to June 2022. Experimental work has been carried out at laboratories at the Department of Materials Science and Engineering, NTNU NanoLab and SINTEF. Thanks to Marit Stange and Abdulla Bin Afif, who have helped me prepare some of the samples. I appreciate your contribution.

I am grateful for all my fellow students and technical staff working in the corrosion lab in chemistry building 2. The long days in the lab would not have been the same without you. Finally, I want to thank Eirik and my family for always supporting me and giving me extra motivation when needed.

I, Maria Amundsen Mustaparta, declare that the work described in this report has been done in accordance with the regulations at NTNU.

Trondheim, June 2022.

Maria A Mustaparta

Abstract

The modern world's biggest challenge is keeping within the limits of acceptable global warming. Hence, the emission of greenhouse gases must be reduced. Air traffic is a massive contributor to greenhouse gas emissions worldwide. One of the most promising green energy solutions is the proton exchange membrane fuel cell. Making this technology the next generation aircraft engines can reduce air traffic pollution considerably. The main challenge is reducing the total fuel cell weight.

In this work, a multilayer coating for aluminium bipolar plates has been developed as a low-weight alternative to traditional stainless steel bipolar plates used in proton exchange membrane fuel cells. Stainless steel bipolar plates can account for up to 80% of the weight of a fuel cell stack, and if fuel cells are to be used in hard-to-decarbonise sectors like aircraft, a large weight reduction is required. Therefore, a light-weight metal such as aluminium is a promising bipolar plate material. However, uncoated aluminium is not stable in the proton exchange membrane fuel cell environment and does not fulfil the conductivity requirement due to oxide formation when exposed to air. Thus, this work has focused on developing corrosion resistant and highly conductive multilayer coatings on aluminium.

Various coating techniques such as electron beam evaporation, magnetron sputtering, and atomic layer deposition have been performed to apply the individual layers of the multilayer coating. The coatings were studied using scanning electron microscopy, and their corrosion resistance was tested in a simulated proton exchange membrane fuel cell environment. The contact resistance of each sample was measured before and after corrosion tests.

Interfacial contact resistance measurements demonstrated that aluminium coated with either titanium or titanium nitride and gold, before corrosion tests, could meet the area specific resistance target (below 10 mΩ cm^2) outlined by the U.S. Department of Energy before corrosion tests. However, scanning electron microscopy showed that the pretreatment procedure led to an uneven surface with multiple pits. Thus, it was hard to obtain complete coating coverage and defect-free coatings. The exposed aluminium substrate led to high current densities and coating failure during linear sweep voltammetry and chronoamperometry in pH 3 electrolyte heated to 70°C, at relevant fuel cell potentials. Aluminium coated with titanium nitride showed the highest corrosion resistance

with a current response below 1 µA cm^{-2} after 24 hours at 1 V. However, this sample did not meet the area specific resistance target.

Further work should focus on further development of titanium nitride coatings, which showed promising corrosion properties but high contact resistances. Additionally, investigating different coating techniques to achieve defect-free coatings would improve the coating longevity. Finally, adjusting the test conditions to more closely match the actual surroundings the bipolar plates experience inside an operating fuel cell would give a more realistic result.

Sammendrag

Den moderne verdens største utfordring er å holde seg innenfor grensen for akseptabel global oppvarming. Klimagassutslipp må derfor reduseres. Flytrafikk er en enorm bidragsyter til klimagassutslipp i hele verden. Proton-utveksling membran brenselceller er en av de mest lovende grønne energiløsningene. Ved å gjøre denne teknologien til neste generasjons flymotorer vil klimagassutslipp innenfor flytrafikk kunne reduseres betraktelig. Hovedutfordringen med brenselceller er å redusere deres totale vekt.

Det har i løpet av dette arbeidet blitt utviklet et flerlagsbelegg for aluminium bipolare plater som et lettvekts alternativ til de tradisjonelle bipolare platene laget av rustfritt stål. Når flere brenselceller kobles i serie, kan de bipolare platene laget av rustfritt stål være ansvarlig for opptil 80% av den totale vekten. Dersom brenselceller skal implementeres i fly, krever dette en kraftig vektreduksjon. Derfor er et lettmetall som aluminium et lovende bipolart platematerial. Ubelagt aluminium er imidlertid ikke stabilt i protonutvekslingsmembranbrenselcellemiljøet og oppfyller ikke konduktivitetskravet på grunn av oksiddannelse når det kommer i kontakt med luft. Dette arbeidet har derfor fokusert på å utvikle korrosjonsbestandige og svært ledende flerlagsbelegg på aluminium.

Ulike belegningsteknikker som elektronstrålefordamning, sputterdeponering og atomlagsdeponering har blitt benyttet for å påføre de ulike lagene av flerlagsbelegget. Beleggene ble studert i elektronmikroskop og deres korrosjonsmotstand ble testet i et simulert protonutvekslingsmembranbrenselcellemiljø. Kontaktmotstanden til hver prøve ble målt før og etter korrosjonstester.

Kontaktmotstandsmålinger viste at aluminium belagt med enten titan eller titannitrid og gull, før korrosjonsmålinger, møtte kontaktmotstandsmålet (under 10 mΩ cm^2) utnevnt av det amerikanske energidepartementet. Undersøkelse ved bruk av elektronmikroskopi viste imidlertid at forbehandlingsprosedyren førte til en ujevn overflate med mange groper. Dermed var det vanskelig å oppnå belegg som dekket overflaten helt og var uten defekter, og enkelte deler av aluminiumssubstratet ble eksponert til elektrolytt. De eksponerte delene av aluminiumssubstratet førte til høye strømtettheter og beleggssvikt under lineær sveipevoltammetri og kronoamperometri i pH 3 elektrolytt varmet opp til 70°C, ved relevante brenselcellepotensialer. Aluminium belagt med titannitrid viste den høyeste korrosjonsmotstanden med en strømrespons under 1 µA cm^{-2} etter 24 timer ved 1 V. Denne prøven var imidlertid ikke i stand til å oppnå kontaktmostand innenfor kontakt-

motstandsmålet.

Videre arbeid bør fokusere på å videreutvikle titannitridbelegg som viste lovende korrosjonsegenskaper, men høy kontaktmotstand. I tillegg vil det å undersøke forskjellige beleggningsteknikker for å oppnå belegg uten defekter forbedre beleggets levetid. Det å justere testforholdene slik at de samsvarer bedre med de faktiske omgivelsene de bipolare platene utsettes for i en brenselcelle under drift, vil kunne gi et mer realistiske resultater.

Abbreviations

Abbreviations	Description
ALD	Atomic Layer Deposition
BPP	Bipolar Plate
CA	Chronoamperometry
CE	Counter Electrode
CV	Cyclic Voltammetry
DI	Deionised Water
DOE	U.S. Department of Energy
EDS	Energy-dispersive X-ray Spectroscopy
GDL	Gas Diffusion Layer
HER	Hydrogen Evolution Reaction
ICR	Interfacial Contact Resistance
LSV	Linerar Sweep Voltammetry
MEA	Membrane Electrode Assembly
OCP	Open Circuit Potential
ORR	Oxygen Reduction Reaction
PEM	Proton Exchange Membrane
PEMFC	Proton Exchange Membrane Fuel Cell
RE	Reference Electrode
RHE	Reversible Hydrogen Electrode
SEM	Scanning Electron Microscopy
SHE	Standard Hydrogen Electrode
WE	Working Electrode

Nomenclature

Symbol	Description	Unit
A	Interfacial contact area	m^2
E	Potential	V
I	Current	A
i	Current density	A cm^{-2}
i_0	Exchange current density	A cm^{-2}
R	Areal specific resistance	mΩ cm^2
V	Voltage	V

Table of Contents

Chapter 1

Introduction

1.1 Background and Motivation

Increased population and a higher standard of living have led to an increased energy demand today compared to half a century ago. Today's lifestyle involves booking a flight whenever suitable and ordering goods online when desired. At the same time, there is an increasing focus on greenhouse gas emissions related to fossil fuel vehicles, and an energy transition is necessary to reduce such emissions. Fuel cells can produce zero-emission energy and therefore be part of the solution. Different types of fuel cells are available on the market. The Proton Exchange Membrane Fuel Cell (PEMFC) is an excellent alternative to traditional fossil fuel-based engines. It has a low operating temperature and thus fast response time, which is a vast advantage in applications with dynamic power demands, such as vehicles. PEM fuel cells utilise the attractive energy density of hydrogen, together with oxygen from the air to produce electrical energy. The only by-product is water, meaning this is an excellent zero-emission alternative.

Fuel cells have already been implemented in cars, buses, boats, trucks, and trains [1]. However, the use of fuel cells in large aeroplanes has not been demonstrated. Air traffic is a huge contributor to greenhouse gas emissions worldwide. At the same time, the global international aviation emissions are forecasted to grow by 200-700% between 2020 and 2050 [2]. It is therefore desirable to replace traditional aircraft engines with a green alternative. Batteries are too heavy for aeronautical applications and have a limited range. On the other hand, fuel cells might meet the weight requirements and can run as long as fuel is present.

A fuel cell is built up of several components. Among these are the Bipolar Plates, BPPs. The bipolar plates play a crucial role as they connect individual cells, distribute reactant gases, collect electrons and heat as well as provide stack structural integrity [3, 4]. They also transport the produced water out of the cell. Due to the many different roles of the BPPs, finding a suitable material that fulfils all requirements is challenging. Metal

substrates, e.g. stainless steels, are promising due to their high conductivity, formability, and low gas permeability. However, the passive layer commonly formed on metals leads to a reduction in conductivity performance over time. Current research has focused on modifying the passive layer on stainless steel with corrosion resistant and conductive coatings, such as Cr-N, Ti-N, Cr-C, amorphous carbon, or multilayer coatings [5]. Stainless steel bipolar plates can be responsible for up to 80% of the total fuel cell weight, making them too heavy for aeronautical applications [6]. Aluminium is a light-weight material, around three times lighter than stainless steel. Replacing stainless steel with aluminium for BPPs could reduce the fuel cell weight by 66%. Additional benefits are the cost of aluminium, which is two to three times cheaper than stainless steel, and the fact that aluminium is 20 - 45 times more conductive than stainless steel.

Due to an oxide layer that forms when exposed to the atmosphere, aluminium has excellent corrosion resistance in neutral environments. However, the oxide is electrically insulating and not stable in acidic environments with pH below 4.3 and high potentials, such as a typical PEMFC environment. Additionally, corrosion products are harmful to the fuel cell membrane and the catalyst layer, while the oxide will cause significant ohmic losses. Aluminium must therefore be coated. Furthermore, the coating must be corrosion resistant and highly conductive for aluminium to be considered a potential bipolar plate material for PEMFCs.

The U.S. Department of Energy, DOE, has in cooperation with the U.S. DRIVE Partnership developed technical targets for PEM fuel cell components [7]. When developing new fuel cell components, the targets are meant as guidelines when evaluating the progress without testing out full systems. The current status and technical targets for 2025 for bipolar plates are outlined in Table 1.1 [7, 8].

Table 1.1: Technical targets for BBPs, DoE [7, 8]

Characteristic	**Units**	**Status**	**2025 Target**
Cost	$\$/kW_{net}$	5.40	2
Plate weight	kg/kW_{net}	< 0.4	0.18
H_2 permeation coefficient	Std. $cm^3/(sec\ cm^2\ Pa)$	$< 2 \cdot 10^{-6}$	$2 \cdot 10^{-6}$
Corrosion, anode	$\mu A/cm^2$	no active peak	< 1 and no active peak
Corrosion, cathode	$\mu A/cm^2$	< 0.1	< 1
Electrical conductivity	S/cm	> 100	> 100
Areal specific resistance	$\Omega\ cm^2$	0.006	< 0.01
Flexural strength	MPa	> 34 (carbon plate)	> 40
Forming elongation	%	20-40	40

This thesis builds on the work described in the project report [9] with the same title carried out during the fall of 2021. The main focus during the project work was applying a multilayer coating consisting of a zinc adhesion layer, a titanium main coating layer

and a gold top layer on aluminium substrates. Experiments showed that the coating was able to meet the area specific resistance criteria outlined by the DOE (Table 1.1), but due to coating failure, high corrosion current densities were measured on all samples during electrochemical testing, and the interfacial contact resistance increased significantly. Furthermore, when applying titanium directly on aluminium, without the zincate process prior to deposition, coating failure was initiated later. Therefore, it was suggested that titanium failed to adhere well to the zinc layer. Further work suggested testing an alternative pre-treatment procedure, another type of adhesion layer, applying thicker coating layers and ensuring a tight sample holder.

1.2 Aim of Work

This work aims to develop a multilayer coating on aluminium bipolar plates in lightweight PEMFCs. The coating should be able to protect the aluminium surface from the aggressive fuel cell environment and, at the same time, obtain and maintain a minimal interfacial contact resistance. Therefore, the coating should consist of several layers to achieve a coating that does not degrade in a typical PEMFC environment while remaining highly conductive.

The oxide and other impurities on the aluminium surface will be removed by immersing the sample in an alkaline solution. After oxide removal, the next coating layer will be applied as soon as possible, performing various coating techniques. The coating layers should cover the aluminium substrates completely and be defect-free to avoid species penetrating the coating, thus causing corrosion of the underlying substrate that may lead to coating delamination. The main coatings should be titanium-based as titanium show excellent corrosion resistance, even at low pH and high potentials [10, 11]. Finally, a thin layer of gold will be deposited to facilitate high electrical conductivity during the lifetime of the bipolar plate.

The corrosion resistance of the samples will be tested using a three-electrode electrochemical cell designed to mimic the conditions inside an operating PEM fuel cell. Measured corrosion current densities below 1 $\mu A/cm^2$ are desired, and when performing potentiodynamic tests, no active peaks should be observed (Table 1.1). The contact resistance between the sample and the gas diffusion layer will be measured before and after corrosion tests to check if high electrical conductivity is achieved and maintained. At a compaction pressure of 140 N cm^2, the contact resistance should be lower than 10 $m\Omega$ cm^2 (Table 1.1). The surface characteristics of each layer and final coating solution will be investigated using scanning electron microscopy.

Chapter 2

Theory

2.1 Proton Exchange Membrane Fuel Cells

A fuel cell is a device that produces electrical energy from chemical energy. Compared to a conventional battery, the reactants are stored outside the cell, meaning a fuel cell can produce energy as long as it is fed with fuel and an oxidant [12]. Therefore, a fuel cell's performance is rated by its power output (kW). In an operating Proton Exchange Membrane Fuel Cell, PEMFC, the fuel is hydrogen, and the oxidant is oxygen, often in the form of air [13]. Hydrogen and oxygen gas are separated from each other by a proton-conducting but electronically insulating membrane [14]. During operation, hydrogen is oxidised while oxygen is reduced according to Eq. 2.1 and 2.2 respectively. The electrons are forced through an external circuit while the protons are conducted through the membrane.

$$\mathrm{H_2(g)} \rightleftharpoons 2\mathrm{H^+(aq)} + 2\mathrm{e^-}, \qquad E^\circ = 0 \text{ V} \tag{2.1}$$

$$\mathrm{O_2(g)} + 4\mathrm{H^+(aq)} + 4\mathrm{e^-} \rightleftharpoons 2\mathrm{H_2O\,(l)}, \qquad E^\circ = 1.23 \text{ V} \tag{2.2}$$

By combining Eq. 2.1 and 2.2, the overall reaction in a PEM fuel cell becomes

$$2\mathrm{H_2(g)} + \mathrm{O_2(g)} \rightleftharpoons 2\mathrm{H_2O\,(l)}, \qquad E^\circ = 1.23 \text{ V}. \tag{2.3}$$

Thus, the only by-product is water, making the fuel cell an excellent zero-emission engine. A simple sketch of a PEM fuel cell, summarising the working principle, is shown in Figure 2.1.

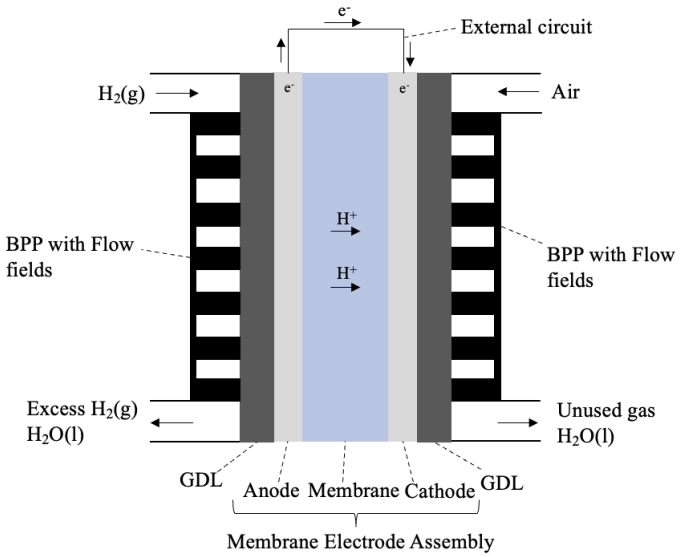

Figure 2.1: Illustration of the working principle in a proton exchange membrane fuel cell. Adapted from [15].

As seen in Figure 2.1, two essential parts of the fuel cell are the Membrane Electrode Assembly, MEA, and the Gas Diffusion Layer, GDL. The MEA consists of a proton exchange membrane with a catalyst layer on each side [16]. The MEA is the key component of the fuel cell where the electrochemical reactions take place. The membrane is usually made of Nafion™, a sulfonated tetrafluoroethylene-based fluoropolymer-copolymer. By ensuring a properly humidified membrane, high proton conductivity is obtained [17]. To force the electrons through the external circuit, the membrane should have low electron conductivity, and to minimise fuel crossover it should be impermeable to hydrogen gas.

As catalyst material, platinum is the most used for both anode and cathode. However, due to the high costs of platinum, it is used in the form of nanoparticles supported on carbon to achieve a high surface area and thus better utilisation of precious material [18].

The function of the GDL is to distribute reactant gases evenly on the MEA surface and provide an electrical connection between the bipolar plate and the catalyst. It is usually made of a porous carbon cloth or paper, to be able to transport the reactant gases into active sites and the produced water out of the cell while being electrically conductive both in-plane and through-plane [17].

At standard states and 25°C, the maximum theoretical output of a single fuel cell is 1.23 V, as can be seen from Eq. 2.3. In a real system, due to irreversibilities (losses), the output of a fuel cell is lower [12]. These irreversibilities include activation losses/overpotentials, ohmic losses, internal currents, fuel cross-over, and mass-transport losses [19]. Activation losses are related to the kinetics of the electrode reactions, especially oxygen reduction,

which is a slow reaction [12]. These losses are highest at low current densities since some of the produced voltage is used to transfer electrons to or from the electrode. Ohmic losses are resistance to electron flow through interfaces and bulk components in the cell and ions in the membrane [20]. Such losses obey Ohm's law and are therefore linearly proportional to the current density. Some electrons and small amounts of the fuel will pass through the membrane leading to losses known as internal currents and fuel cross over, but if the membrane is not damaged, these losses should be negligible [19]. As fuel and oxidant are consumed, the reactant concentrations on the electrode surfaces will vary, leading to reduced reaction rates [12]. These losses are referred to as mass-transport losses and are highest when the cell operates at low potentials or high current densities due to high reactant consumption.

2.2 Bipolar Plates

Due to the irreversibilities outlined in Section 2.1, the output of an individual fuel cell is usually around 0.7 V_{SHE} [21]. Thus, connecting several fuel cells in series, and making a fuel cell stack, is necessary to get the desired power output. When connecting several cells, the Bipolar Plates, BPPs, are essential as they collect and conduct current from the anode of one cell to the cathode of the adjacent cell [17]. The BPP material must therefore be highly conductive. A simplified fuel cell stack is shown in Figure 2.2.

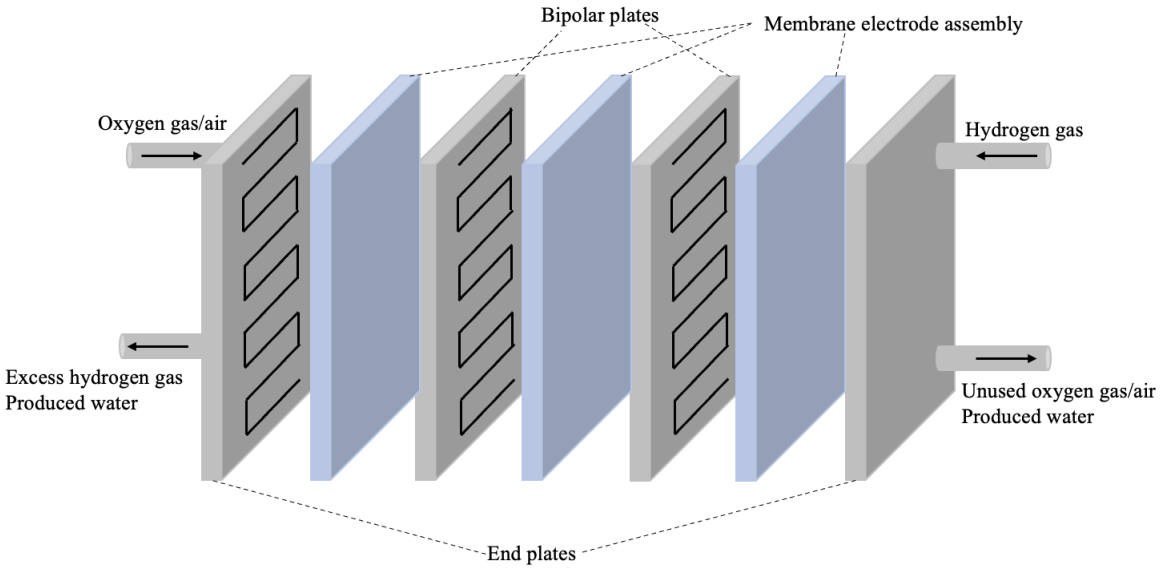

Figure 2.2: Fuel cell stack consisting of several individual cells. Adapted from [22].

Additionally, the BPPs provide mechanical stability and distribute hydrogen gas over the anode surface and air/oxygen over the cathode surface. To evenly and effectively distribute reactant gases over the electrode areas, the BPPs have flow fields of different

geometries etched or stamped into the surface [3]. A selection of different geometries is shown in Figure 2.3, where the parallel serpentine is very reliable, has a suitable pressure drop, and shows very good performance, which is why it is a preferred choice in many applications [23].

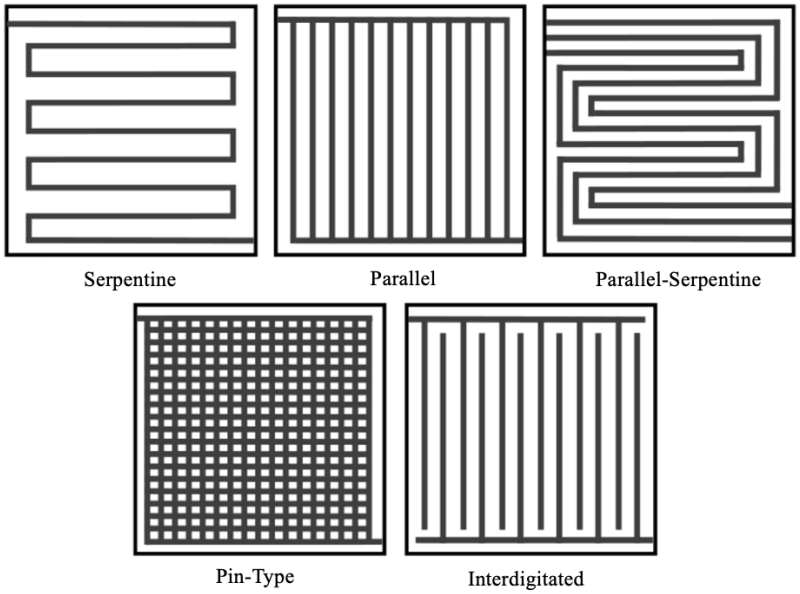

Figure 2.3: Illustrations of the most common BPP flow field patterns [24].

2.2.1 Materials for Bipolar Plates

Graphite has traditionally been the most commonly used bipolar plate material due to its chemical stability, and high electrical conductivity [25, 26]. However, due to its fragility and porosity, in addition to the production cost and poor manufacturability new BPP materials have been researched and investigated [27, 28, 29]. Among these are carbon polymer composites and metals [30]. It has proven to be challenging to find a suitable material that fulfils all BPP requirements. Graphite bipolar plates are still used as a standard when searching for, and testing other BPP materials [21, 25, 26]. An overview of different materials and coatings used as bipolar plate materials is given in Figure 2.4 [31].

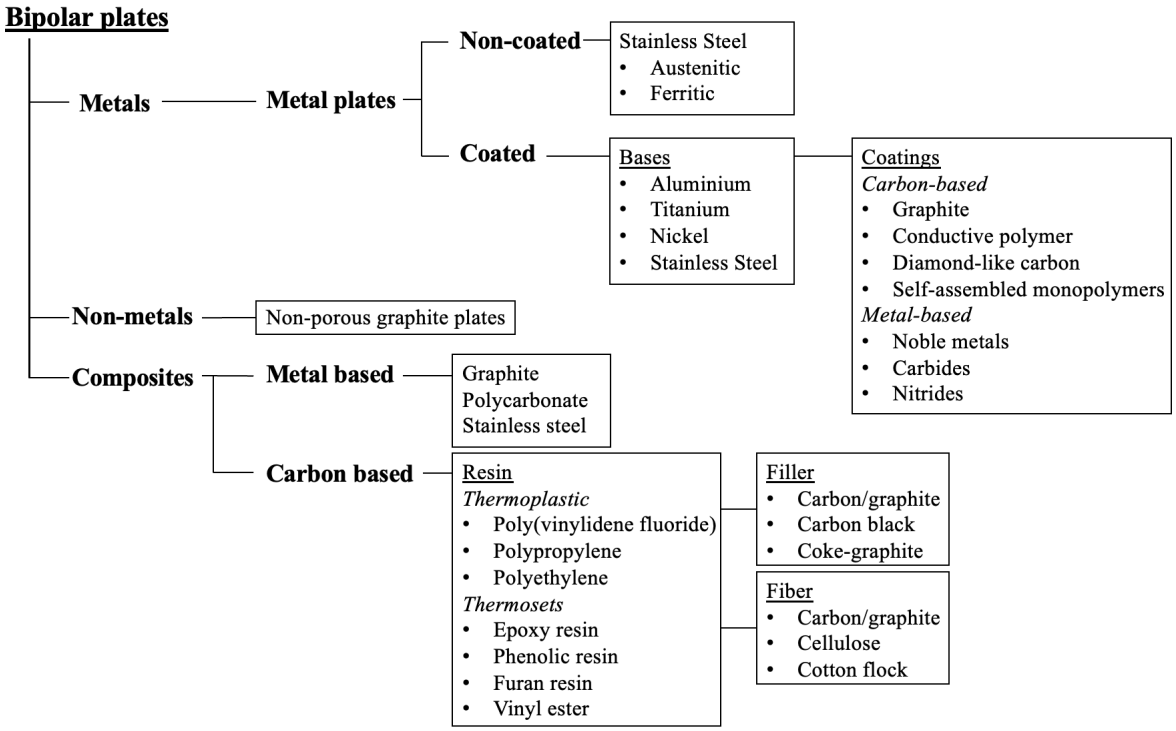

Figure 2.4: Overview of materials used in bipolar plates for PEM fuel cells. Adapted from [31].

Composite materials consist of a polymer matrix and a metal-based or carbon-based filler material. Composite bipolar plates are cheaper than graphite, show good corrosion resistance, and are relatively light [31]. The main challenge when it comes to composite materials is the compromise between mechanical stability and electrical conductivity [32].

Today, metallic materials with suitable surface modifications and/or coatings have received extensive attention in BPP research, especially stainless steel [21]. Metallic bipolar plates have many advantages, such as low gas permeability, good formability, high electrical and thermal conductivity, and low costs [27, 28]. For transport applications where mechanical shocks and vibrations have the potential to cause cracks and leakage of reactant gases, bipolar metal plates are advantageous due to their high mechanical stability [32]. However, a large drawback with metallic BPPs is their low stability in the humid PEM fuel cell environment which is acidic (pH 3-5) and warm (70-80°C). Under such conditions, many metals corrode, and the corrosion products can potentially poison the catalyst layer and the membrane and thus reduce the overall fuel cell performance [30]. Noble metals, such as gold and platinum, will not suffer from corrosion in the PEMFC environment but are too expensive for fuel cell applications [21, 30].

2.2.2 Aluminium Bipolar Plates

Since the bipolar plates can be responsible for up to 80% of the total fuel cell weight and around 25% of the total costs in a PEM fuel cell stack [6, 33], aluminium bipolar plates can be more suitable than stainless steel thanks to the low density, 2.7 g cm^{-3}, and the lower price of aluminium. Additionally, aluminium has high electrical conductivity, 36.9 $\cdot$ 10^6 S m^{-1}, compared to stainless steel with 1.32 $\cdot$ 10^6 S m^{-1} [34].

When implementing fuel cells in aeroplanes, where weight is a crucial factor, aluminium bipolar plates is a promising candidate. However, like stainless steel, the main challenge with aluminium is its stability in the PEM fuel cell environment [32, 35]. When exposed to the atmosphere, aluminium reacts spontaneously with oxygen and forms an insulating oxide, as can be seen from Eq. 2.4,

$$4\mathrm{Al(s)} + 3\mathrm{O_2(g)} \rightleftharpoons 2\mathrm{Al_2O_3(s)}. \tag{2.4}$$

The free energy of the reaction (Eq. 2.4) is -1675 kJ, explaining aluminium's high affinity toward oxygen [36]. The reaction between aluminium and oxygen is referred to as low-temperature oxidation since it takes place in the absence of an electrolyte where solid-state diffusion is negligible [37]. When the oxide thickness has reached a few nanometers, the oxide growth rate falls to practically zero. Aluminium oxide is, according to the Pourbaix diagram (Figure 2.7), chemically stable in mild acidic environments down to pH 4.3 but has a poor electronic conductivity [38].

For aluminium to meet the targets outlined by the U.S. DOE (Table 1.1), the oxide must be removed and replaced by a highly conductive and corrosion resistant coating. There are several examples of using coated aluminium as a bipolar plate material in PEM fuel cells.

Havigh et al. [39] applied a multilayer coating on aluminium consisting of titanium to obtain improved corrosion resistance and conductivity and amorphous carbon to postpone titanium oxidation and further improve the conductivity. The coatings were deposited applying magnetron sputtering, and the samples were tested in electrolytes adjusted to pH 2, 3, and 4. Their results showed that the OCP values for coated aluminium were more positive than those for uncoated aluminium in pH 2, 3, and 4. However, after 15 and 17 hours in electrolytes with pH 2 and 3 respectively, the OCP values for uncoated and coated aluminium were almost the same. The measured corrosion potentials for coated samples were higher for all pH values compared to bare aluminium, indicating that the coating did work as a protecting layer. However, the coating was removed entirely on the sample immersed in the electrolyte with pH 2 and partially on the sample immersed

in the pH 3 electrolyte. They concluded that coating failure was caused mainly by the acidity of the electrolyte and that defects in the coatings should be avoided as they have a detrimental effect on the coatings.

Marzo et al. [40] coated aluminium alloy AA7075 with Ni-P of different thickness, applied by electroless deposition. An additional layer of 10 µm chromium was applied on one of the samples, by electroplating on top of the Ni-P coating. Their results showed that the corrosion resistance decreased with increasing Ni-P coating thickness. The multilayer coating consisting of 20 µm Ni-P and 10 µm Cr showed the largest polarisation resistance although it contained micro-cracks, allowing electrolyte to reach the substrate surface and delaminate the coating. In addition, the chromium oxide layer that formed on the sample surface during corrosion tests led to a large increase in ICR.

Fetohi et al. [41] coated different aluminium substrates (pure Al, AA6061, AA3004, and AA1050) with Ni-Co-P using an electroplating power supply technique. Prior to coating deposition, they performed a double zincating process. Their results showed that Ni-Co-P coatings on pure Al and AA1050 greatly reduced the corrosion rate, while the effect on AA3004 and AA6061 was smaller. The reduced corrosion rate can be explained by the dense coatings formed on pure Al and AA1050. In contrast, the coatings on AA3004 and AA6061 contained visible cracks allowing the electrolyte to reach the aluminium substrate, causing corrosion. Potentiodynamic polarisation tests were performed at 25°C as well as at 70°C. The tests performed at elevated temperatures showed a significant increase in corrosion rate. Therefore, they concluded that Ni-Co-P coatings could not prevent different aluminium substrates from corrosion at elevated temperatures. Although Ni-Co-P coated AA1050 obtained a high corrosion rate at elevated temperature, Fetohi et al. concluded that it showed promising interfacial contact resistance with 27.05 mΩ cm^{-2} at 140 N cm^{-2}.

González Gutiérres et al. [42] looked into the zincating effect on corrosion resistance of electroless Ni-P coating on aluminium, AA6061. Prior to coating, a zincating process consisting of either a single, double or triple step was performed. The sample pre-treated with a triple zincating step showed improved corrosion resistance compared to those treated with a single and a double zincating step. Additionally, there was an increasing amount of phosphorous deposited on the sample with increasing number of zincating steps. This finding underpins the theory that increased phosphorous content increases the corrosion resistance made by other authors [43, 44, 45]. González Gutiérres et al. reported a measured corrosion current density of 4.4 µA cm^{-2} at a corrosion potential of -0.14 $V_{Ag/AgCl}$ on the triple zincated, coated aluminium sample. ICR measurements were not performed.

Although there are promising examples of coated Al BBPs in the literature, long-term

in-situ testing has not been performed. None of the above reported results meet the targets outlined by the DOE, and aluminium BPPs have therefore not yet been used in a commercial fuel cell.

2.3 Coating Metallic Bipolar Plates

Coating a metal surface is a way to obtain specific and desired properties, with the final surface properties determined by the type of substrate, pre-treatment procedure, coating technique, and the coating material. For metals, the coating is often a barrier to prevent water and oxygen from reaching the surface and thus avoid corrosion.

The main purpose of coating a metallic bipolar plate is to resist corrosion and remain highly conductive throughout the fuel cell lifetime [32]. The coating should cover the surface entirely and be defect-free. Proper adhesion between the substrate and the coating is essential and easier obtained if the substrate and the coating have similar coefficients of thermal expansion [21]. A large difference in thermal expansion coefficients could potentially lead to micro-cracks and micro-pores.

For metallic bipolar plates, commonly used coating materials are divided into carbon-based and metal-based coatings, as can be seen from Figure 2.4. The carbon-based coatings include graphite, conductive polymers, diamond-like carbon and self-assembled monopolymers, while metal-based coatings can be noble metals, carbides, and nitrides [31].

2.3.1 Coating Techniques

Several coating techniques can be used to coat metallic bipolar plates. Some techniques have limitations regarding deposition material, while others are prone to defects such as pinholes. Defects in coatings stop it from being a barrier to the electrolyte and may lead to accelerated coating degradation and initiate localised corrosion attacks [21]. This will harm the overall performance of the coated metallic BPP. The different coating techniques used during this work and their respective working principles are explained in this section.

Electron Beam Evaporation

Electron beam evaporation is a Physical Vapour Deposition, PVD, technique which involves vaporising the material desired to deposit, the source material, by using an electron beam [46]. The e-beam is generated by heating a tungsten filament up to around 2500°C such that electrons leave the surface of the filament. Magnets are then used to direct the beam towards the source material, which has to be electrically conductive [47]. Both the source material and the substrate are placed in a high vacuum chamber (10^{-6} - 10^{-7}

mbar). Multiple materials may be deposited on top of each other without breaking the vacuum since the source material is contained in a crucible, and an e-beam evaporator can have several pockets containing crucibles with different source materials. The final thin film usually contains grains as the film growth starts with small islands that grow. By rotating the sample during deposition, a more uniform film on the sample surface is obtained [47].

Sputtering

Sputtering is, like e-beam evaporation, a PVD technique. However, unlike e-beam, sputtering does not use evaporation but involves using energetic ions to knock atoms or molecules from a target/source material. While the target and the substrate are facing each other, acting as electrodes, in a sputtering chamber, an inert gas, typically argon, is introduced at a pressure of around 0.13 mbar [47]. By applying an electric field, or a dc voltage between the electrodes, the argon atoms are ionised, and positive argon ions, Ar^+, are attracted to the negatively charged target. Since the argon ions have a high speed when they hit the target, they physically knock off individual atoms on the target material [47]. These atoms deposit on the opposite electrode, the substrate, and the process can continue until the desired film thickness is achieved.

Magnetron sputtering is a modified sputtering technique. Magnets are placed behind the target resulting in a magnetic field that tarps the free electrons just above the target, meaning they can not bombard the substrate to the same extent as without the magnetic field [48]. Less bombardment of the substrate avoids overheating and structural damage of the substrate. Trapping these electrons also leads to increased ionising of the inert gas and thus accelerated eroding rate of the target material, resulting in an overall increase in deposition rate [48].

During sputtering, the substrate surface is activated through electron bombardment, while the substrate is not activated during electron beam evaporation. As a result, the resulting thin films deposited by e-beam evaporation contain large grains while the sputtered films are more fine-grained [47]. An additional advantage of sputtered thin films is the strong adhesion to the substrate [49]. However, both techniques require expensive equipment, high vacuum and high temperature.

Atomic Layer Deposition

Atomic Layer Deposition, ALD, is a Chemical Vapour Deposition, CVD, method. Compared to PVD, CVD involves a chemical reaction between the substrate and the deposition material. ALD is a deposition technique that offers excellent thickness control as only one atomic or molecular layer can grow on the substrate at once [47]. The process starts

with activating the substrate surface chemically. Precursors are then introduced into the deposition chamber, interacting with the active surface and forming chemical bonds with the substrate. The precursors do not interact with each other and react only with unreacted areas on the substrate, meaning one single layer of atoms/molecules is deposited during each cycle, and the deposited film is pinhole free [50]. A schematic illustration showing one cycle of titanium oxide film growth by ALD is shown in Figure 2.5. For the next cycle, the surface is reactivated and the precursor reintroduced into the deposition chamber.

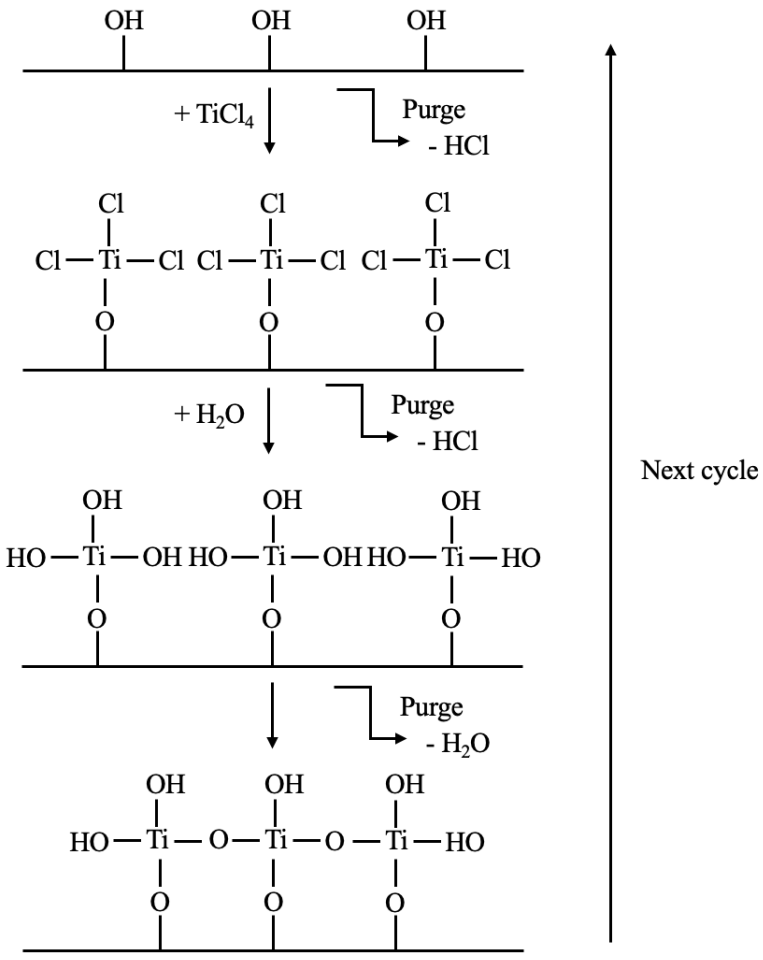

Figure 2.5: Schematic illustration of titanium oxide film growth by ALD. Adapted from [47].

2.3.2 Coating Aluminium

This work suggests a multilayer coating on aluminium, consisting of a pre-treatment procedure and multiple individual layers by performing the techniques described in Subsection 2.3.1. The final coating is believed to be able to withstand the conditions inside a PEM fuel cell without suffering from major harmful effects while being electrically conductive.

During the specialisation project [9], the main challenge was coating failure during electrochemical testing. Therefore, this work's main focus is achieving a coating that does not fail during long-term electrochemical testing. The pre-treatment procedure and the different individual layers are described in the following subsections.

Pre-treatment of Substrates and Adhesion Layer

The spontaneously formed oxide on pure aluminium, Al_2O_3, is electrically insulating, porous and has a non-uniform thickness [37]. The non-uniform thickness makes it hard to obtain an uniform coating on aluminium as well as achieve good adhesion [42]. Therefore, this layer must be removed. By immersing aluminium in an alkaline solution, hydroxides attack the aluminium oxide at the oxide film/solution interface. Thus, the oxide will dissolve chemically according to Eq. 2.5 [51].

$$Al_2O_3(s) + 2OH^-(ad) \rightleftharpoons 2AlO_2{}^-(aq) + H_2O\,(l) \tag{2.5}$$

While the aluminium oxide dissolves, there will be a simultaneous formation and dissolution of an aluminium hydroxide film. Hydroxide ions migrate through the oxide layer to the aluminium/oxide interface resulting in film formation according to reaction Eq. 2.6 [52]. On the other hand, hydroxide ions attack the aluminium hydroxide film, resulting in a breakdown of the film according to reaction Eq. 2.7 [52].

$$Al\,(s) + 3\,OH^-(aq) \rightleftharpoons Al(OH)_3(s) + 3\,e^- \tag{2.6}$$

$$Al(OH)_3(s) + OH^-(aq) \rightleftharpoons Al(OH)_4{}^-(aq) \tag{2.7}$$

By combining Eq. 2.6 and 2.7, reaction Eq. 2.8 is obtained, showing how aluminium dissolves in alkaline solution [52].

$$Al\,(s) + 4OH^-(aq) \rightleftharpoons Al(OH)_4{}^-(aq) + 3e^-. \tag{2.8}$$

The corresponding reduction reaction will mainly be reduction of water resulting in hydrogen gas evolution according to reaction Eq. 2.9 [51].

$$2H_2O\,(l) + 2e^- \rightleftharpoons H_2(g) + 2OH^-(aq) \tag{2.9}$$

By combining Eq. 2.8 and 2.9, the overall reaction of aluminium dissolution in alkaline media becomes [53],

$$2\mathrm{Al(s)} + 6\mathrm{H_2O\,(l)} + 2\mathrm{OH^-(aq)} \rightleftharpoons 2\mathrm{Al(OH)_4{}^-(aq)} + 3\mathrm{H_2(g)}. \tag{2.10}$$

Factors such as pH, the concentration of reactants, aluminium composition, presence of anions and surface treatment prior to alkaline treatment will all affect the reaction mechanism [51]. After alkaline treatment and exposure to the atmosphere, the oxide layer on aluminium will reform.

Zincating is a widely used surface treatment procedure on aluminium. It is a dipping process involving aluminium oxide dissolution and zinc deposition, according to Eq. 2.11 [54], to avoid the reformation of the oxide when exposed to the atmosphere.

$$3\mathrm{Zn(OH)_4{}^{2-}(aq)} + 2\mathrm{Al(s)} \rightleftharpoons 2\mathrm{AlO_2{}^-(aq)} + 3\mathrm{Zn\,(s)} + 4\mathrm{H_2O\,(l)} + 4\mathrm{OH^-(aq)}. \tag{2.11}$$

The zincating process commonly includes a double zincating step with an acidic stripping between the two steps [55]. González Gutiérres et al. [42] investigated the effect of the zincating process on corrosion resistance of electroless Ni-P coating on aluminium. Their results showed that the corrosion resistance was further improved by performing a third zincating step. SEM pictures showed an uniform, thin and tight honeycombed structure covering the aluminium surface after performing a third zincating step. Furthermore, EDS analysis showed that the amount of zinc was lower when performing a third dipping step compared to a double. This indicates a thinner zinc layer. Also, the oxygen content decreased as a third step was completed, implying enhanced aluminium oxide removal by performing a third zincating step [55].

Main Coating Layer

The main coating layer should be corrosion resistant in the PEM fuel cell environment and remain conductive during the BPP lifetime. Titanium is known for its excellent corrosion properties, which can withstand acidic and chlorine-containing environments [56]. Additionally, titanium has a low density, 4.53 g $\mathrm{cm^{-3}}$, and is, like aluminium, regarded as a light-weight metal. Titanium's corrosion resistance is obtained through the formation of an oxide layer, so high electrical conductivity must be maintained through the application of a top layer. Titanium ions have, however, shown to have a less detrimental effect on the proton exchange membrane and the catalyst layer compared to iron, chromium etc. ions from stainless steel [57]. Titanium is, therefore, a potential light-weight bipolar plate

material. However, the costs of titanium, as well as the high time consumption and costs associated with fabrication due to the inherent hardness in addition to the insulating properties of the oxide layer, are limiting factors [39, 58].

During this work, metallic titanium will be deposited by performing electron-beam evaporation and magnetron sputtering. Titanium oxide will be deposited by atomic layer deposition while titanium nitrite will be deposited by performing magnetron sputtering.

Top Layer

Finally, the main coating layer must be partially covered by a thin top layer of a highly conductive metal such as gold in order to suppress oxide formation and obtain sustained electrical conductivity.

Material Properties

The multilayer coating will consist of titanium, titanium oxide, titanium nitride, aluminium oxide, zinc and gold in different combinations. Coefficients of linear expansion and electrical resistivities of these materials are given in Table 2.1.

Table 2.1: Coefficient of linear expansion and electrical resistivity of selected materials [38, 34].

Element	**Coefficient of linear expansion [/°C]**	**Electrical resistivity [Ω m]**
Al	$24 \cdot 10^{-6}$ [34]	$2.4 \cdot 10^{-8}$ [38]
Al_2O_3	-	$> 10^{13}$ [59]
Au	$14.4 \cdot 10^{-6}$ [34]	$2.1 \cdot 10^{-8}$ [38]
Ti	$8.9 \cdot 10^{-6}$ [34]	$39 \cdot 10^{-8}$ [38]
TiN	$10.3 \cdot 10^{-6}$ [60]	$4 \cdot 10^{-3}$ [61]
TiO_2	-	29 - 910 [38]
Zn	$31.2 \cdot 10^{-6}$ [34]	$5.5 \cdot 10^{-8}$ [38]

2.4 Degradation of Coated Metallic BPPs

To be able to predict the durability and understand the degradation mechanisms of bipolar plates inside an operating PEM fuel cell, it is crucial to understand the environment they are exposed to. The fuel cell environment and an introduction to corrosion of metals particularly focused on aluminium and coating failure, are explained in the subsequent subsections.

2.4.1 The Fuel Cell Environment

The potential on the anode side of the cell differs from that on the cathode side. The bipolar plates will therefore experience different potentials [17]. In theory, the potential on the anode side should be equal to that of hydrogen oxidation, while the potential on the cathode side should be equal to the reduction potential of oxygen. However, in reality, due to losses described in Section 2.1, this is not the case.

At low currents, the activation overpotentials dominate. For a given reaction, the activation overpotential is strongly dependent on the exchange current density of that reaction on a material [62]. Further, there is a strong relationship between the exchange current density and the reaction kinetics, and the exchange current density on the cathode is around five orders of magnitude lower than that on the anode [12]. The overpotential on the anode is thus negligible, and the bipolar plate will experience a voltage equal to the reversible potential of hydrogen oxidation. The bipolar plate on the cathode side will be exposed to a potential equal to that of oxygen reduction minus the activation overpotential when current is drawn from the fuel cell.

The humidity inside the fuel cell is carefully controlled since flooding is a threat and should be avoided. Humidity is, however, essential in achieving proper proton conductivity of the proton exchange membrane [17]. The exact pH within an operating fuel cell is difficult to measure. However, it is expected to be acidic due to the Nafion-membrane, a sulfonated fluoropolymer with SO_3^- side chains that attract protons and water and create a dilute acid [17]. The operating temperature is usually around 70-80°C [31].

Thus, the bipolar plates are exposed to varying potentials, aqueous, acidic and warm conditions during operation. Metals are especially prone to corrosion, and the humidity gives rise to aqueous corrosion.

2.4.2 Corrosion of Metals

It is well known that most metals corrode. Corrosion can be defined as an attack on a metallic surface by a reaction with the surrounding media [63]. The overall reaction consists of an oxidation and a reduction and is referred to as a charge-transfer reaction. This can be illustrated with an Evans diagram shown in Figure 2.6. The green and orange curves represent hydrogen evolution and oxygen reduction, respectively, while the black curve is the oxidation of an active-passive metal. If oxygen is present, the oxygen reduction reaction is the dominating cathodic reaction until the intersection between the green and orange curve (*). After this point, hydrogen evolution becomes the dominating reduction reaction.

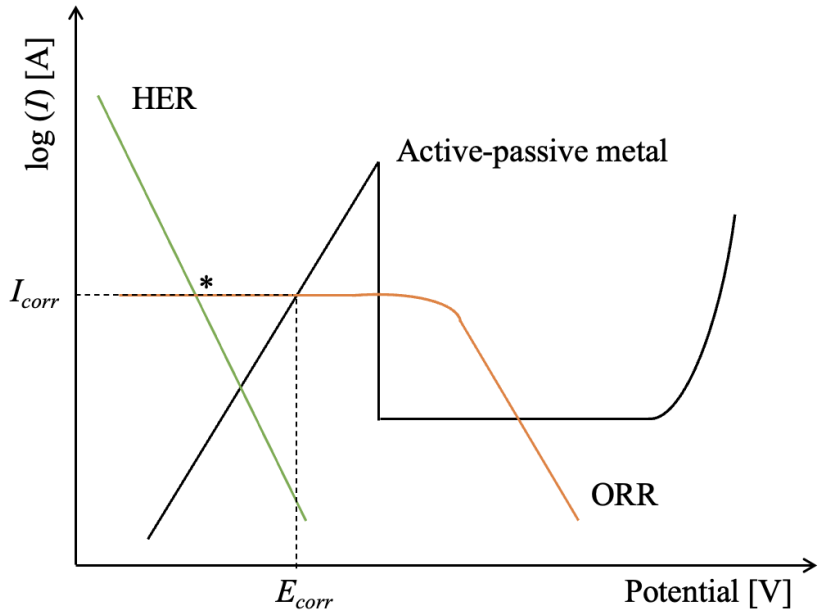

Figure 2.6: Evans diagram, showing the hydrogen evolution reaction, HER (green line), the oxygen reduction reaction, ORR (orange curve), and the theoretical oxidation curve of an active-passive metal (black curve).

A potential-pH (Pourbaix) diagram can give useful information about a specific metal making it possible to predict if the metal will corrode or not at a given potential and pH interval. Such a diagram can be constructed for a given metal if thermodynamic data such as the standard free energies ($\Delta_f G^\circ$) or the standard reduction potentials (E°), as well as all possible charge-transfer reactions leading to metal dissolution are known [64]. The software "HSC Chemistry" is used to construct the Pourbaix diagram for aluminium at 70°C, and the diagram is shown in Figure 2.7. The horizontal lines represent purely electrochemical reactions, only involving electrons. Vertical lines represent purely chemical reactions, involving either H^+ or OH^- depending on the pH of the surrounding media. Diagonal lines, with a positive or negative slope, depend on pH and potential as they involve both electrons and H^+/OH^-. The reversible potential of hydrogen and oxygen is represented by the lower and upper dashed lines, respectively.

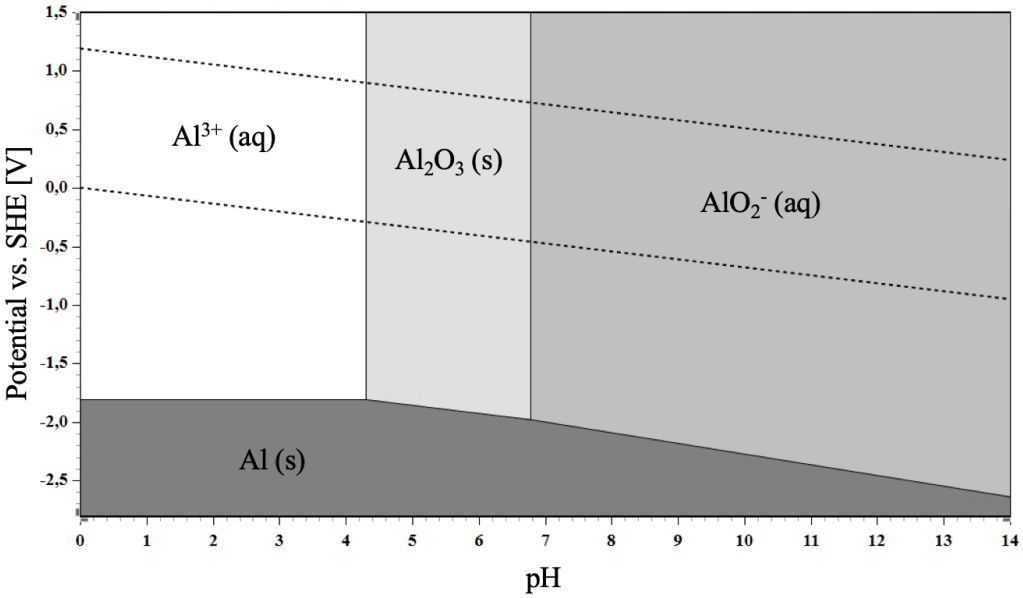

Figure 2.7: Pourbaix diagram for aluminium. The diagram is calculated for a temperature of 70°C and an activity of dissolved species equal to 10^{-6} mol L^{-1}. The software "HSC Chemistry" is used to construct the Pourbaix diagram.

The dark grey area, marked "Al (s)", is the potential-pH range where aluminium is immune to corrosion. The white and grey areas marked with aqueous ions indicate under which potential and pH values aluminium is actively corroding, while the light grey area, marked "Al_2O_3 (s)", shows when the passivating oxide is stable [64]. Therefore, aluminium is expected to actively corrode when exposed to a typical PEM fuel cell environment at pH 3 and potentials between 0 - 1 V.

Localised Corrosion

Corrosion attacks can either be uniform or local. Localised corrosion occurs when the metal, according to the Pourbaix diagram, has obtained a passive film on its surface. Corrosion then occurs at a small, confined area of the sample surface where the passive film is incomplete [64]. There are several types of localised corrosion, such as pitting corrosion, crevice corrosion, selective corrosion, intergranular corrosion and layer/exfoliation corrosion.

The mechanisms of pitting, crevice and selective corrosion vary to some extent, but all of them are initiated at weakened oxide spots (flaws). Flaws can be a result of mechanical (scratches, cracks or slip planes introduced by external factors or internal stresses) or microstructural (inclusions on the surface) factors. For media not containing chlorides or other halides, pitting corrosion is generally not observed [65].

Intergranular corrosion is a form of localised corrosion taking place on grain boundaries, and exfoliation is a special case of intergranular corrosion occurring on metals that, due to rolling or extrusion, have a flat grain structure [64]. The origin of intergranular corrosion is the difference in corrosion potential between the grain and the grain boundary. For example, iron impurities in aluminium give rise to Fe_3Al-particles that are more electropositive than the aluminium grains [56]. The Fe_3Al-particle becomes cathodic compared to aluminium which becomes anodic, leading to a micro cell where galvanic corrosion occurs. Exfoliation corrosion is recognised by thin sheets of material peeling off like pages in a book because corrosion products push different planes away from each other [36, 64].

2.4.3 Coating Failure

Coating failure is usually initiated by a coating damage or poor adhesion between the coating material and the substrate. In these situations, water can easily reach the coating/substrate interface and react with the substrate. Reaction products push the coating upwards, resulting in weakened adhesion between the coating and the substrate. This is a typical coating failure mechanism for coatings submerged in water or in the ground. Applying multiple coats and/or thicker coatings can reduce this effect.

Another coating failure mechanism can come from galvanic corrosion. In the case of Al, the reversible potential is low (Figure 2.7), and aluminium will in contact with a more noble metal act as a sacrificial anode. If there is a coating damage when coating aluminium with a more noble metal, a small area of aluminium will be exposed to the corrosive medium. Thus, the area of the anode will be much smaller than the cathodic area, resulting in a very high corrosion rate of the anode material, aluminium, which can lead to pinholes [64].

2.5 Bipolar Plate Testing

To compare and measure the performance and long-term stability of bipolar plates, the U.S. Department of Energy, DOE, has established a set of targets and requirements. The targets are developed in cooperation with the U.S DRIVE Partnership and are summarised in Table 1.1. They are meant as guidance for developers and include test methods and targets for both ex-situ (in a simulated fuel cell environment) and in-situ (in an operating fuel cell) testing [7].

2.5.1 Interfacial Contact Resistance Measurements

Between each fuel cell component, there will be a contact resistance contributing to the total contact resistance. The contribution from the bipolar plate/gas diffusion layer interface is particularly important [24]. The interfacial contact resistance is influenced by surface roughness, oxide layer and pressure and should be as low as possible in order to minimise ohmic losses in the fuel cell.

The contact resistance is measured using a standardised method, based on the work done by Wang et al. [66]. A BPP sample with a GDL on top is placed between two gold coated copper plates. A constant current is applied through the sample while a variable pressure is applied, and the resulting voltage is measured. The area specific resistance, R, can then be calculated by Ohm's law,

$$R(\mathrm{m\Omega\ cm^2}) = \frac{V(\mathrm{mV})}{I(\mathrm{A})} A(\mathrm{cm^2}), \tag{2.12}$$

where V is the measured voltage, I is the applied current and A is the area of the interfacial contact. When measuring the resistance using this method, all contact resistances in the system are combined in the measured voltage drop. In order to isolate the BPP/GDL contact resistance from the GDL/top plate contact resistance, GDL bulk resistance and other resistances in the wires and system, the ICR of a single GDL is measured and subtracted from the measured ICR of the total system.

In order to meet the targets outlined by DOE, the interfacial contact resistance should be lower than 10 $\mathrm{m\Omega\ cm^2}$ at the standard compaction pressure of 140 $\mathrm{N\ cm^{-2}}$ for ex-situ testing [7].

2.5.2 Electrochemical Measurements

The electrochemical behaviour of bipolar plates is important to investigate in order to get an estimate of their durability and longevity. For metallic bipolar plates, the largest concern is their degradation in form of corrosion in the harsh PEMFC environment [30]. Ex-situ testing includes simple and cheap tests that can be performed to predict the bipolar plate's behaviour before possibly testing it in-situ. The guidelines from the U.S. DOE include test conditions such as electrolyte pH, temperature and voltage ranges in order to mimic an operating PEMFC [7]. However, some notable differences exist between the ex-situ testing conditions and the in-situ environment.

Open Circuit Potential (OCP), Linear Sweep or Cyclic Voltammetry (LSV or CV) and Chronoamperometry (CA) are among the most commonly used electrochemical methods

for bipolar plates. The experimental setup consists of a three-electrode electrochemical cell consisting of a reference electrode, a working electrode (the BPP sample) and a counter electrode.

Open circuit potential measurements are performed to measure the potential between the working electrode and the reference electrode at zero current. The result of an OCP measurement is the open circuit potential, also called the corrosion potential, of the bipolar plate. This potential does not give much information about the bipolar plate's performance in an operating fuel cell. However, the OCP says something about the ability to oxidise or reduce the bipolar plate.

LSV or CV measurements are performed by sweeping the potential between two setpoints in one direction or for multiple cycles and recording the current at each potential. By performing LSV or CV with a low scanning rate, 1 mV s^{-1} or lower, at relevant fuel cell potentials, the measured current at a given potential can be interpreted as the corrosion current [24]. The measured currents give information about surface reactions on the bipolar plate and potential intervals where active corrosion and surface passivation occur.

CA experiments are used to study the current transient over a longer period of time. For fuel cell testing, this method involves "jumping" from a potential where no reactions are expected to occur to a typical operating fuel cell potential for a set amount of time and recording the current response. It is desirable to obtain a low current density even after several hours ($>$ 1000 h) of applied potential.

Ex-situ corrosion tests are usually performed in pH 3 electrolytes since this has been measured pH in run-off water from fuel cell stacks [67]. However, the actual pH is likely less acidic, as described in Subsection 2.4.1. Since the bipolar plate is immersed in the electrolyte during such ex-situ experiments, full contact between the plate and the electrolyte is obtained. In-situ, however, there are only droplets of liquid in the channels due to the carefully controlled humidity. Thus, the bipolar plate will only experience partial contact with acidic water droplets [24].

According to the guidelines outlined by the DOE, ex-situ tests should be performed at, or up to 0.6 $V_{Ag/AgCl}$ or 0.8 V_{SHE}. During ex-situ tests, the bipolar plates are therefore exposed to high voltages over time. Hinds and Brightman [67] measured the in-situ potential experienced by the cathode and anode BBPs. Their results showed that, regardless of the cell potential, the cathode BPP experienced voltages around 0.6 V. The anode BPP experienced relatively steady potentials equal to 0 V and was not influenced by the cell potential. During start-up and shut-down, potential spikes up to 0.8 V were observed on the cathode BPP, while potentials up to $\sim$0.6 V were measured on the anode BPP.

Thus, LSV/CV and CA are quick and easy methods to test bipolar plates and investigate possible failure mechanisms, although the bipolar plate is exposed to a very harsh environment, possibly harsher than in-situ conditions. Testing under such harsh conditions may be useful as an accelerated testing method and when comparing several bipolar plate candidates. However, the bipolar plate candidates should be tested inside an operating fuel cell to achieve more accurate performance details.

2.5.3 Surface Characterisation

Scanning Electron Microscopy, SEM, is a non-destructive surface characterisation method that can be used to study surfaces on micro scale. An electron beam irradiates a specific sample area and excites the atoms in the sample, giving rise to different signals such as backscattered electrons, secondary electrons, characteristic X-rays, Auger electrons and photons based on the electronic levels in each element [68]. Each signal can be detected by its respective detector as long as it is strong enough and has a certain speed, and an image of the surface is created. The most used signals are backscattered and secondary electrons as well as characteristic X-rays. The energy of the electron beam can vary between 0.1 - 40 kV, and the beam penetrates the sample to a certain depth based on this energy [69]. The higher the energy, the larger the penetration depth.

Information such as topography and morphology can be obtained by detecting secondary electrons, while backscattered electrons show composition contrast if the sample contains more than one phase. The characteristic X-rays are used when performing element analysis, Energy-dispersive X-ray spectroscopy (EDS).

Chapter 3

Experimental Procedure

3.1 Sample Preparation

3.1.1 Pre-Treatment Procedure

During this work, 0.4 mm thick, round AA1080 aluminium coupons, ⌀35 mm or ⌀38 mm, were used as substrates. The alloy composition of AA1080 is given in Table 3.1. An industrial alkaline cleaner with pH 12.8 was used to remove impurities and the oxide layer, Al_2O_3, on the aluminium surface before further treatment.

Table 3.1: Composition of aluminium coupons, AA1080 [70].

Al	**Fe**	**Si**	**V**	**Cu**	**Ga**	**Ti**	**Zn**	**Mg**	**Mn**	**Other**
$\geq$ 99.8%	$\leq$ 0.15%	$\leq$ 0.15%	$\leq$ 0.05%	$\leq$ 0.03%	$\leq$ 0.03%	$\leq$ 0.03%	$\leq$ 0.03%	$\leq$ 0.02%	$\leq$ 0.02%	$\leq$ 0.02%

The alkaline cleaning solution was prepared by adding 30 mL C-AK2011 and 3 mL C-AD1270 to 1 L deionised water (Milli-Q Integral pure water system, 18.2 MΩ cm at 25°C). The solution was mixed using a magnet stirrer. After mixing and before cleaning the samples in the alkaline cleaner, the solution was heated up to 55°C.

Four stainless steel substrates, SS316L, have been coated and tested for comparison. Three of them were cleaned for 10 minutes in 12.5% HCl, rinsed in DI water and dried using lint-free paper prior to coating deposition.

To study the effect of the pH of the alkaline cleaner, the pH was adjusted to 11, 11.5 and 12 by addition of phosphoric acid, H_3PO_4 (AnalaR NORMAPUR, 85%). Three samples were then immersed in each solution for 5 minutes, rinsed in deionised water, and dried using lint-free paper. Afterwards, the surface morphology was studied using scanning electron microscopy.

All samples used in further experiments were immersed in the alkaline cleaning solution (pH 12.8), rinsed in deionised water and dried using lint-free paper before further treatment.

Polishing

Some samples were polished using 1200 µm and 4000 µm paper before 3 µm diamonds were used. After polishing, the samples were rinsed in water to remove polishing particles. Finally, the samples were cleaned in the alkaline cleaner before further treatment.

Plasma Cleaning

A plasma cleaner (Diener Electronics, Femto) was used to plasma clean the samples using argon gas. The sample was placed in the plasma chamber, and the generator frequency and argon gas flow rate were set to 40 kHz and 200 sccm, respectively. The samples were plasma cleaned for 10 minutes.

3.1.2 Coating

After the pre-treatment procedure, different coatings were applied. Both thickness and coating techniques varied. The experimental procedure for each method is described in the subsequent subsections. Pre-treatment prior to deposition and coating thickness are specified in Section 3.3, "Sample Overview".

Zincating

A thin zinc layer was deposited by performing a dipping process. The zincating process consisted of a triple zincating step with an acidic stripping between each step. The composition of the zincate solution is given in Table 3.2 [42]. The zincating process was performed at room temperature and was as follows [42]:

Table 3.2: Zincate solution composition. The composition of the zincate solution was adopted from [42].

Compound	**Concentration [mol L^{-1}]**	**Manufacturer and Quality**
NaOH	0.25	Supelco EMSURE
ZnO	1.23	VWR TECHNICAL, 98%

- Dip sample in zincate solution for 20 seconds.
- Rinse in deionised water.
- Dip in 1 M sulphuric acid for 10 seconds.
- Rinse in DI water.
- Dip in zincate solution for 20 seconds.
- Rinse in DI water.

- Dip in 1 M sulphuric acid for 10 seconds.
- Rinse in deionised water.
- Dip in zincate solution for 20 seconds.
- Rinse in DI water.
- Dry sample.

Electron Beam Evaporation

An e-beam evaporator (Pfeiffer, Vacuum Classic 500) was used to deposit metallic titanium and gold. E-beam evaporation was performed under high vacuum (10^{-6} - 10^{-7} mbar). To avoid contamination of the vacuum chamber, the samples were rinsed in isopropanol and dried. The samples were then attached to the sample holder using double-sided tape. The sample holder was rotating during deposition. A deposition rate of 0.5 nm s^{-1} and an acceleration voltage of 8 keV were used for titanium deposition. For deposition of gold, the samples were argon plasma cleaned prior to deposition, the deposition rate was 0.1 nm s^{-1}, and an acceleration voltage of 8 kV was used.

Atomic Layer Deposition

Atomic layer deposition (Veeco, Savannah S200) was used to deposit aluminium oxide, Al_2O_3, titanium oxide, TiO_2 and hafnium oxide, HfO_2. Before deposition, the samples were rinsed in isopropanol and dried using nitrogen gas. Additionally, some of the samples were argon plasma cleaned prior to deposition. The samples were placed in the reactor and left there for some minutes to be heated up before deposition. A determined number of ALD cycles were performed depending on desired coating thickness and the oxide growth rate. The growth rate of the three oxides is given in Table 3.3.

Table 3.3: ALD growth rates for aluminium oxide, titanium oxide and hafnium oxide.

Oxide	**Growth rate [Å cycle^{-1}]**
Al_2O_3	1.2
TiO_2	0.5
HfO_2	1.07

3.2 Characterisation

Different characterisation methods have been used to test and investigate the different samples. The methods and experimental conditions are explained in the following subsections.

3.2.1 ICR-Measurements

The Interfacial Contact Resistance, ICR, between the sample (bipolar plate) and the gas diffusion layer was measured before and after corrosion measurements for all samples using the setup shown in Figure 3.1. The apparatus consisted of a stamp cylinder that pushed the lower gold-coated copper plate towards the upper plate with a variable pressure. A hole in the bottom plate allowed an electrically isolated gold pin to contact the lower surface of the sample.

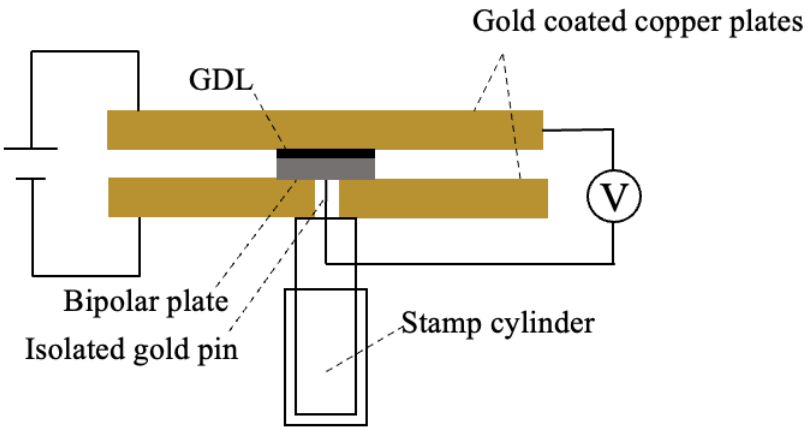

Figure 3.1: Simple sketch of the setup used to measure the interfacial contact resistance. Adapted from [71].

The sample, with a GDL on top, was placed between the gold plates. The lower plate was pushed towards the upper plate by applying a variable pressure, 33 - 250 N cm^{-2}. Meanwhile, a constant current of 1.5 A was applied between the gold plates through the sample. Using a multimeter, the resulting voltage between the upper gold plate and the gold pin was measured and plotted as a function of applied pressure. The standard in-situ compaction pressure of a fuel cell is 140 N cm^{-2} [66], and all ICR-measurements are therefore reported at this pressure.

When measuring the contact resistance after corrosion measurements, the sample surface pointing upwards was the same as the one exposed to the electrolyte. Again, a gas diffusion layer was placed on top of the sample.

The uncertainty in the ICR-measurements was estimated by performing the measurement three times on the same sample and calculating the standard deviation. All ICR-measurements were assumed to have the same uncertainty.

3.2.2 Electrochemical Measurements

Electrochemical experiments were performed using a three-electrode electrochemical cell, as shown in Figure 3.2. The cell consisted of a reference electrode, a platinum counter electrode and the sample as a working electrode. As a reference electrode, a reversible hydrogen electrode (RHE), a Gaskatel HydroFlex® Pt/Pd reference was used to avoid any chlorides in the system as this would lead to pitting corrosion of the aluminium coupon. The electrolyte, 0.1 M Na_2SO_4, was kept at 70°C and adjusted to pH 3 adding H_2SO_4 (Supleco EMSURE, 98%). All reported potentials are given vs RHE (pH 3). Electrolyte calculations are shown in Appendix A. The solution was purged with nitrogen gas to de-aerate the electrolyte prior to experiments. All electrochemical measurements were performed using a GAMRY Reference 600 Potentiostat. To study the effect of the electrolyte pH, the electrolyte was adjusted to pH 5, adding H_2SO_4. The potential was recalculated and expressed versus RHE (pH 3).

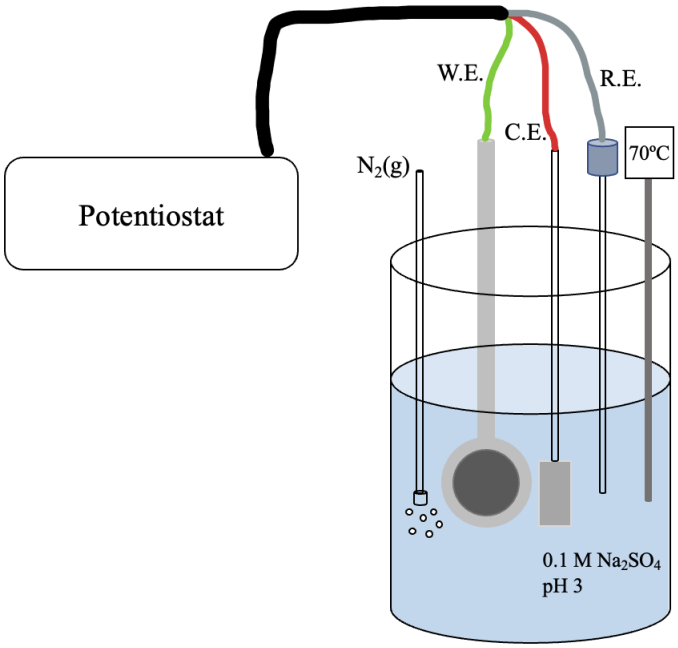

Figure 3.2: Simple sketch of the three-electrode electrochemical cell used to perform electrochemical measurements.

All potentiodynamic measurements were performed with a sweep rate of 1 mV s^{-1} starting at -0.8 V up to 1 V, and only one cycle was performed. This was performed to study the current density over a wider potential range. Potentiodynamic measurements were performed for 1 or 24 hours at a potential of 1 V.

3.2.3 Scanning Electron Microscopy

A "Hitachi S-3400N" SEM was used to study the surface morphology of the samples. The samples were studied after pre-treatment, after applying the coating layers, and after corrosion measurements were performed. To capture pictures of the sample surface, an acceleration voltage of 20 kV was used, and each sample was pictured using secondary electrons with 5000, 1200 and 400 magnification. The working distance varied between 6-10 mm. In addition, energy Dispersive Spectroscopy, EDS, was performed to study the elemental composition of some of the samples. Depending on the coating material, variable acceleration voltages, 10 - 20 kV, were used.

One sample was studied using a Field Emission SEM (FEI Apreo). Compared to "Hitachi S-3400N" SEM it is possible to achieve higher resolution using this Field Emission SEM. An acceleration voltage of 5 kV and a working distance of 8 mm was used to capture pictures with 5000, 1200 and 400 magnification.

3.3 Sample Overview

48 samples with different pre-treatment and coating layers have been tested and investigated. The tables below summarise treatment, coating thickness and characterisation methods applied to the different samples. If else not stated, the samples were cleaned for 2 minutes in the alkaline cleaner with pH 12.8. LSV was performed with a sweep rate of 1 mV s^{-1} between -0.8 - 1 V and CA at a potential of 1 V for 1 hour or 24 hours. Both LSV and CA have been carried out in electrolytes adjusted to pH 3. Only a few samples were tested in pH 5 electrolytes, and for those samples, this is explicitly given in the tables. Treatment and/or coating application were done in the order given in the tables unless otherwise stated. The characterisation was also done in the order given in the tables after treatment/coating unless otherwise stated.

3.3.1 Uncoated Aluminium

For the uncoated aluminium samples, the interfacial contact resistances were measured straight after the alkaline cleaning procedure and compared. Electrochemical measurements, as outlined in Table 3.4, were performed on the samples. Additionally, one sample was polished before studying the surface characteristics using SEM.

Table 3.4: Sample preparation and characterisation of uncoated aluminium.

Sample no.	Treatment/Coating	Characterisation
1	Alkaline cleaning (5 min)	ICR
2	Alkaline cleaning	ICR ICR (after 11 days) LSV CA, 1 h
3	Alkaline cleaning	LSV (pH 5) CA (pH 5), 1 h
4	Polishing	SEM

Variable pH of Alkaline Cleaner

The pH of the alkaline cleaner was adjusted to three different pH values. One sample was cleaned in each solution, and surface characteristics were compared by studying the sample surfaces using SEM, as summarised in Table 3.5.

Table 3.5: Sample preparation and characterisation of samples cleaned in alkaline cleaning solutions with variable pH.

Sample no.	Treatment	Characterisation
5	Alkaline cleaning (5 min), pH 11	SEM
6	Alkaline cleaning (5 min), pH 11.5	SEM
7	Alkaline cleaning (5 min), pH 12	SEM

3.3.2 Titanium Coatings

Cleaning Procedure and Zincating

Four samples were cleaned and zincated. These were the only zincated samples in this study due to the performance of the zincated samples tested during the project work [9]. These samples were cleaned in the alkaline cleaning solution. Immersion time varied and is given together with coating thickness and characterisation methods in Table 3.6. Additionally, ICR-measurements and SEM were performed when the pre-treatment and the zincating process were complete.

Table 3.6: Sample preparation and characterisation of zincated aluminium coated with titanium using electron beam evaporation. Variable cleaning intervals prior to zincating.

Sample no.	Treatment/Coating	Characterisation
8	Alkaline cleaning (5 min)	ICR
	Zincating	SEM
	200 nm Titanium	CA, 1 h
		ICR
9	Alkaline cleaning (4 min)	ICR
	Zincating	SEM
	200 nm Titanium	CA, 1 h
		ICR
10	Alkaline cleaning (3 min)	ICR
	Zincating	SEM
	200 nm Titanium	CA, 1 h
		ICR
11	Alkaline cleaning	ICR
	Zincating	SEM
	200 nm Titanium	CA, 1 h
		ICR

Variable Titanium Thickness

Titanium coatings with variable thickness were applied on aluminium and stainless steel substrates performing electron beam evaporation and magnetron sputtering. Three aluminium and three stainless steel samples were coated using e-beam, tested and compared according to Table 3.7 and 3.8 respectively.

Table 3.7: Sample preparation and characterisation of aluminium samples coated with different titanium thickness performing e-beam evaporation.

Sample no.	Treatment/Coating	Characterisation
12	Alkaline cleaning	ICR
	900 nm Titanium	CA, 1 h
		ICR
13	Alkaline cleaning	ICR
	300 nm Titanium	CA, 1 h
		ICR
14	Alkaline cleaning	ICR
	150 nm Titanium	CA, 1 h
		ICR

Table 3.8: Sample preparation and characterisation of stainless steel samples coated with different titanium thickness performing e-beam evaporation.

Sample no.	Treatment/Coating	Characterisation
15	Acidic cleaning (10 min), 12.5% HCl 900 nm Titanium	ICR CA, 1 h ICR
16	Acidic cleaning (10 min), 12.5% HCl 300 nm Titanium	ICR CA, 1 h ICR
17	Acidic cleaning (10 min), 12.5% HCl 150 nm Titanium	ICR CA, 1 h ICR

Two samples, one aluminium and one stainless steel were coated with 1.5 µm titanium using magnetron sputtering. The samples were characterised and tested as stated in Table 3.9.

Table 3.9: Sample preparation and characterisation of one aluminium sample and one stainless steel sample coated with titanium applying magnetron sputtering.

Sample no.	Substrate	Treatment/Coating	Characterisation
18*	Aluminium	1.5 µm Titanium	ICR SEM LSV CA, 1 h ICR
19*	Stainless Steel	1.5 µm Titanium	ICR SEM LSV CA, 1 h ICR

* Marit Stange prepared this sample.

3.3.3 Oxides as Adhesion Layer

Aluminium oxide and titanium oxide were applied with ALD and tested as adhesion layers under metallic titanium deposited using an e-beam evaporator. Thickness and characterisation methods are specified in Table 3.10.

Table 3.10: Sample preparation and characterisation of aluminium samples coated with aluminium- or titanium oxide performing ALD and titanium using an e-beam evaporator.

Substrate	Treatment/Coating	Characterisation
20	Alkaline cleaning	ICR
	5 nm Al_2O_3	SEM
	200 nm Titanium	LSV
		CA, 1 h
		ICR
21	Alkaline cleaning	ICR
	5 nm TiO_2	SEM
	200 nm Titanium	LSV
		CA, 1 h
		ICR

To study the effect of oxide thickness on electrical conductivity and compare the resistivity of titanium oxide and aluminium oxide, different Al_2O_3 thickness were deposited on three samples. The same thickness of TiO_2 were deposited on three other samples applying ALD. The contact resistances were measured and compared. Aluminium- and titanium oxide thickness are given in Table 3.11.

Table 3.11: Sample preparation and characterisation of aluminium samples coated with different aluminium oxide and titanium oxide thickness performing atomic layer deposition.

Sample no.	Treatment/Coating	Characterisation
22	Alkaline cleaning	ICR
	5 nm Al_2O_3	
23	Alkaline cleaning	ICR
	2 nm Al_2O_3	
24	Alkaline cleaning	ICR
	1 nm Al_2O_3	
25	Alkaline cleaning	ICR
	5 nm TiO_2	
26	Alkaline cleaning	ICR
	2 nm TiO_2	
27	Alkaline cleaning	ICR
	1 nm TiO_2	

3.3.4 Oxides as Main Coating Layer

Titanium Oxide

Three samples were coated with 5 nm aluminium oxide and variable titanium oxide thickness applying ALD, as given in Table 3.12. The samples were characterised according to

the table.

Table 3.12: Sample preparation and characterisation of aluminium samples coated with aluminium- and titanium oxide performing atomic layer deposition.

Sample no.	Treatment/Coating	Characterisation
28	Alkaline cleaning	ICR
	Ar plasma cleaning	LSV
	5 nm Al_2O_3	CA, 1 h
	20 nm TiO_2	ICR
		SEM & EDS
29	Alkaline cleaning	ICR
	Ar plasma cleaning	LSV
	5 nm Al_2O_3	CA, 1 h
	10 nm TiO_2	ICR
		SEM & EDS
30	Alkaline cleaning	ICR
	Ar plasma cleaning	LSV
	5 nm Al_2O_3	CA, 1 h
	5 nm TiO_2	ICR
		SEM & EDS

Aluminium Oxide

Aluminium oxide, deposited performing ALD, was tested as outer coating layer. Coating thickness as well as characterisation methods are given in Table 3.13.

Table 3.13: Sample preparation and characterisation of aluminium samples coated with aluminium oxide performing ALD. One sample was coated with TiO_2 prior to aluminium oxide deposition.

Sample no.	Treatment/Coating	Characterisation
31	Alkaline cleaning	ICR
	5 nm Al_2O_3	LSV
		CA, 1 h
		ICR
32	Alkaline cleaning	ICR
	Ar plasma cleaning	LSV
	5 nm Al_2O_3	CA, 1 h
		ICR
33	Alkaline cleaning	ICR
	5 nm TiO_2	LSV
	5 nm Al_2O_3	CA, 1 h
		ICR

3.3.5 Titanium Nitride as Main Coating Layer

Titanium nitride has been tested as main coating layer, applied directly on three aluminium samples after pre-treatment, performing magnetron sputtering. An additional top layer of gold was applied to two of the samples using an e-beam evaporator. Coating thickness and characterisation methods are specified in Table 3.14. SEM was performed on sample no. 35 and 36, both prior and post gold deposition.

Table 3.14: Sample preparation and characterisation of aluminium samples coated with titanium nitride. A gold top layer was applied on two of the samples.

Sample no.	**Treatment/Coating**	**Characterisation**
34*	Alkaline cleaning	ICR
	20 nm TiN	LSV
		CA, 24 h
		ICR
		SEM & EDS
35*	Alkaline cleaning	ICR
	20 nm TiN	SEM & EDS
	Ar plasma cleaning	LSV
	10 nm Gold	CA, 24 h
		ICR
36*	Polishing	ICR
	Alkaline cleaning	SEM & EDS
	20 nm TiN	LSV
	Ar plasma cleaning	CA, 24 h
	10 nm Gold	ICR

* Abdulla Bin Afif performed TiN deposition on this sample.

3.3.6 Combining E-beam and Sputtering/ALD

Six aluminium samples were coated with titanium using e-beam evaporation. Titanium nitride was deposited on top of one sample performing magnetron sputtering, while the rest of the samples were coated with different TiO_2 thickness performing ALD. Coating thickness and characterisation methods performed are given in Table 3.15.

Table 3.15: Sample preparation and characterisation of aluminium samples coated with titanium and titanium nitride or variable titanium oxide thickness.

Sample no.	Treatment/Coating	Characterisation
37	Alkaline cleaning	ICR
	200 nm Titanium	SEM
	20 nm TiN	LSV
		CA, 24 h
		ICR
		SEM
38	Alkaline cleaning	ICR
	200 nm Titanium	SEM
	5 nm TiO_2	LSV
		CA, 1 h
		ICR
		SEM
39	Alkaline cleaning	ICR
	200 nm Titanium	LSV
	4 nm TiO_2	CA, 24 h
		ICR
40	Alkaline cleaning	ICR
	200 nm Titanium	LSV
	3 nm TiO_2	CA, 24 h
		ICR
41	Alkaline cleaning	ICR
	200 nm Titanium	LSV
	2 nm TiO_2	CA, 24 h
		ICR
42	Alkaline cleaning	ICR
	200 nm Titanium	LSV
	1 nm TiO_2	CA, 24 h
		ICR

Gold Top Layer

Six aluminium samples were cleaned and coated with titanium performing electron beam evaporation. Thereafter, one sample was coated with titanium nitride performing magnetron sputtering, another was coated with hafnium oxide, and the rest were coated with titanium oxide. Both hafnium oxide and titanium oxide were applied with ALD. Finally, all samples were coated with gold, performing e-beam evaporation. Coating thickness and characterisation methods are specified in Table 3.16. Sample no. 48 was not pictured using SEM as it was assumed to be similar to the one with 5 nm TiO_2. EDS was not performed on sample no. 47 before corrosion measurements, as it was assumed to give the same results as the unpolished one.

Table 3.16: Sample preparation and characterisation of aluminium samples coated with titanium, TiN or HfO_2 or TiO_2 and gold.

Sample no.	**Treatment/Coating**	**Characterisation**
43	Alkaline cleaning	ICR
	200 nm Titanium	SEM & EDS
	20 nm TiN	LSV
	Ar plasma cleaning	CA, 24 h
	10 nm Gold	ICR
		SEM & EDS
44	Alkaline cleaning	ICR
	200 nm Titanium	SEM & EDS
	20 nm HfO_2	LSV
	Ar plasma cleaning	CA, 24 h
	10 nm Gold	ICR
		SEM & EDS
45	Alkaline cleaning	ICR
	200 nm Titanium	SEM & EDS
	5 nm TiO_2	LSV
	Ar plasma cleaning	CA, 24 h
	10 nm Gold	ICR
		SEM & EDS
46	Alkaline cleaning	ICR
	200 nm Titanium	LSV (pH 5)
	5 nm TiO_2	CA, (pH 5), 24 h
	Ar plasma cleaning	ICR
	10 nm Gold	
47	Polishing	ICR
	Alkaline cleaning	SEM
	200 nm Titanium	LSV
	5 nm TiO_2	CA, 24 h
	Ar plasma cleaning	ICR
	10 nm Gold	SEM & EDS
48	Alkaline cleaning	ICR
	200 nm Titanium	LSV
	4 nm TiO_2	CA, 24 h
	Ar plasma cleaning	ICR
	10 nm Gold	

Chapter 4

Results

4.1 Uncoated Aluminium

The results obtained from the uncoated aluminium samples (#1 - #7) are presented in this section.

Interfacial Contact Resistance

Before cleaning the aluminium sample, it had an interfacial contact resistance of 38.8±7.7 mΩ cm^2. Straight after cleaning it for 2 minutes in the alkaline cleaner, it obtained an interfacial contact resistance of 10.8±2.1 mΩ cm^2. The ICR of this sample increased to 16.3±3.2 mΩ cm^2 after 11 days in a plastic bag. Another aluminium sample, cleaned for 5 minutes, obtained an ICR of 12.5±2.5 mΩ cm^2 directly after cleaning. These results showed that an immersion time of 2 minutes resulted in the same degree of oxide dissolution as 5 minutes immersion time. Additionally, shorter immersion time led to less pits on the sample surface (Figure 4.5 and 4.8).

Surface Polishing

Figure 4.1 shows SEM images of an aluminium sample as-received (a - c), obtained during the project work [9], and a polished aluminium sample, #4, (d - f). The images show that the scratches and small holes on the surface of the as-received sample were removed by polishing the sample. After polishing, the surface was smoother but had a certain surface texture.

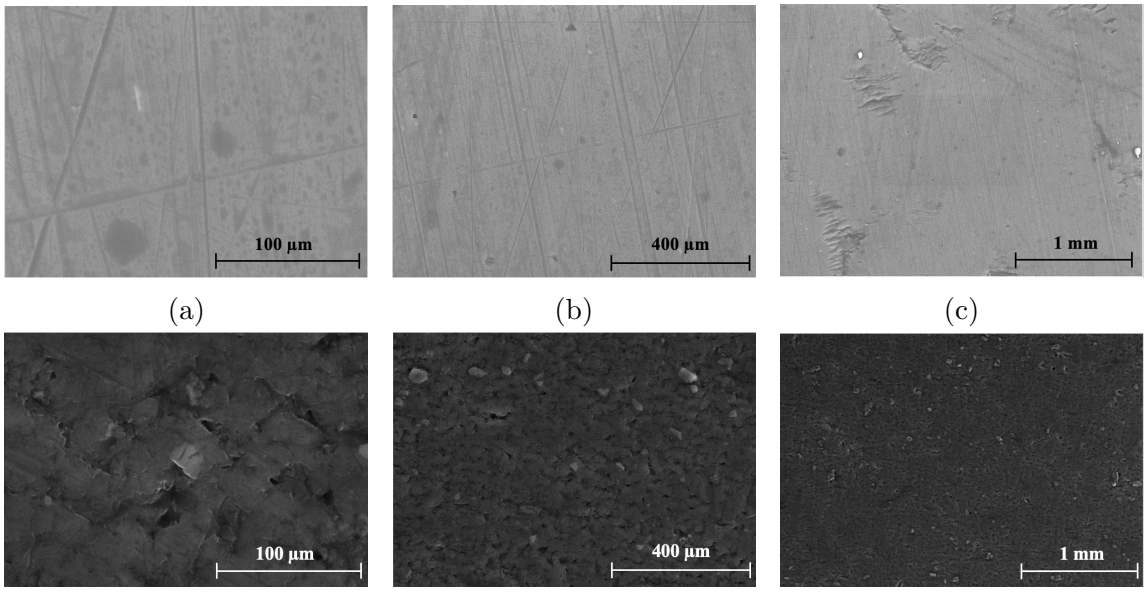

Figure 4.1: SEM images of an aluminium sample before any treatment (a - c) [9] and a polished sample, #4, (d - f). Notice the scale difference.

Corrosion Measurements

The results of linear sweep voltammetry performed on uncoated aluminium, #2 and #3, in electrolytes adjusted to pH 3 and pH 5, respectively, are shown in Figure 4.2.

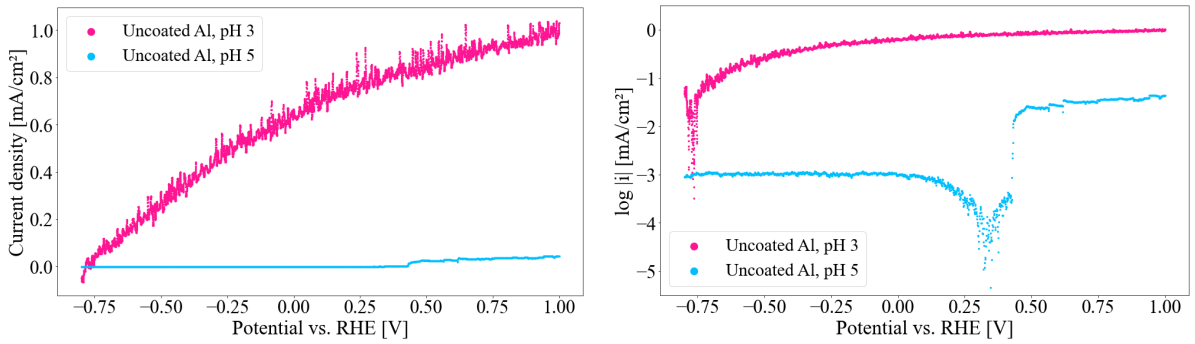

Figure 4.2: Polarisation curves of uncoated aluminium samples (#2 (pink) and #3 (blue)) in 0.1 M Na_2SO_4 electrolyte, pH 3 or pH 5 at 70°C. Sweep rate: 1 mV s^{-1}, sweeping from -0.8 - 1 V. Current density plotted against potential (a) and log $|i|$ against potential (b).

As seen from Figure 4.2b, the corrosion potential measured on uncoated aluminium in pH 5 was much higher than that measured on uncoated aluminium in pH 3. Furthermore, the corrosion current density increased linearly with applied potential on aluminium when polarising in electrolyte adjusted to pH 3 compared to a more stable current density obtained in the pH 5 electrolyte.

The results of potentiostatic measurements on uncoated aluminium performed in pH 3 and pH 5 electrolytes are shown in Figure 4.3. Increasing the electrolyte pH resulted in a lower current response of uncoated aluminium. In a pH 5 environment, aluminium oxide is, according to the Pourbaix diagram (Fig. 2.7), stable and protects aluminium from corrosion, while pH 3 is in the active area where aluminium is prone to corrosion. The current density was around one order of magnitude lower in pH 5 electrolyte compared to pH 3 electrolyte.

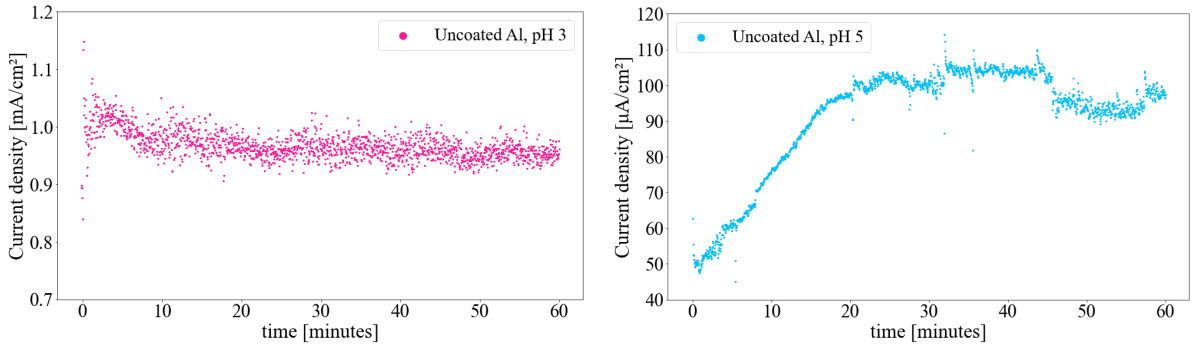

(a) (b)

Figure 4.3: Chronoamperometric scans on uncoated aluminium samples in 0.1 M Na_2SO_4 electrolyte, pH 3 (a) or pH 5 (b) at 70°C. The potential was kept at 1 V for 1 hour. Notice the unit difference.

4.1.1 Variable pH of Alkaline Cleaner

SEM pictures of the sample surfaces after cleaning three aluminium samples for 5 minutes in alkaline cleaning solutions with pH 11 (#5), 11.5 (#6), and 12 (#7), respectively, are shown in Figure 4.4. As can be seen from the pictures, pits were present on all surfaces. Pits were observed independently of the pH of the cleaning solution.

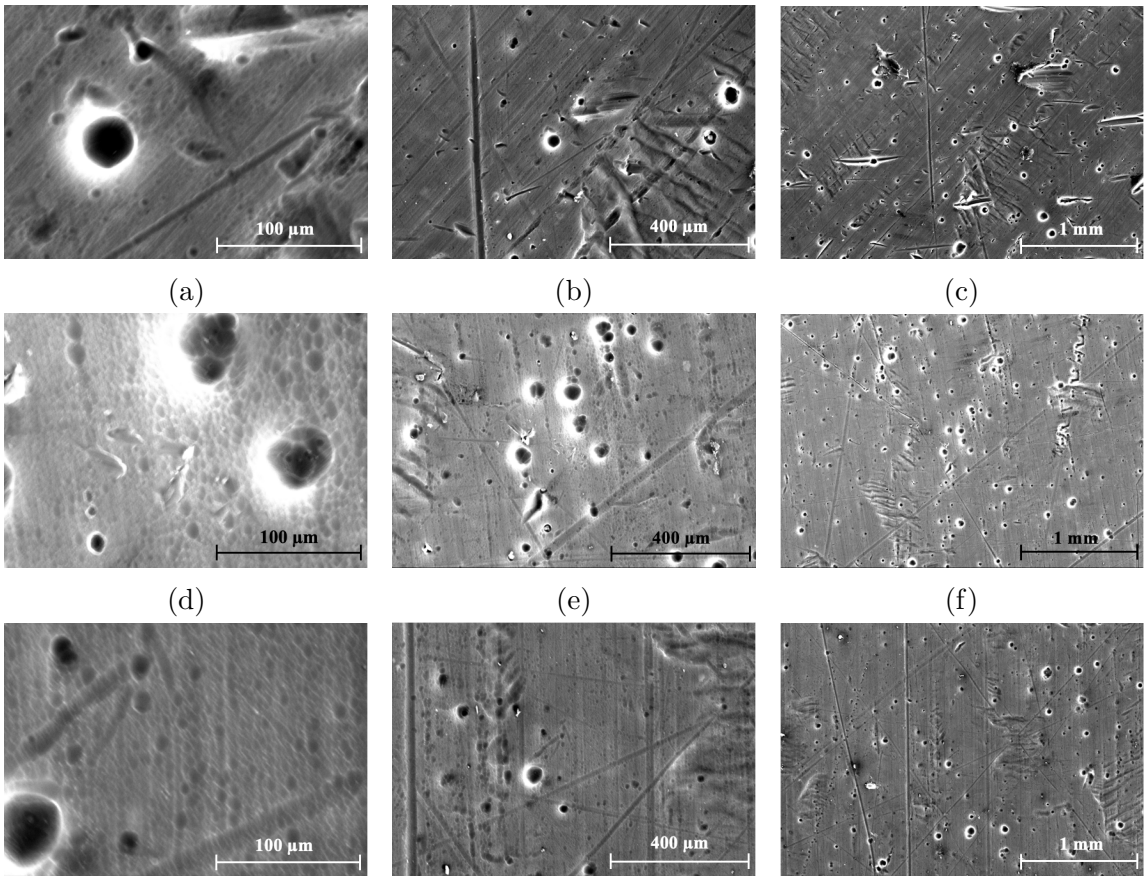

Figure 4.4: SEM images of three different aluminium samples after alkaline cleaning for 5 minutes in pH 11 (a - c), 11.5 (d - f), and 12 (g - i). Notice the scale difference.

4.2 Metallic Titanium Coatings

The results obtained from the zincated aluminium samples coated with 200 nm titanium (#8 - #11) and the aluminium and stainless steel samples coated with variable titanium thickness (#12 - #19) are presented in this section.

4.2.1 Cleaning Procedure and Zincating

The results of cleaning aluminium samples for 5 min, 4 min, 3 min, and 2 min prior to the zincate process are shown below. SEM pictures show that a shorter immersion time led to fewer pits on the surface. The smoothest surface was obtained by cleaning the sample for 2 minutes, as can be seen in Figure 4.8. The sample surfaces were also pictured after applying 200 nm titanium.

Surface Characterisation before Corrosion Measurements

Figure 4.5 shows SEM images of the zincated sample surface after cleaning the sample for 5 minutes prior to the zincating process before (a - c) and after (d - f) 200 nm Ti was applied performing e-beam evaporation. As can be seen from the pictures, the pits, probably formed during the alkaline treatment, were present after zincating and also after the application of titanium.

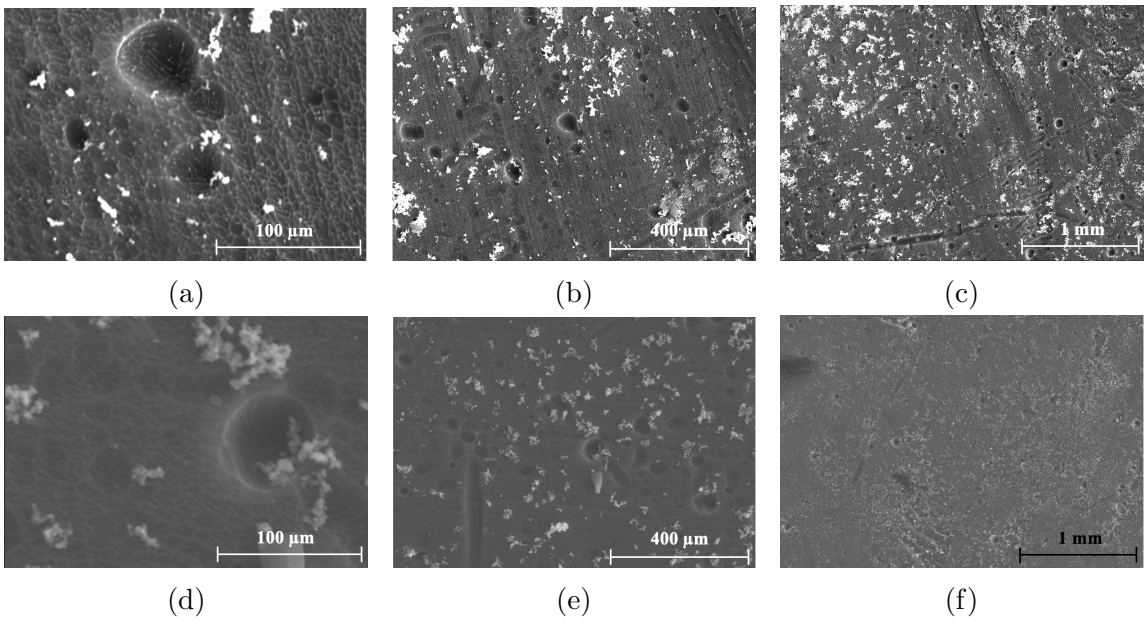

Figure 4.5: SEM images of zincated aluminium before (a - c) and after (d - f) 200 nm titanium was applied. Alkaline cleaning for 5 minutes was performed prior to zincating. Notice the scale difference.

Figure 4.6 shows SEM images of the sample surface after cleaning the sample for 4 minutes prior to zincating both before (a - c) and after (d - f) a 200 nm thick titanium layer was applied, performing e-beam evaporation. This sample surface appeared similar to the one cleaned for 5 minutes prior to zincating and titanium deposition.

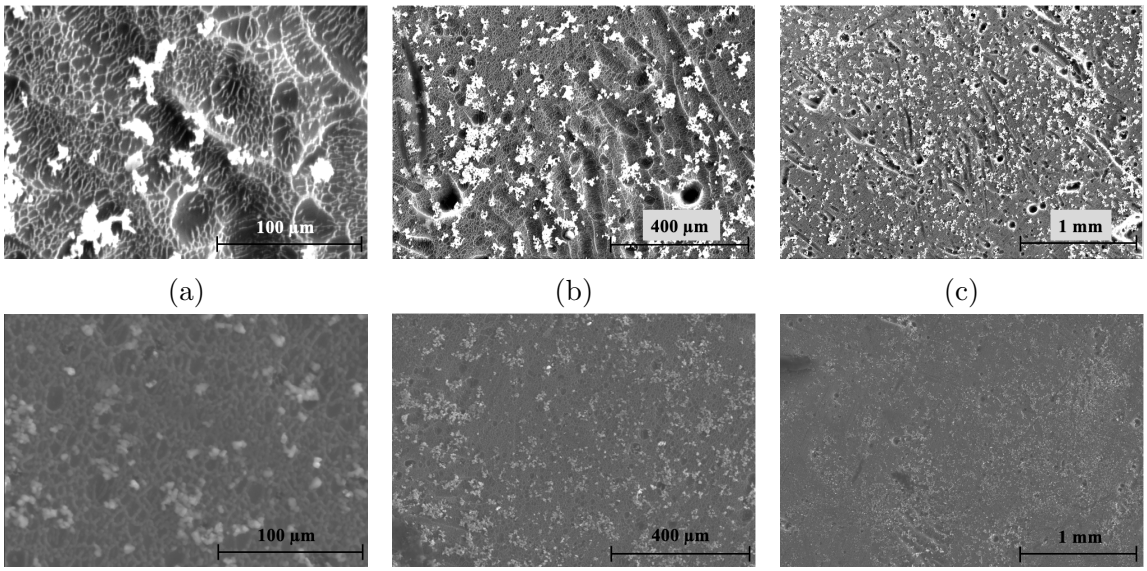

Figure 4.6: SEM images of zincated aluminium before (a - c) and after (d - f) 200 nm titanium was applied. Alkaline cleaning for 4 minutes was performed prior to zincating. Notice the scale difference.

SEM images of the zincated sample surface after cleaning the sample for 3 minutes prior to zincating, before (a - c) and after (d - f) 200 nm titanium was applied performing e-beam evaporation are shown in Figure 4.7. Pits were visible on this sample as well, although there were fewer compared to the samples cleaned for 5 or 4 minutes.

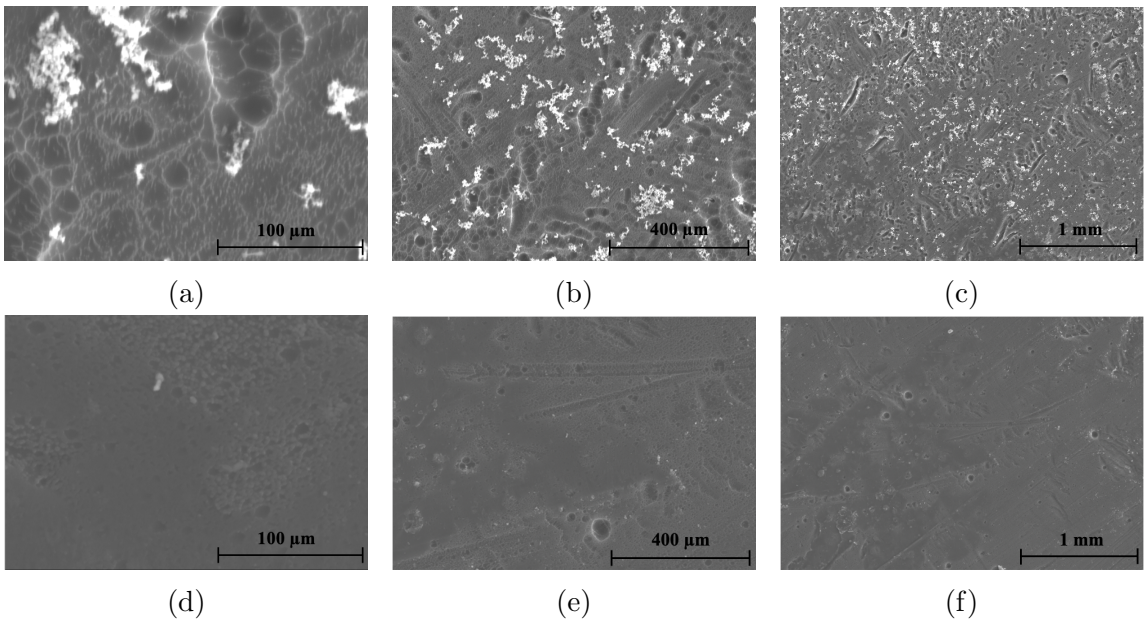

Figure 4.7: SEM images of zincated aluminium before (a - c) and after (d - f) applying 200 nm titanium. Alkaline cleaning Notice the difference in scale.

SEM images of sample no. 11 are shown in Figure 4.8. The surface was pictured when alkaline cleaning for 2 minutes and zincating were performed (a - c) and after applying 200 nm titanium by e-beam evaporation (d - f). Only a few pits were present on the surface, and the amount was smaller compared to the samples shown in Figures 4.5, 4.6, and 4.7.

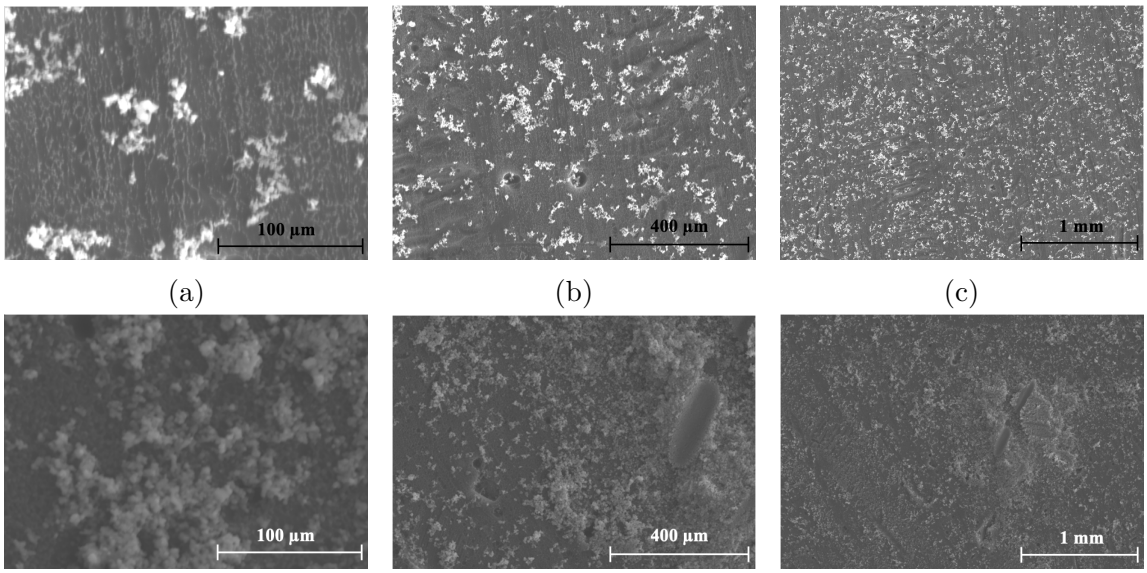

Figure 4.8: SEM images of zincated aluminium before (a - c) and after (d - f) 200 nm titanium was applied. Alkaline cleaning for 2 minutes prior to zincating. Notice the different scale bars.

Corrosion Measurements

The results of potentiostatic measurements performed on all the above samples are shown in Figure 4.9. The lowest current densities were obtained on samples no. 8 (5 min) and 11 (2 min), while the highest current response was obtained on sample no. 10 (3 min). The difference in current density is not significant and may be due to coincidences and uncertainties in the measurements. The titanium layers were worn off under the O-ring, and the electrolyte had reached the back of the samples. Partial coating failure was observed on all samples. The current responses were low during the first minutes of the scan. If the electrolyte had not reached the back of the samples and the coatings were still intact, the current responses could have been similar to those obtained at the beginning of the scans.

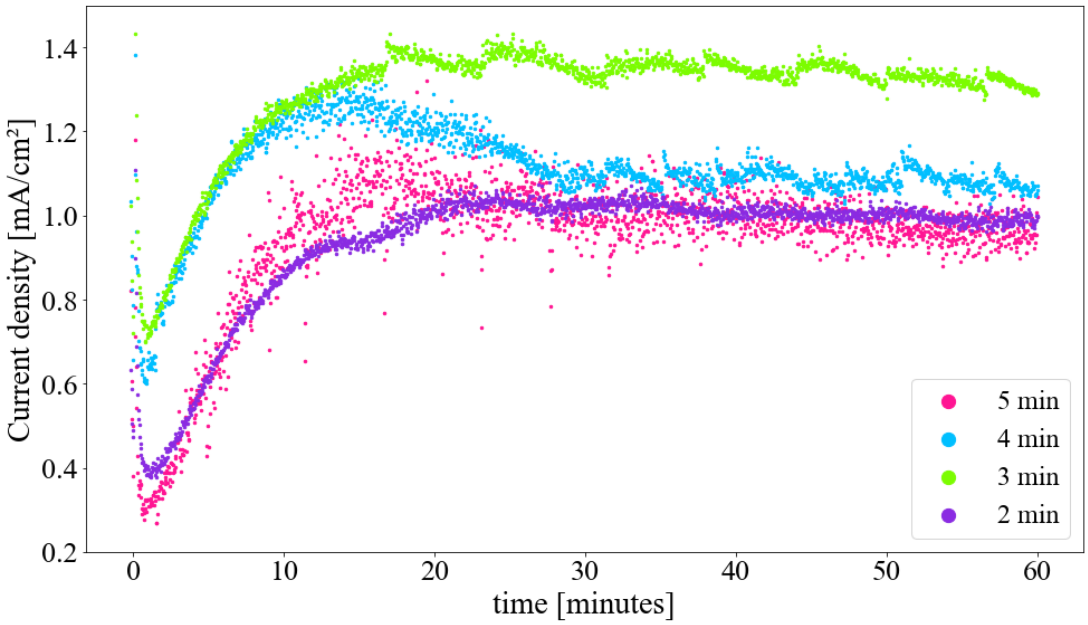

Figure 4.9: Chronoamperometric scans on zincated aluminium samples coated with 200 nm titanium. The samples were cleaned for 5 min (#8), 4 min (#9), 3 min (#10), and 2 min (#11), respectively, prior to zincating. All samples were tested in 0.1 M Na_2SO_4, pH 3 at 70°C. The potential was kept at 1 V for 1 hour.

Interfacial Contact Resistance

The measured contact resistances after zincating, after applying titanium coatings and post corrosion tests are given in Table 4.1. The sample cleaned for 2 minutes obtained the lowest ICR after zincating.

Table 4.1: Interfacial contact resistances at a compaction pressure of 140 N cm^{-2} of aluminium samples after zincating, after applying titanium, and post chronoamperometry for 1 h at 1 V.

Sample no.	**Treatment/coating**	**ICR at 140 N cm^{-2} [mΩ cm^2]**
8	5 min cleaning & zincating	11.0±2.2
	200 nm Ti	10.5±2.1
	After CA, 1 h	36.9±7.3
9	4 min cleaning & zincating	13.0±2.6
	200 nm Ti	7.4±1.5
	After CA, 1 h	53.9±10.7
10	3 min cleaning & zincating	13.6±2.7
	200 nm Ti	8.7±1.7
	After CA, 1 h	49.8±9.9
11	2 min cleaning & zincating	6.7±1.3
	200 nm Ti	8.1±1.6
	After CA, 1 h	72.4±14.4

4.2.2 Variable Titanium Thickness

The 900 nm thick titanium coatings deposited performing e-beam evaporation on aluminium and stainless steel did not cover the sample surfaces completely and contained irregularities, as shown in Figure 4.10. The 300 nm and 150 nm thick coatings were more uniform and smooth, and appeared visually defect-free. However, these were not pictured.

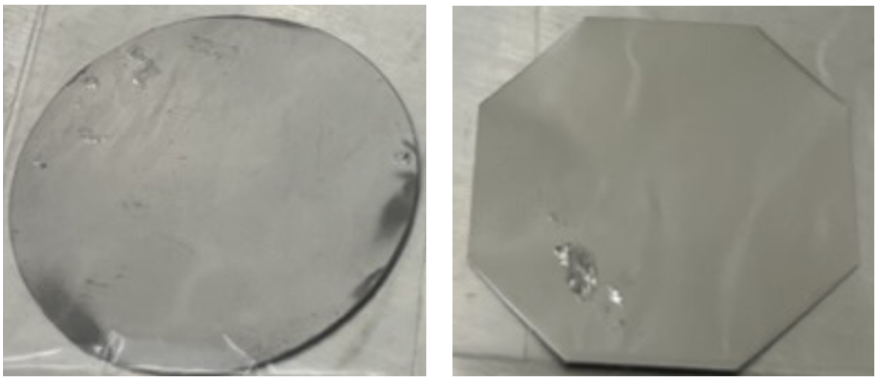

(a) (b)

Figure 4.10: Pictures of aluminium (a) and stainless steel (b) coated with 900 nm titanium performing e-beam evaporation. Coating-defects were visible on both samples.

Corrosion Measurements

When samples no. 12 and 15 were immersed in the electrolyte, the electrolyte penetrated the coating layers immediately before a potential was applied, resulting in coating delamination, as shown in Figure 4.11. The same behaviour was observed for sample no. 13, but it occurred 2 minutes after the potential was applied. The 900 nm and 300 nm thick coatings on aluminium failed during testing. However, the 150 nm thick titanium layer adhered to the aluminium surface during the experiment. The coating was only worn off in the area where the O-ring had been placed. The 300 nm and 150 nm thick coatings on stainless steel adhered to the surfaces during the electrochemical experiments. The 300 nm thick coating was worn off in the O-ring area.

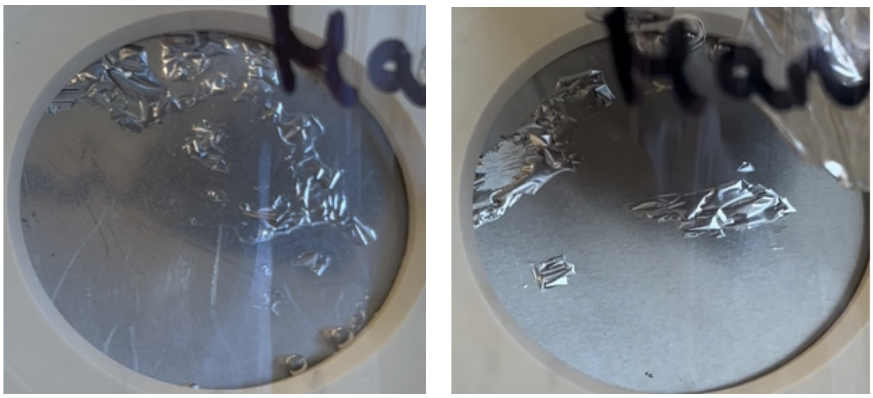

(a) (b)

Figure 4.11: Aluminium, #12, (a) and stainless steel, #15, (b) samples coated with 900 nm titanium after immersing them in the electrolyte. Bubbles under the coating layers were visible.

The results of potentiostatic measurements on aluminium coated with different titanium thickness are shown in Figure 4.12. For the sample coated with 300 nm Ti (#13), it seems like the connection was lost between 6 - 22 minutes. The current transients for all three samples were similar to the one obtained on uncoated aluminium in pH 3 electrolyte (Fig. 4.3a), indicating little or no protection by the titanium coating.

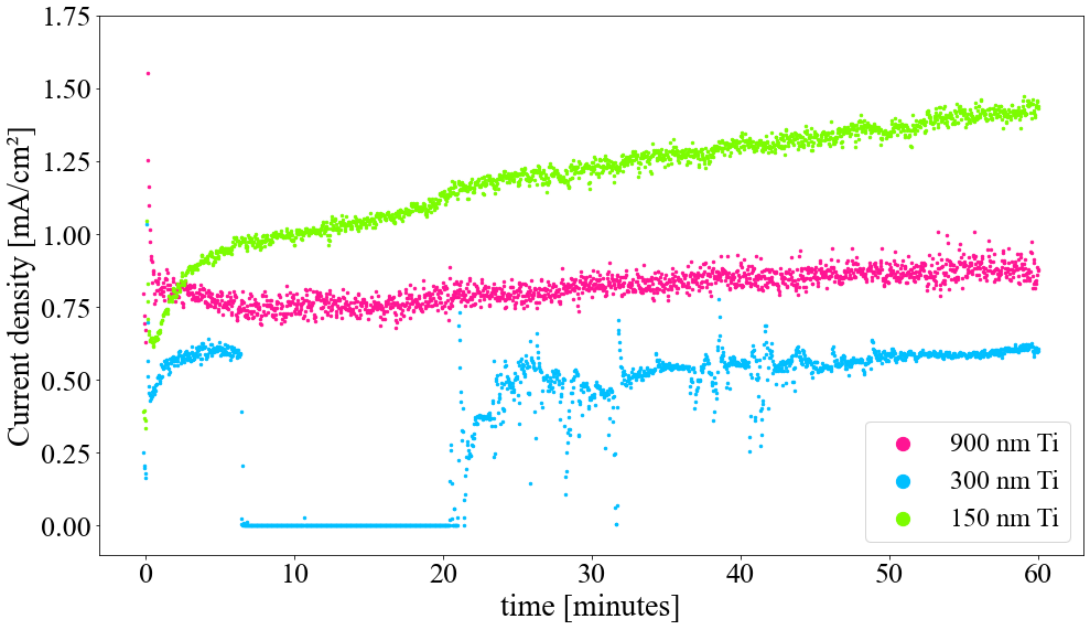

Figure 4.12: Chronoamperometric scans on coated aluminium samples, #12 (pink), #13 (blue), and #14 (green) in 0.1 M Na_2SO_4 electrolyte, pH 3 at 70°C. The potential was kept at 1 V for 1 hour.

The results of potentiostatic measurements on stainless steel coated with different titanium thickness are shown in Figure 4.13.

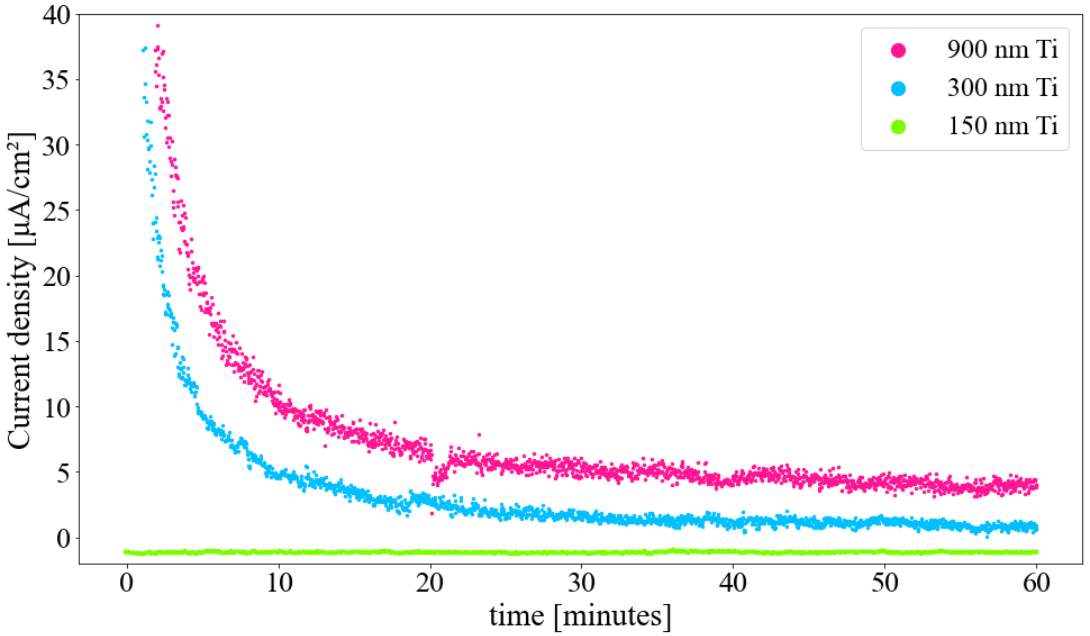

Figure 4.13: Chronoamperometric scans on coated stainless steel samples, #15 (pink), #15 (blue), and #16 (green) in 0.1 M Na_2SO_4 electrolyte, pH 3 at 70°C. The potential was kept at 1 V for 1 hour.

As can be seen from the figure, the measured currents on stainless steel are much lower than the ones obtained on aluminium (Figure 4.12). This is probably due to the stability of stainless steel in the simulated PEMFC environment compared to aluminium's stability. Since the 900 nm thick coatings were poor and failed, the underlying substrates were exposed to the electrolyte, and the current responses can probably be interpreted as from uncoated aluminium and uncoated stainless steel. Further, the thinner the coating layer on stainless steel, the lower the current response. This trend may have been due to the improved coating quality as the coating thickness decreased.

Interfacial Contact Resistance

Measured interfacial contact resistances are given in Table 4.2, showing lower values for the coated stainless steel samples compared to aluminium. Before corrosion measurements, there was a decreasing trend in interfacial contact resistance for the stainless steel samples as the titanium thickness increased. After performing corrosion measurements, the ICR-measurements showed an increase in contact resistance for all samples. The increase was most significant for the aluminium samples. Aluminium coated with 150 nm titanium obtained the highest ICR after corrosion measurements. As this was the only aluminium sample where the coating did not fail, an oxide may have formed on the titanium surface and thus resulted in increased contact resistance.

Table 4.2: Interfacial contact resistances at a compaction pressure of 140 N cm^{-2} of aluminium and stainless steel samples coated with different titanium thickness, before and after performing chronoamperometry for 1 h at 1 V.

Sample no.	**Substrate**	**Coating/characterisation**	**ICR at 140 N cm^{-2} [mΩ cm^2]**
12	Al	900 nm Ti	13.2±2.6
		After CA, 1 h	31.4±6.2
13	Al	300 nm Ti	10.3±2.0
		After CA, 1 h	33.0±6.6
14	Al	150 nm Ti	13.5±2.7
		After CA, 1 h	91.0±18.1
15	SS	900 nm Ti	6.4±1.3
		After CA, 1 h	15.2±3.0
16	SS	300 nm Ti	7.4±1.5
		After CA, 1 h	24.2±4.8
17	SS	150 nm Ti	10.4±2.1
		After CA, 1 h	20.0±4.0

The 1.5 µm thick Ti coatings on aluminium, #18, and stainless steel, #19, applied by magnetron sputtering covered the sample surfaces uniformly and did not contain any visible irregularities, as can be seen on the aluminium sample pictured in Figure 4.15a.

Surface Characterisation before Corrosion Measurements

SEM pictures of samples no. 18 and 19 are shown in Figure 4.14. The aluminium sample (a - c) was not completely even, and some holes and irregularities were visible. Pictures of the stainless steel sample (d - f) showed a smoother surface with fewer pits.

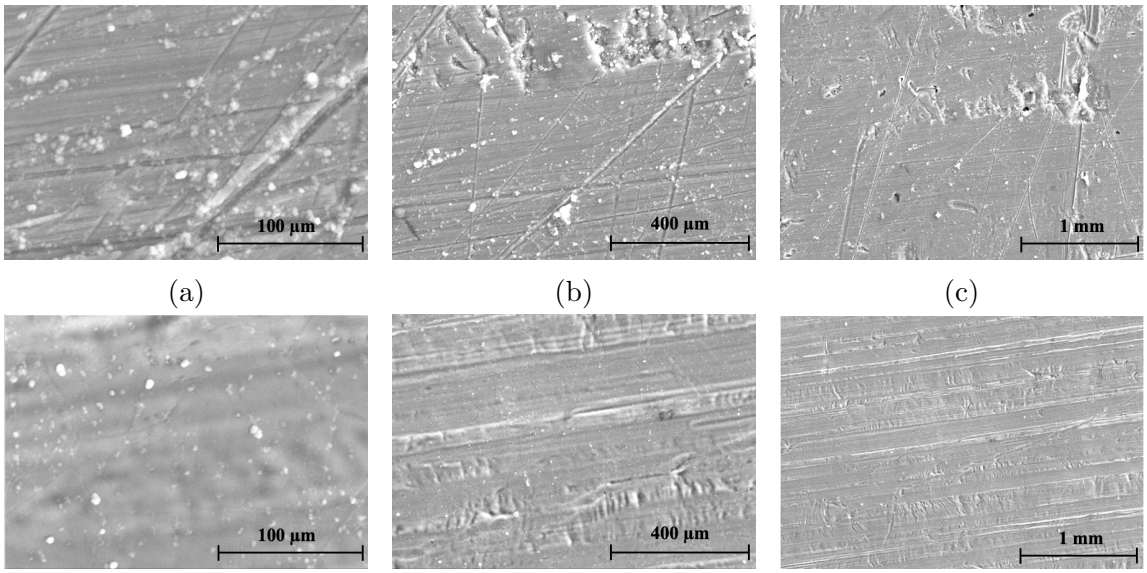

Figure 4.14: SEM images of aluminium, #18, (a - c) and stainless steel, #19, (d - f) coated with 1.5 µm titanium performing magnetron sputtering, captured at different magnifications.

Figure 4.15 shows pictures of the aluminium sample, prior (a) and post (b) corrosion measurements. As can be seen from the pictures, the sample surface was less shiny after performing corrosion measurements. The coating adhered to the surface during the test.

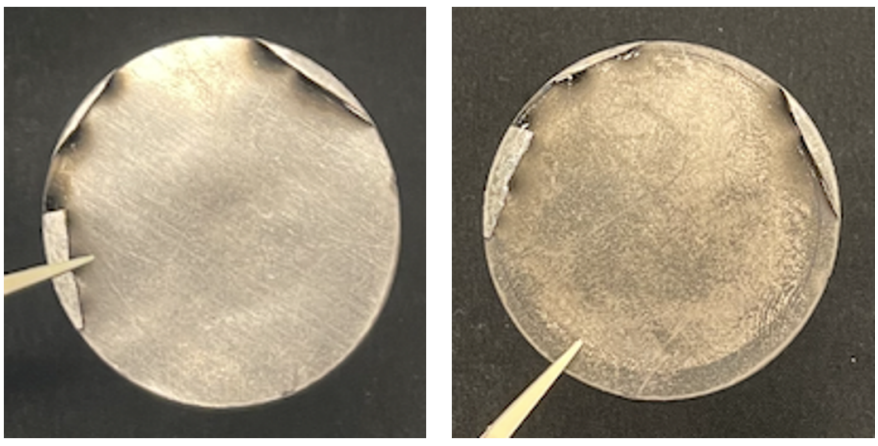

Figure 4.15: Pictures of aluminium coated with 1.5 µm Ti performing magnetron sputtering, prior (a) and post (b) corrosion measurements.

Corrosion Measurements

The results of polarisation on both samples are shown in Figure 4.16. From Figure 4.16b it can be seen that the measured corrosion potential of aluminium was slightly lower than the one measured on stainless steel. After reaching this potential, the current response of aluminium increased significantly as can be seen in Figure 4.16a. According to the low measured current density, the stainless steel sample was passivated at this potential.

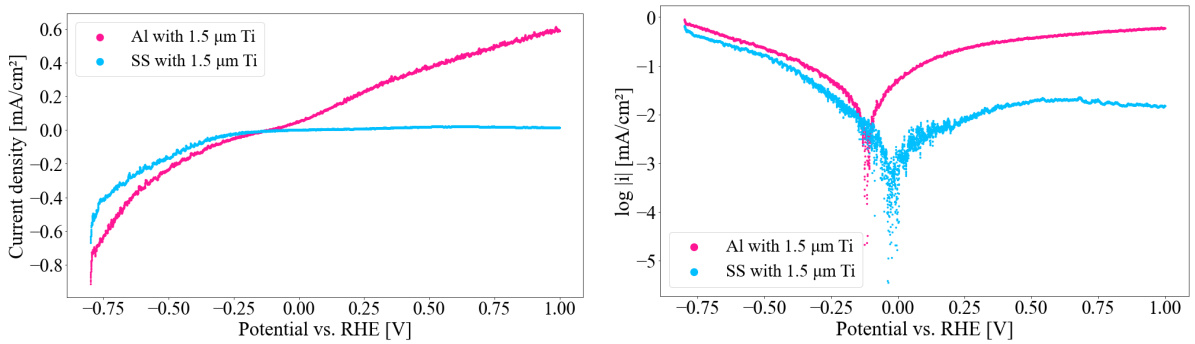

(a) (b)

Figure 4.16: Polarisation curves of coated aluminium, #18 (pink), and stainless steel, #19 (blue). The tests were performed in 0.1 M Na_2SO_4 electrolyte, pH 3 at 70°C. Sweep rate: 1 mV s^{-1}, sweeping from -0.8 - 1 V. Current density plotted against potential (a) and log |i| against potential (b).

Figure 4.17 shows the current transients of aluminium, #18, (a) and stainless steel, #19, (b) coated with 1.5 µm by magnetron sputtering when applying a constant potential of 1 V for 1 hour. The current response of the stainless steel sample decreased rapidly and stabilised around 1 µA cm^{-2}, while the current response of aluminium continued to increase with time. During the first minutes, the current density on aluminium was around 0.4 mA cm^{-2} before it suddenly increased to 0.6 mA cm^{-2} and continued to increase.

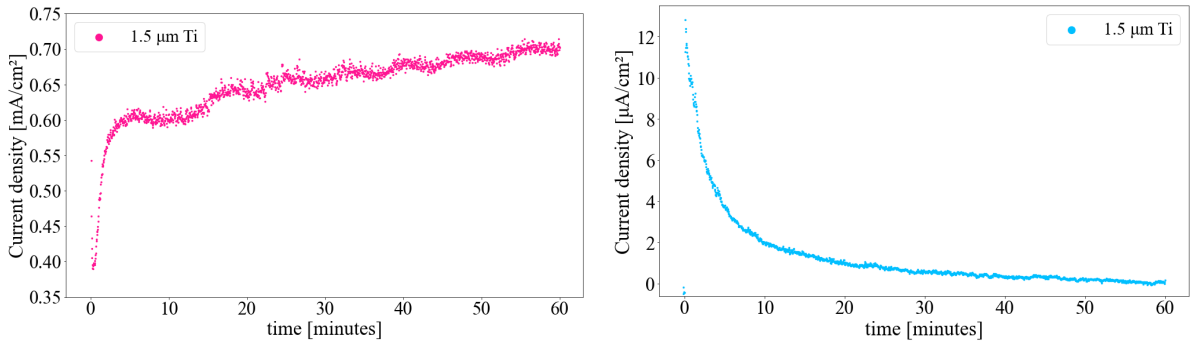

(a) (b)

Figure 4.17: Chronoamperometric scans on coated aluminium, #18, (a) and coated stainless steel, #19, (b) in 0.1 M Na_2SO_4 electrolyte, pH 3 at 70°C. The potential was kept at 1 V for 1 hour. Notice the unit difference.

Interfacial Contact Resistance

The measured interfacial contact resistances of samples no. 18 and 19 are given in Table 4.3. Before corrosion measurements, the samples obtained similar resistances. However, both samples showed an increase in contact resistance after performing electrochemical measurements, and the increase was most significant for the stainless steel sample. Since the polarisation curve of stainless steel (Figure 4.16) indicated passivation, this increase was probably caused by oxide formation during electrochemical tests.

Table 4.3: Interfacial contact resistances at a compaction pressure of 140 N cm^{-2} of one aluminium and one stainless steel sample coated with 1.5 µm titanium by performing magnetron sputtering, before and after corrosion measurements.

Sample no.	**Substrate**	**Coating/characterisation**	**ICR at 140 N cm^{-2} [mΩ cm^2]**
18	Al	1.5 µm Ti	8.4±1.7
		After LSV & CA, 1 h	17.6±3.5
19	SS	1.5 µm Ti	8.8±1.8
		After LSV & CA, 1 h	22.3±4.4

4.3 Oxides as Adhesion Layer

Surface Characterisation before Corrosion Measurements

SEM pictures of the sample surfaces after applying either 5 nm Al_2O_3, #20, (a - c) or 5 nm TiO_2, #21, (d - f) by ALD and 200 nm titanium by performing e-beam evaporation are shown in Figure 4.18. Some pits were present on the samples, and according to the images, the sample surfaces appeared similar independent of the type of adhesion layer.

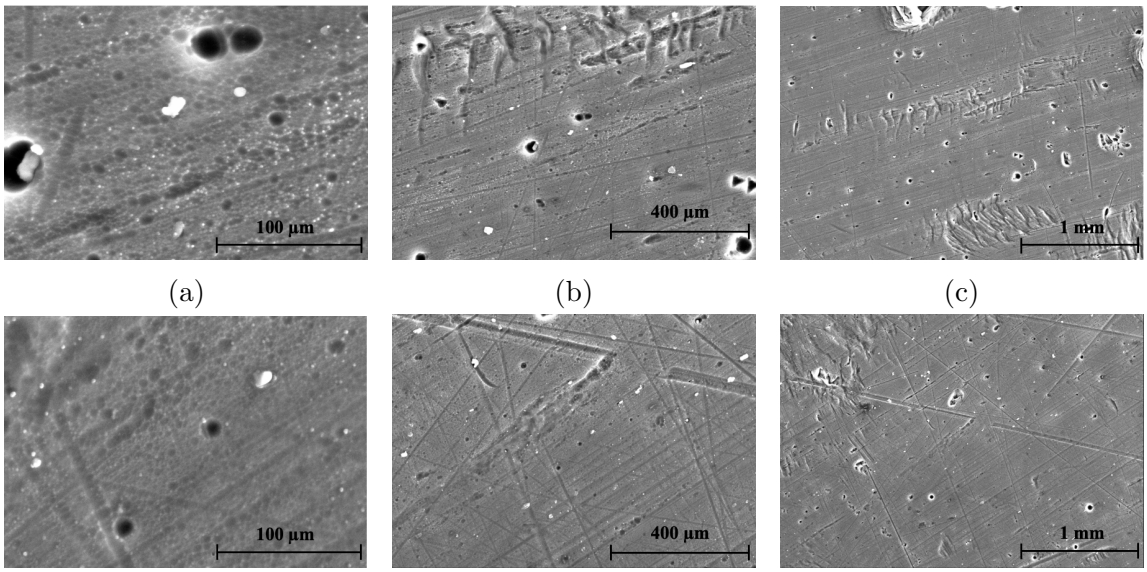

Figure 4.18: SEM images of aluminium coated with either 5 nm Al_2O_3, #20, (a - c) or TiO_2, #21, (d - f) and 200 nm Ti, captured at different magnifications.

Corrosion Measurements

The results of linear sweep voltammetry on samples no. 20 and 21 are shown in Figure 4.19. As can be seen from Figure 4.19b, the measured corrosion potential of the sample having TiO_2 as adhesion layer was slightly higher than the one having Al_2O_3 as adhesion layer. In general, lower current density was measured on the sample coated with TiO_2 and titanium.

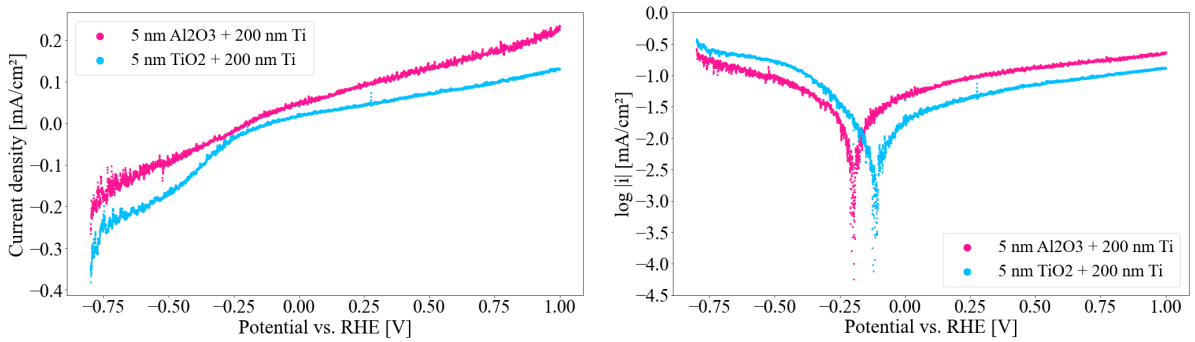

Figure 4.19: Linear sweep voltammetry performed on coated aluminium, #20 (pink) and #21 (blue), in 0.1 M Na_2SO_4 electrolyte, pH 3 at 70°C. Sweep rate: 1 mV s^{-1}, sweeping from -0.8 - 1 V. Current density plotted against potential (a) and log |i| against potential (b).

Potentiostatic measurements confirmed lower corrosion current on sample no. 21 than on sample no. 20, as shown in Figure 4.20. This may indicate better adhesion between

TiO_2 and Ti than between Al_2O_3 and Ti, as well as better corrosion resistance of titanium oxide compared to aluminium oxide in the simulated PEMFC environment. However, the current density increased linearly for both samples, indicating an increased corrosion rate over time. In addition, the coatings fell partially off when the experiments were done, and the samples were rinsed in deionised water.

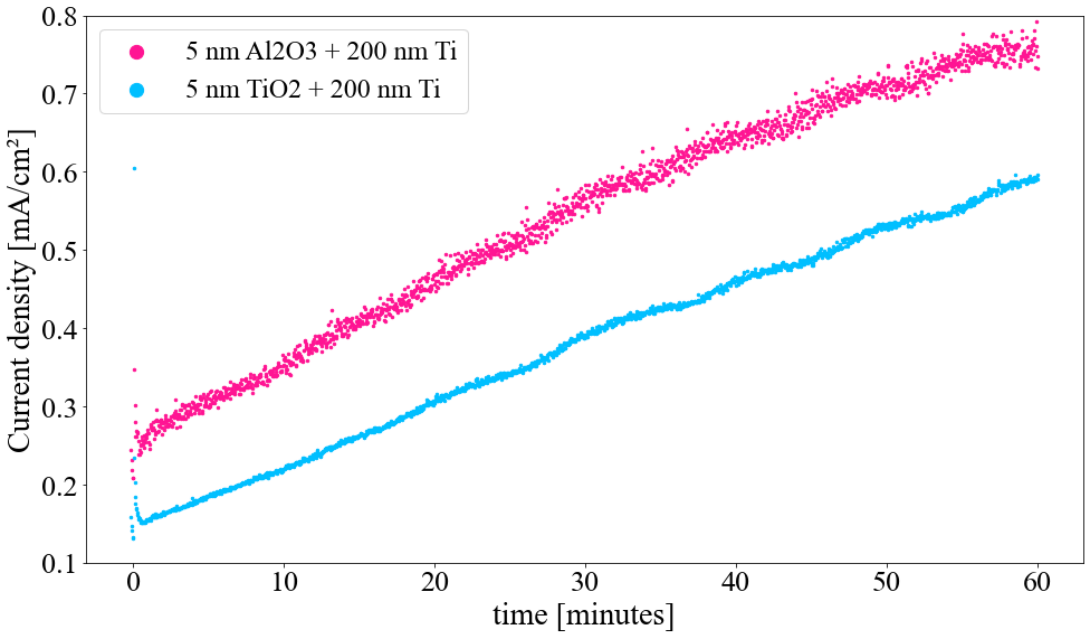

Figure 4.20: Chronoamperometric scans on coated aluminium, #20 (pink) and #21 (blue), in 0.1 M Na_2SO_4 electrolyte, pH 3 at 70°C. The potential was kept at 1 V for 1 hour.

Interfacial Contact Resistance

Measured contact resistances before and after performing corrosion measurements are given in Table 4.4. The lowest measurements were obtained on sample no. 20.

Table 4.4: Interfacial contact resistances at a compaction pressure of 140 N cm^{-2} of coated aluminium before and after performing corrosion measurements. Coating materials and thickness are specified in the table.

Sample no.	**Treatment/coating**	**ICR at 140 N cm^{-2} [mΩ cm^2]**
20	5 nm Al_2O_3 + 200 nm Ti	18.1±3.6
	After LSV & CA, 1 h	26.5±5.3
21	5 nm TiO_2 + 200 nm Ti	37.8±7.5
	After LSV & CA, 1 h	35.0±7.0

The measured contact resistances of the samples coated with various thickness of Al_2O_3 and TiO_2 by ALD are given in Table 4.5. As can be seen from the measured values, the conductivity of titanium oxide is slightly higher than the conductivity of aluminium

oxide. According to these values and theoretical values (Table 2.1), the ICR of sample no. 21 should have been lower than the one of sample no. 20. From Table 4.5 it can be seen that increasing oxide thickness resulted in increased contact resistance. None of the samples could meet the target outlined by the DOE (> 10 mΩ cm^2), and the oxide layer should be as thin as possible to obtain samples with low contact resistances.

Table 4.5: Interfacial contact resistances at a compaction pressure of 140 N cm^{-2} of samples coated with variable aluminium- or titanium oxide thickness.

Sample no.	**Coating**	**ICR at 140 N cm^{-2} [mΩ cm^2]**
22	5 nm Al_2O_3	92.7±18.4
23	2 nm Al_2O_3	64.5±12.8
24	1 nm Al_2O_3	30.1±6.0
25	5 nm TiO_2	71.6±14.2
26	2 nm TiO_2	45.1±9.0
27	1 nm TiO_2	28.2±5.6

4.4 Oxides as Main Coating Layer

4.4.1 Titanium Oxide

Corrosion Measurements

The results of electrochemical measurements performed on aluminium samples coated with aluminium oxide and variable thickness of titanium oxide are shown below. As can be seen in Figure 4.21, coating aluminium with Al_2O_3 and TiO_2 resulted in low corrosion currents, below 20 µA cm^{-2}. A small reduction in current response with increasing TiO_2 thickness was observed.

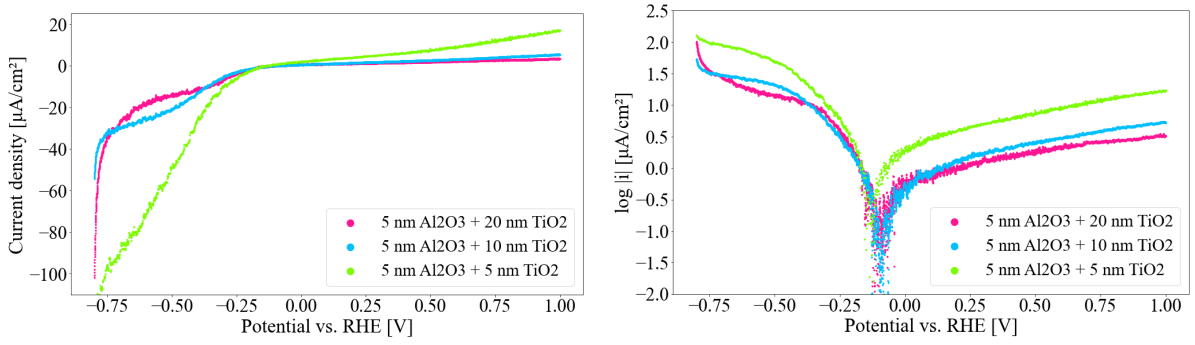

(a) (b)

Figure 4.21: Polarisation curves of coated aluminium, #28 (pink), #29 (blue), and #30 (green), in 0.1 M Na_2SO_4 electrolyte, pH 3 at 70°C. Sweep rate: 1 mV s^{-1}, sweeping from -0.8 - 1 V. Current density plotted against potential (a) and log |i| against potential (b).

The results of potentiostatic measurements on sample no. 28, 29 and 30 are shown in Figure 4.22. When keeping a constant potential of 1 V for 1 hour, the lowest corrosion current was obtained on the sample with the thickest, 20 nm, titanium oxide layer. The increasing corrosion currents over time indicated coating breakdown.

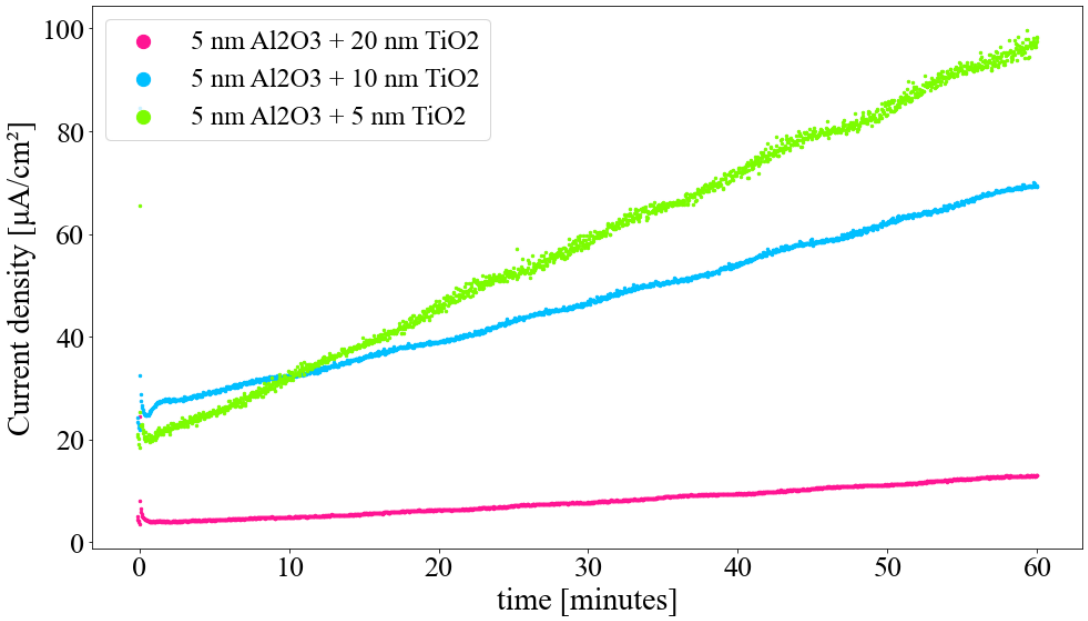

Figure 4.22: Chronoamperometric scans on coated aluminium, #28 (pink), #29 (blue), and #30 (green), performed in 0.1 M Na_2SO_4 electrolyte, pH 3 at 70°C. The potential was kept at 1 V for 1 hour.

Surface Characterisation after Corrosion Measurements

EDS analysis suggested that the surface composition of aluminium coated with aluminium oxide and titanium oxide after corrosion measurements were aluminium, oxygen and titanium. As can be seen from Table 4.6, the amount of titanium decreased with decreasing titanium oxide thickness. The analysis also confirmed that titanium was left on the surface after electrochemical tests had been performed.

Table 4.6: Results of EDS analysis performed on aluminium coated with 5 nm Al_2O_3 and variable TiO_2 thickness after corrosion measurements were performed.

Sample no.	**Coating**	**Al**	**O**	**Ti**
28	5 nm Al_2O_3 + 20 nm TiO_2	93.72%	3.52%	2.76%
29	5 nm Al_2O_3 + 10 nm TiO_2	95.98%	2.42%	1.60%
30	5 nm Al_2O_3 + 5 nm TiO_2	97.48%	1.77%	0.75%

SEM pictures of the samples after corrosion measurements were complete are shown in Figure 4.23. Pits were visible on the sample surfaces. No significant difference in surface

morphology was observed.

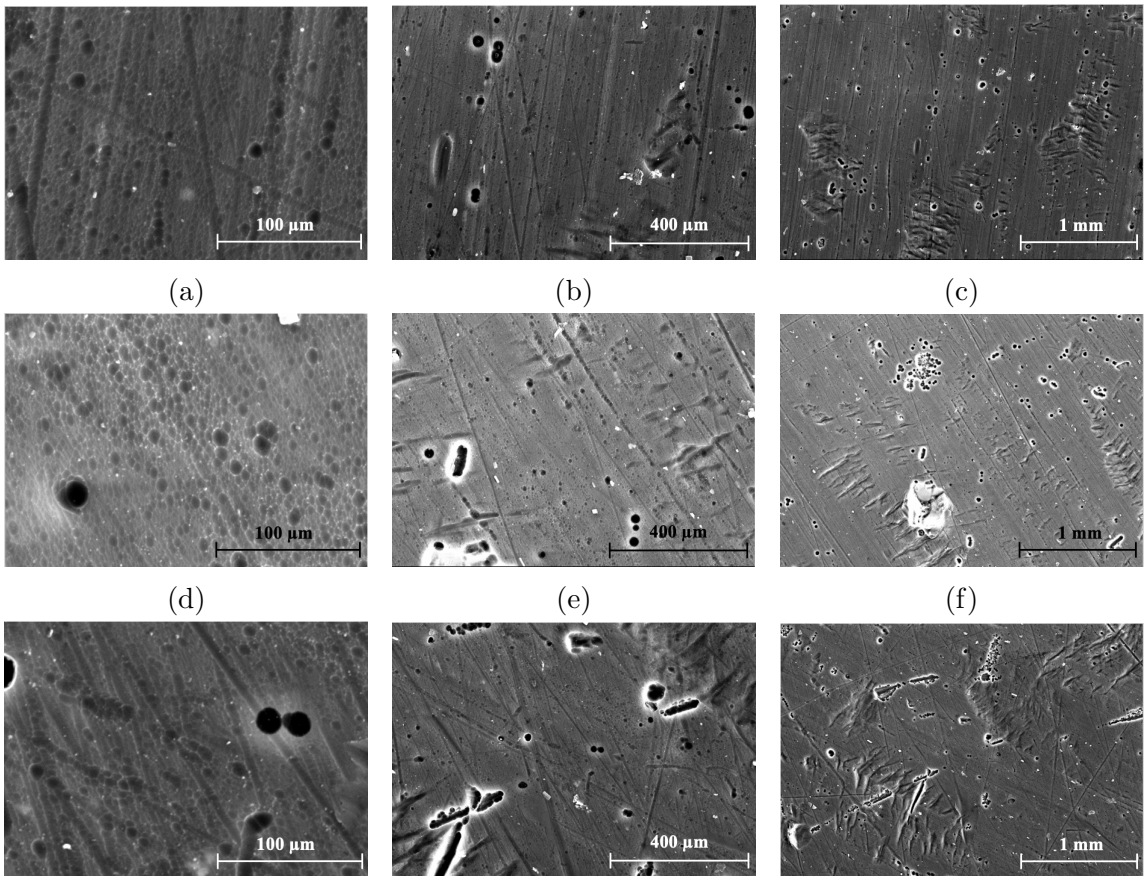

Figure 4.23: SEM images of aluminium coated with 5 nm Al_2O_3 and either 20 nm TiO_2, #28, (a - c) or 10 nm TiO_2, #29, (d - f) or 10 nm TiO_2, #30, (g - i), after performing corrosion measurements. Notice the scale difference.

Interfacial Contact Resistance

Measured contact resistances before and after performing corrosion measurements are given in Table 4.8. All samples obtained contact resistances well above the goal of below 10 mΩ cm^2. After corrosion measurements, the ICR of the samples decreased, indicating dissolution of the oxides during electrochemical experiments. Aluminium coated with 5 nm Al_2O_3 and 5 nm TiO_2 showed the lowest ICR. However, this sample showed high corrosion current, much higher than the goal (< 1 µA cm^{-2}) outlined by the DOE.

Table 4.7: Interfacial contact resistances at a compaction pressure of 140 N cm^{-2} of coated aluminium samples before and after performing corrosion measurements. Coating materials and thickness are specified in the table.

Sample no.	**Coating/characterisation**	**ICR at 140 N cm^{-2} [mΩ cm^2]**
28	5 nm Al_2O_3 + 20 nm TiO_2	200.4±39.9
	After LSV & CA, 1 h	157.5±31.3
29	5 nm Al_2O_3 + 10 nm TiO_2	201.9±40.2
	After LSV & CA, 1 h	185.8±37.0
30	5 nm Al_2O_3 + 5 nm TiO_2	150.5±30.0
	After LSV & CA, 1 h	136.2±27.1

4.4.2 Aluminium Oxide

Corrosion Measurements

The results of LSV on aluminium coated with 5 nm Al_2O_3 (#31 and #32) are shown in Figure 4.24a. Figure 4.24b shows the result of polarising aluminium coated with 5 nm TiO_2 and 5 nm Al_2O_3 (#33). A remarkable difference in the current response was observed. It was clear that the titanium oxide layer underneath aluminium oxide greatly impacted the corrosion resistance in the simulated PEM fuel cell environment.

As can be seen from Figure 4.24c, the measured corrosion potentials were low, and there were only minor differences in measured corrosion potentials for the three samples. When reaching a potential of around 0 V, the current responses of samples no. 31 and 32 were similar to the current response of uncoated aluminium at the same potential (Figure 4.2a (pink)).

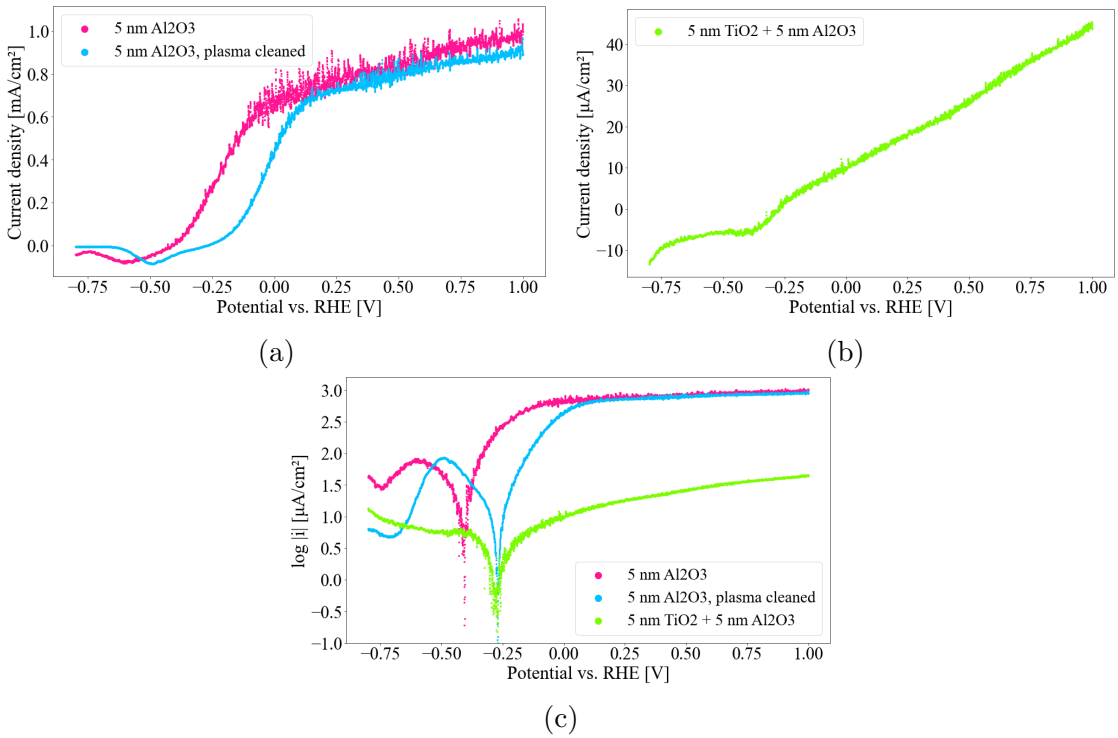

Figure 4.24: Polarisation curves of coated aluminium samples, #31 (pink), #32 (blue), and #33 (green). The tests were performed in 0.1 M Na_2SO_4, pH 3 at 70°C. Sweep rate: 1 mV s^{-1}, sweeping from -0.8 - 1 V. Current density plotted against potential (a and b) and log |i| against potential (c). Notice the unit difference.

As can be seen in Figure 4.25, the resulting current transients of aluminium coated with aluminium oxide were similar to the current transient of uncoated aluminium in pH 3 electrolyte (Fig. 4.3a). The plasma cleaned sample obtained a slightly lower current transient, although the difference was small. Again, the current response of the sample coated with both titanium oxide and aluminium oxide was lower than the ones measured on the samples coated with only aluminium oxide. During 1 hour, the current response of aluminium coated with TiO_2 and Al_2O_3 increased with around 0.2 mA cm^{-2}.

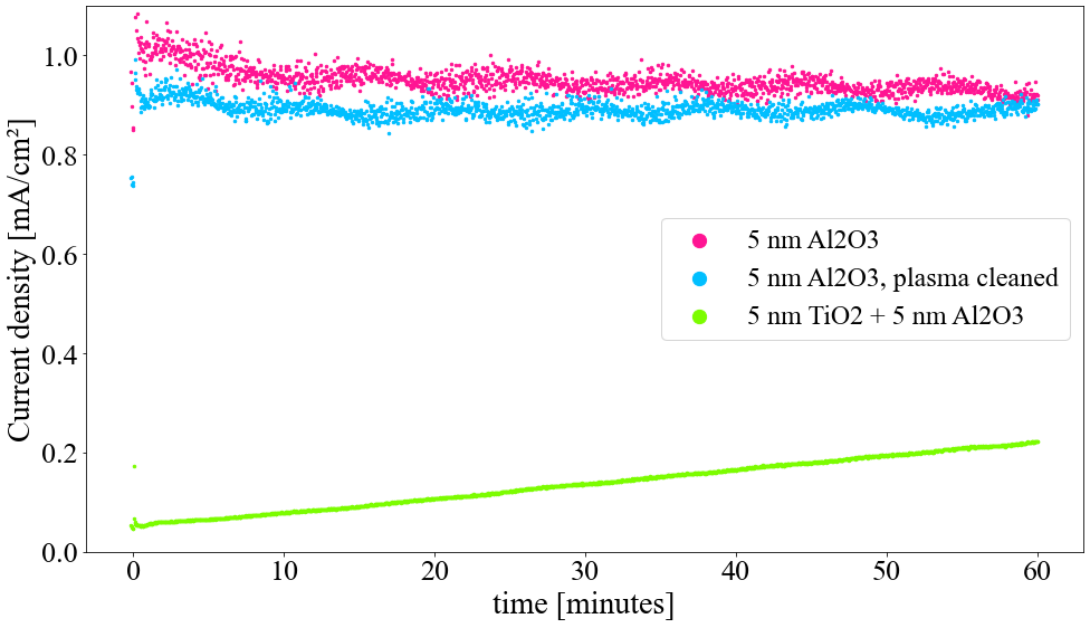

Figure 4.25: Chronoamperometric scans on coated aluminium samples, #31 (pink), #32 (blue), and #33 (green) in 0.1 M Na_2SO_4 electrolyte, pH 3 at 70°C. The potential was kept at 1 V for 1 hour.

Interfacial Contact Resistance

Measured contact resistances of the samples before and after performing corrosion measurements are given in Table 4.8. All samples obtained resistances above the goal of below 10 mΩ cm^2. Additionally, the samples showed a decrease in ICR after electrochemical measurements, indicating coating breakdown.

Table 4.8: Interfacial contact resistances of coated aluminium samples at a compaction pressure of 140 N cm^{-2} before and after performing corrosion measurements. Coating materials and thickness are specified in the table.

Sample no.	**Coating/characterisation**	**ICR at 140 N cm^{-2} [mΩ cm^2]**
31	5 nm Al_2O_3	124.8±24.8
	After LSV & CA, 1 h	84.6±16.8
32	5 nm Al_2O_3, plasma cleaned	123.6±24.6
	After LSV & CA, 1 h	60.3±12.0
33	5 nm TiO_2 + 5 nm Al_2O_3	160.5±31.9
	After LSV & CA, 1 h	28.3±5.6

4.5 Titanium Nitride as Main Coating Layer

Surface Characterisation before Corrosion Measurements

EDS analysis suggested that the surface composition of the aluminium samples coated with titanium nitride by conducting magnetron sputtering and gold by performing e-beam evaporation was as given in Table 4.9. Almost no nitrogen was detected on the samples. According to the thickness of the gold layer compared to the thickness of the titanium nitride layer, higher amounts of titanium and nitrogen were expected. This may be due to the use of too high acceleration voltage.

Table 4.9: Results of EDS analysis performed on coated aluminium samples before corrosion measurements were performed.

Sample no.	Coating	Al	Au	C	Ti	O	N
35	20 nm TiN + 10 nm Au	77.3%	12%	4%	4.1%	2.3%	0.3%
36	20 nm TiN + 10 nm Au, polished	75.9%	12.5%	5.5%	3.9%	1.9%	0.3%

SEM images of sample no. 35 (a - c) and sample no. 36 (d - f), before the gold layer was applied, are shown in Figure 4.26. The surface of the polished sample, #36, was uniform and textured, while the unpolished one contained visible pits and scratches, randomly distributed over the surface. The samples were also pictured after applying the gold layer, but the surface characteristics were the same as without gold and the pictures are therefore not included here.

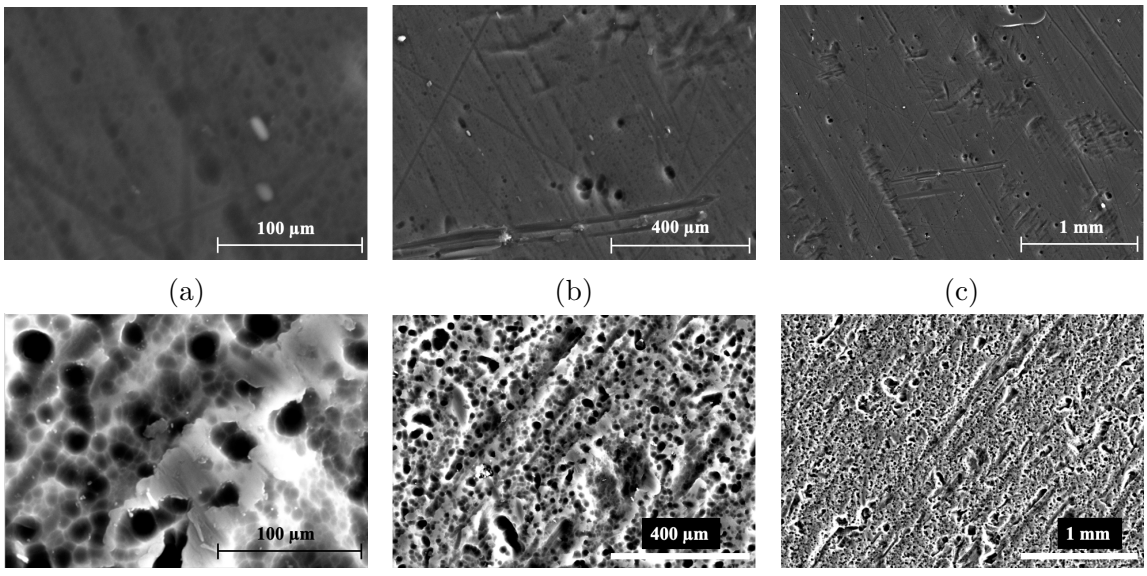

Figure 4.26: SEM images of unpolished aluminium coated with titanium nitride, #35, (a - c) and polished aluminium coated with titanium nitride, #36, (d - f). Notice the scale difference.

Corrosion Measurements

The polarisation curve of aluminium coated with titanium nitride, #34, is shown in Figure 4.27. The current response was below -0.5 µA cm^{-2} until a potential of around 0.2 V was reached. By the end of the scan, the current density was slightly higher than 1.5 µA cm^{-2}. A low corrosion current and a relatively high corrosion potential were measured.

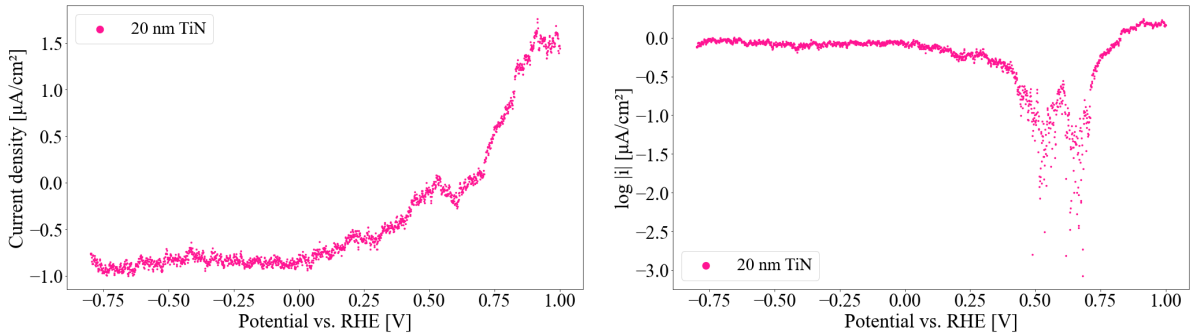

(a) (b)

Figure 4.27: Polarisation curve of coated aluminium, #34, in 0.1 M Na_2SO_4 electrolyte, pH 3 at 70°C. Sweep rate: 1 mV s^{-1}, sweeping from -0.8 - 1 V. Current density plotted against potential (a) and log |i| against potential (b).

Figure 4.28 shows the polarisation curves of two aluminium samples coated with titanium nitride and gold, #35 and #35. One of the samples (#36) was polished before coating deposition, and this sample showed better performance than the unpolished one in terms of lower current density and higher corrosion potential. However, compared to the sample without the gold layer, #34 (Fig. 4.27), the current responses are much higher.

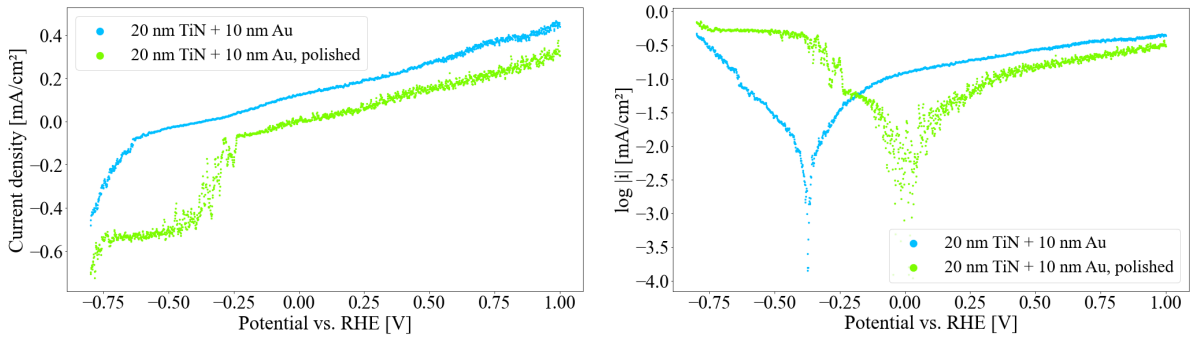

(a) (b)

Figure 4.28: Polarisation curves of coated aluminium, #35 (blue) and #36 (green), in 0.1 M Na_2SO_4 electrolyte, pH 3 at 70°C. Sweep rate: 1 mV s^{-1}, sweeping from -0.8 - 1 V. Current density plotted against potential (a) and log |i| against potential (b).

The results of chronoamperometric scans are shown in Figures 4.29 and 4.30. Again, the corrosion current on sample no. 34 was much lower than those measured on sample no.

35 and 36. As can be seen from the inset highlighting of the last 21 hours of the scan in Figure 4.29, the current transient was relatively stable around 0 - 1 µA cm^{-2} after 3 hours until 17.5 hours and then from 20 hours until the end of the scan. These measurements are close to the target outlined by the DOE (< 1 µA cm^{-2}), although no active peak should be present. The coatings on sample no. 35 and 36 failed after 3 - 4 hours of testing and the current responses were similar to those obtained on uncoated aluminium and even higher for sample no. 35.

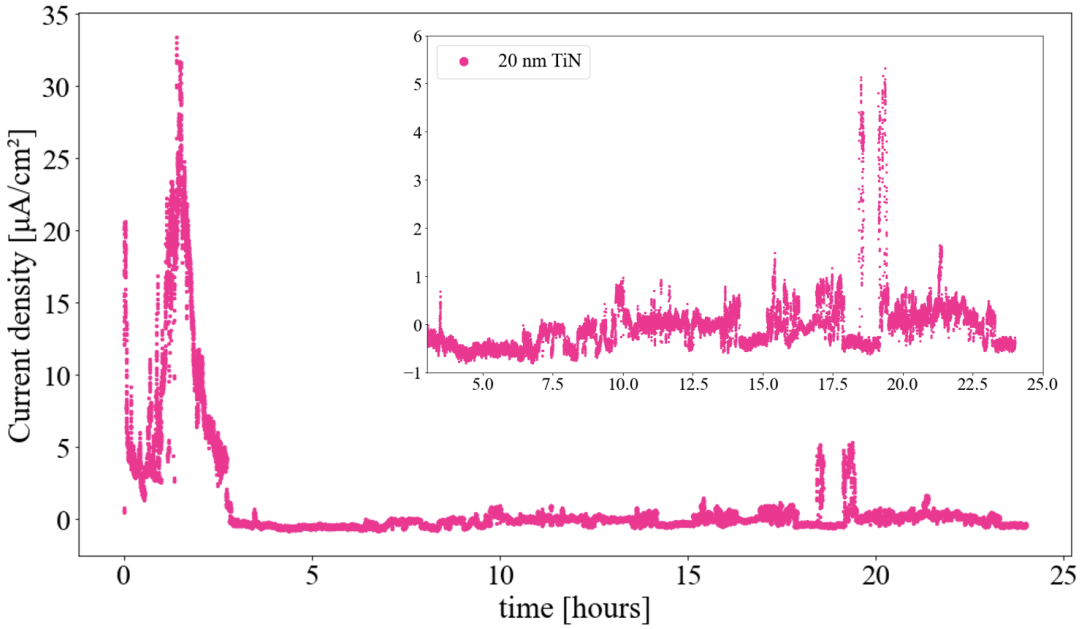

Figure 4.29: Chronoamperometric scan on coated aluminium, #34, in 0.1 M Na_2SO_4 electrolyte, pH 3 at 70°C. The potential was kept at 1 V for 24 hours.

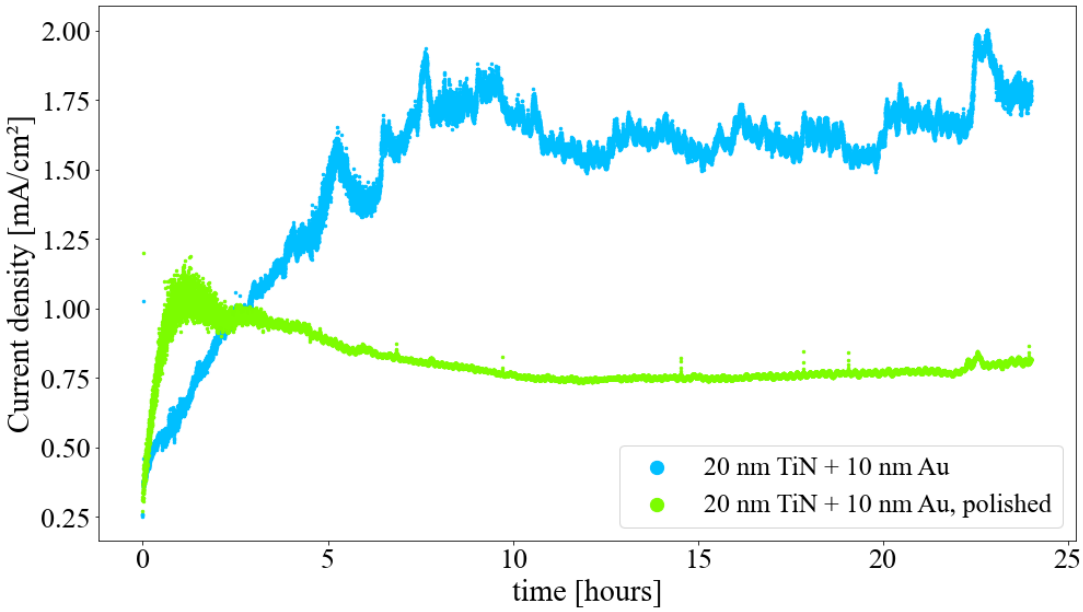

Figure 4.30: Chronoamperometric scans on coated aluminium, #35 (blue) and #36 (green), in 0.1 M Na_2SO_4 electrolyte, pH 3 at 70°C. The potential was kept at 1 V for 24 hours.

Interfacial Contact Resistance

Interfacial contact resistances of coated aluminium samples before and after performing corrosion measurements are given in Table 4.10. The contact resistance of sample no. 34 was high before corrosion measurements and even higher after. This was probably caused by oxide formation on the surface during corrosion measurements. The samples coated with titanium nitride and gold obtained ICR-values below the goal of 10 mΩ cm^2, but also these samples showed an increase in contact resistance after electrochemical experiments were performed.

Table 4.10: Interfacial contact resistances of coated aluminium samples at a compaction pressure of 140 N cm^{-2}, before and after performing corrosion measurements. Coating materials and thickness are specified in the table.

Sample no.	**Coating/characterisation**	**ICR at 140 N cm^{-2} [mΩ cm^2]**
34	20 nm TiN	131.8±26.2
	After LSV & CA, 24 h	249.6±49.7
35	20 nm TiN + 10 nm Au	9.8±2.0
	After LSV & CA, 24 h	23.9±4.8
36	20 nm TiN + 10 nm Au, polished	8.2±1.6
	After LSV & CA, 24 h	28.1±5.6

Surface Characterisation after Corrosion Measurements

Post electrochemical measurements, the results of EDS analysis showed that the surface composition of sample no. 34 was as given in Table 4.11. According to the analysis, almost no nitrogen was left on the surface, and the amount of oxygen was high. This result and the high ICR point toward oxide formation during corrosion tests. The detected amount of carbon may be due to contamination from the GDL that was placed on the top of the sample during ICR-measurements.

Table 4.11: Results of EDS analysis performed on coated aluminium after corrosion measurements.

Sample no.	**Coating**	**Al**	**O**	**C**	**S**	**Ti**	**N**
34	20 nm TiN	51.2%	23.8%	17.9%	4%	2.7%	0.5%

Pictures of the sample surface (#34) are shown in Figure 4.31. After corrosion measurements, it looked like a porous layer had formed on the surface. In addition, the sample area that had been exposed to the electrolyte changed colour, as can be seen in Figure 4.32, and this also underpins the theory that an oxide was formed. Since the multilayer coatings on sample no. 35 and 36 failed completely during corrosion measurements, they were not pictured.

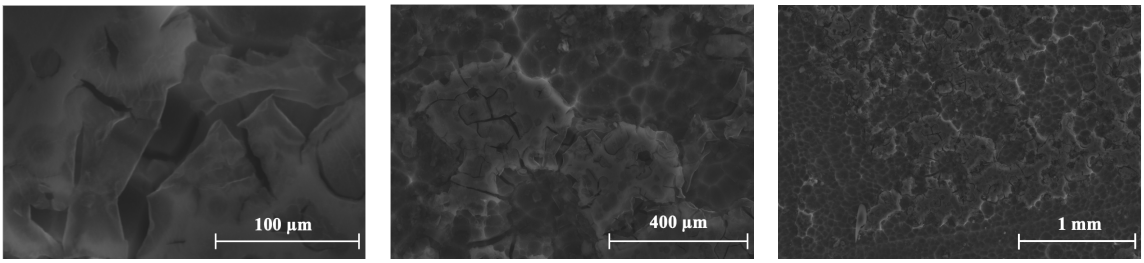

(a) (b) (c)

Figure 4.31: SEM images of coated aluminium, #34, post electrochemical measurements. Notice the scale difference.

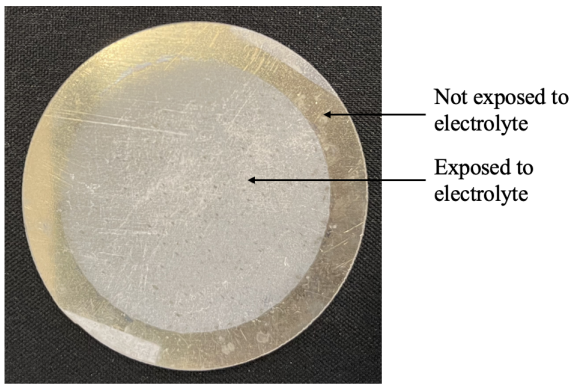

Figure 4.32: Picture of the sample coated with titanium nitride (#34) post corrosion measurements showing how the surface area exposed to electrolyte looked vs. the not exposed area.

4.6 Combining E-beam and Sputtering/ALD

The samples presented in this section were coated with titanium by e-beam evaporation and a second coating layer by performing either magnetron sputtering to deposit titanium nitride or ALD to deposit titanium oxide or hafnium oxide. In Subsection 4.6.1, the results of applying an additional top layer of gold are presented.

Surface Characterisation before Corrosion Measurements

Figure 4.33 shows images of aluminium coated with 200 nm titanium and either 20 nm TiN, #37, (a - c) or 5 nm TiO_2, #38, (d - f). As can be seen from the pictures, there were pits present on the sample surfaces. However, the application of titanium oxide by ALD was thought to result in deposited titanium oxide in the pits/trenches. Since ALD is a CVD method, chemical bonds between titanium and titanium oxide were formed. If the titanium oxide layer successfully managed to cover the pits, the layer could prevent the electrolyte from reaching the substrate.

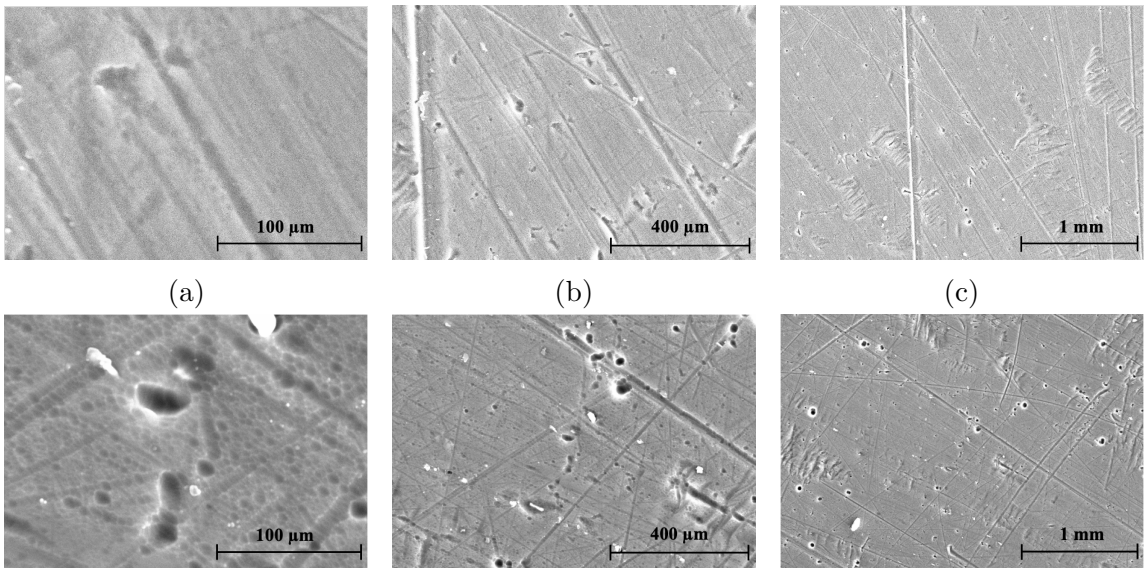

Figure 4.33: SEM images of aluminium coated with 200 nm titanium and either 20 nm TiN, #37, (a - c) or 5 nm TiO_2, #38, (d - f) before electrochemical measurements. Notice the different scale bars.

Corrosion Measurements

The result of polarising sample no. 37 is shown in Figure 4.34. The current response was high and the measured corrosion potential was low.

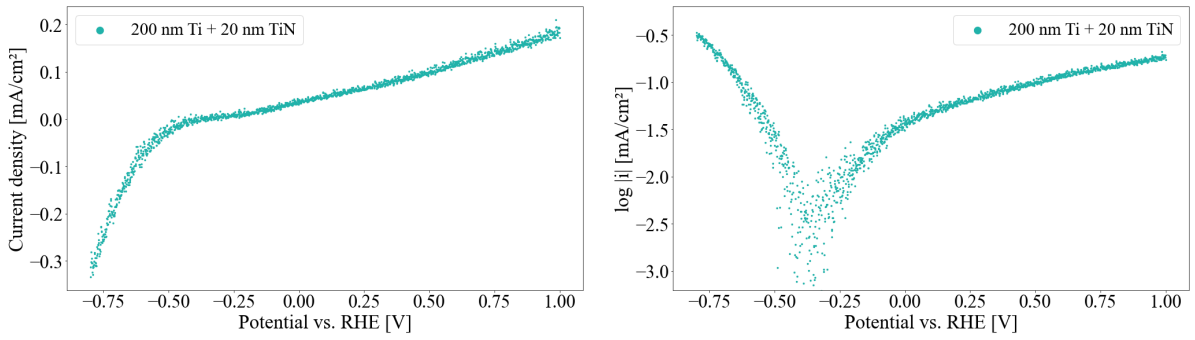

Figure 4.34: Polarisation curve of coated aluminium, #37, in 0.1 M Na_2SO_4 electrolyte, pH 3 at 70°C. Sweep rate: 1 mV s^{-1}, sweeping from -0.8 - 1 V. Current density plotted against potential (a) and log |i| against potential (b).

The results of polarising aluminium coated with 200 nm titanium and 5 nm (#38), 4 nm (#39), 3 nm (#40), 2 nm (#41), and 1 nm (#42) TiO_2, respectively, are shown in Figure 4.35. Samples no. 38 and 40 showed best performance in terms of low current densities.

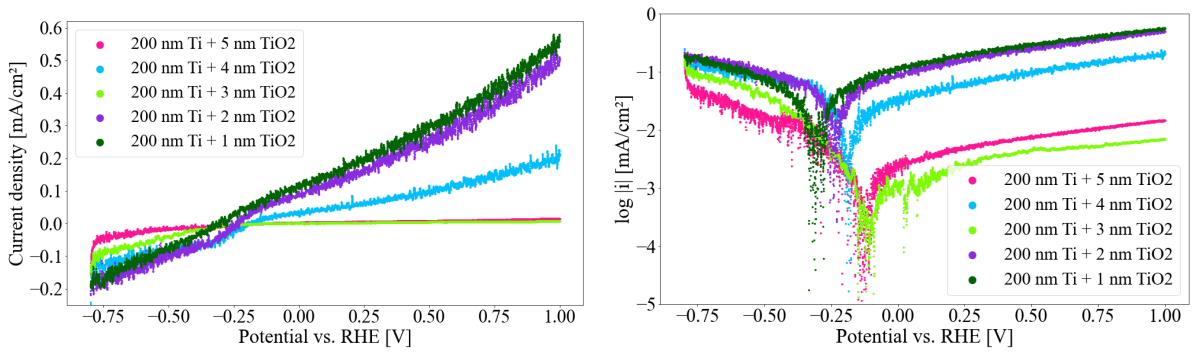

(a) (b)

Figure 4.35: Polarisation curves of coated aluminium samples, #38 (pink), #39 (blue), #40 (green), #41 (purple), and #42 (dark green). The tests were performed in 0.1 M Na_2SO_4 electrolyte, pH 3 at 70°C. Sweep rate: 1 mV s^{-1}, sweeping from -0.8 - 1 V. Current density plotted against potential (a) and log |i| against potential (b).

The resulting current transient of sample no. 37 when performing chronoamperometry is shown in Figure 4.36. During the first 3 hours, the current density increased from 0.2 mA cm^{-2} to 1.1 mA cm^{-2}. The coating layer was still visibly attached to the sample surface after these 3 hours, but according to the current density, this layer did not protect the substrate. After the test was complete, the coating layer fell off when the sample was rinsed in deionised water. Holes through the sample were visible in the contact area between the sample and the gasket after corrosion measurements were complete, as can be seen in Figure 4.37.

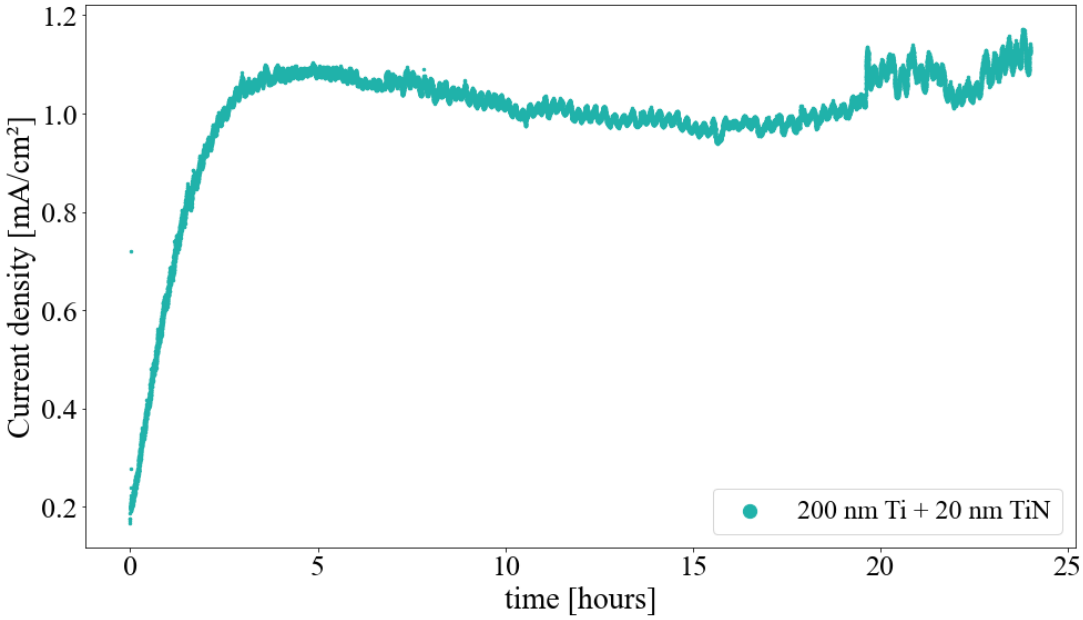

Figure 4.36: Chronoamperometric scan on coated aluminium, #37, in 0.1 M Na_2SO_4 electrolyte, pH 3 at 70°C. The potential was kept at 1 V for 24 hours.

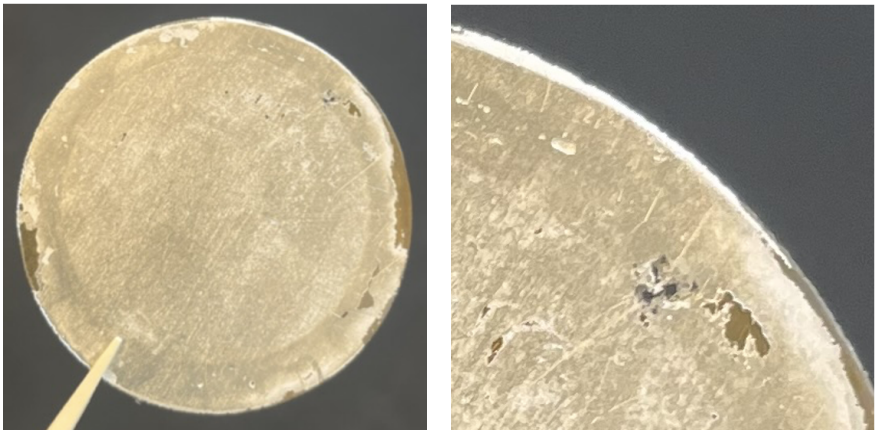

(a) (b)

Figure 4.37: Pictures of sample no. 37 after corrosion measurements were complete (a). Holes were visible in the area where the gasket had been in contact with the sample (b).

A constant potential of 1 V was applied for 1 hour on sample no. 38. The resulting current response is shown in Figure 4.38. The current density increased linearly with time but the coating did not fall off during testing, not even in the O-ring area.

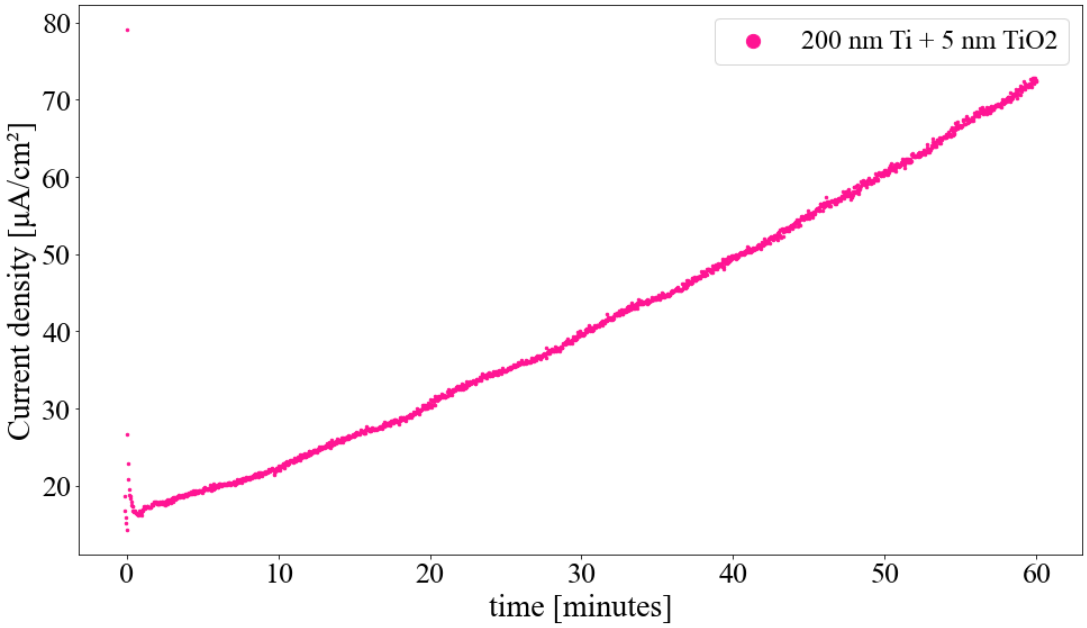

Figure 4.38: Chronoamperometric scan on coated aluminium, #38, in 0.1 M Na_2SO_4 electrolyte, pH 3 at 70°C. The potential was kept at 1 V for 1 hour.

Potentiostatic measurements were performed for 24 hours on samples no. 39, 40, 41, and 42. Figure 4.39 shows the resulting current transients. The sample with 3 nm TiO_2 (#40) excelled from the other samples with a lower current response. This was also the sample where only partial coating failure was observed, while the rest of the coatings failed.

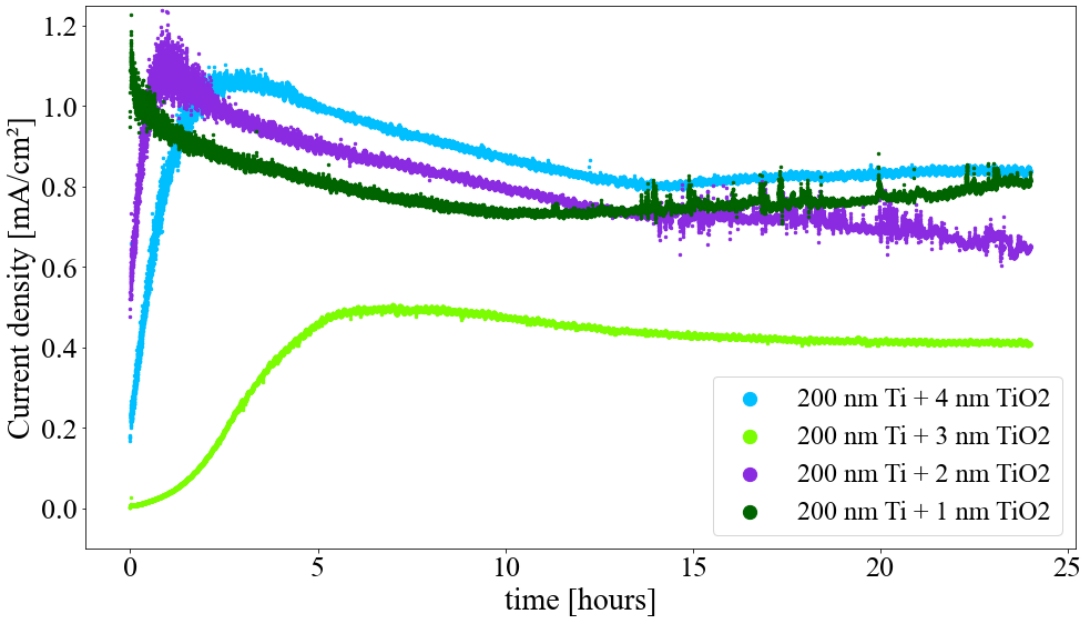

Figure 4.39: Chronoamperometric scans on coated aluminium, #39 (blue), #40 (green), #41 (purple), and #42 (dark green), in 0.1 M Na_2SO_4, pH 3 at 70°C. The potential was kept at 1 V for 24 hours.

Interfacial Contact Resistance

Measured contact resistances before and after corrosion measurements were performed are given in Table 4.12. As can be seen from the table, the contact resistance decreased significantly as the thickness of the titanium oxide layer decreased. After electrochemical measurements all ICR-values increased.

Table 4.12: Interfacial contact resistances of coated aluminium at a compaction pressure of 140 N cm^{-2}, before and after corrosion measurements were performed. Coating materials and thickness are specified.

Sample no.	**Coating/characterisation**	**ICR at 140 N cm^{-2} [mΩ cm^2]**
37	200 nm Ti + 20 nm TiN	113.5±22.6
	After LSV & CA, 24 h	35.4±7.0
38	200 nm Ti + 5 nm TiO_2	54.2±10.8
	After LSV & CA, 1 h	61.2±12.2
39	200 nm Ti + 4 nm TiO_2	19.5±3.9
	After LSV & CA, 24 h	40.4±8.0
40	200 nm Ti + 3 nm TiO_2	11.8±2.3
	After LSV & CA, 24 h	61.8±12.3
41	200 nm Ti + 2 nm TiO_2	7.2±1.4
	After LSV & CA, 24 h	Unstable
42	200 nm Ti + 1 nm TiO_2	6.4±1.3
	After LSV & CA, 24 h	69.9±13.9

Surface Characterisation after Corrosion Measurements

Samples no. 37 and 38 were pictured after corrosion measurements were completed and are shown in Figure 4.40. Sample no. 38 was pictured using a field emission SEM.

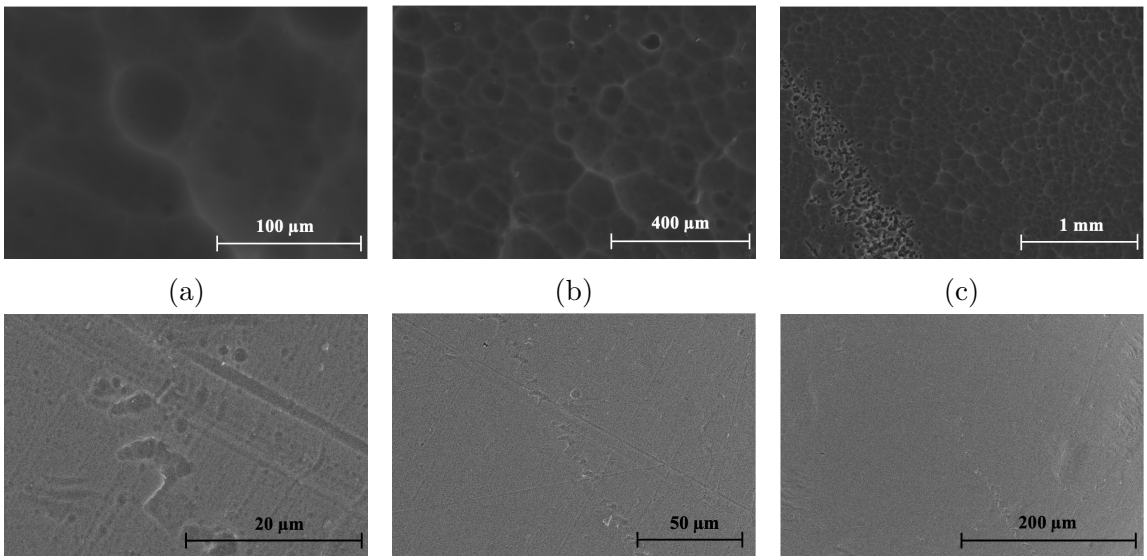

Figure 4.40: SEM images of sample no. 37 (a - c) and sample no. 38 (d - f) after electrochemical measurements. Notice the different scale bars.

4.6.1 Gold Top Layer

Surface Characterisation before Corrosion Measurements

EDS analysis suggested that the surface compositions of samples no. 43, 44, and 45 were as given in Table 4.13 before performing corrosion measurements. The EDS results confirmed that the HfO_2- and TiO_2-deposition had been successful. However, nitrogen was not detected on sample no. 43.

Table 4.13: Results of EDS analysis performed on coated aluminium samples before corrosion measurements.

Sample no.	**Coating**	**Al**	**Ti**	**Au**	**O**	**N**	**Hf**	**C**
43	200 nm Ti + 20 nm TiN + 10 nm Au	65.9%	15.4%	4.5%	4.2%	-	-	10%
44	200 nm Ti + 20 nm HfO_2 + 10 nm Au	65.8%	14.8%	4.6%	5.3%	-	5.4%	4.2%
45	200 nm Ti + 5 nm TiO_2 + 10 nm Au	73.5%	17.7%	5.1%	3.7%	-	-	-

SEM pictures of the sample surfaces coated with 200 nm titanium, 20 nm TiN, #43, (a - c), 20 nm HfO_2, #44, (d - f), or 5 nm TiO_2, #45 and #47, (g - l) and 10 nm gold before corrosion measurements were performed are shown in Figure 4.41. According to the pictures, the polished sample (#47) obtained a more textured surface than the unpolished samples.

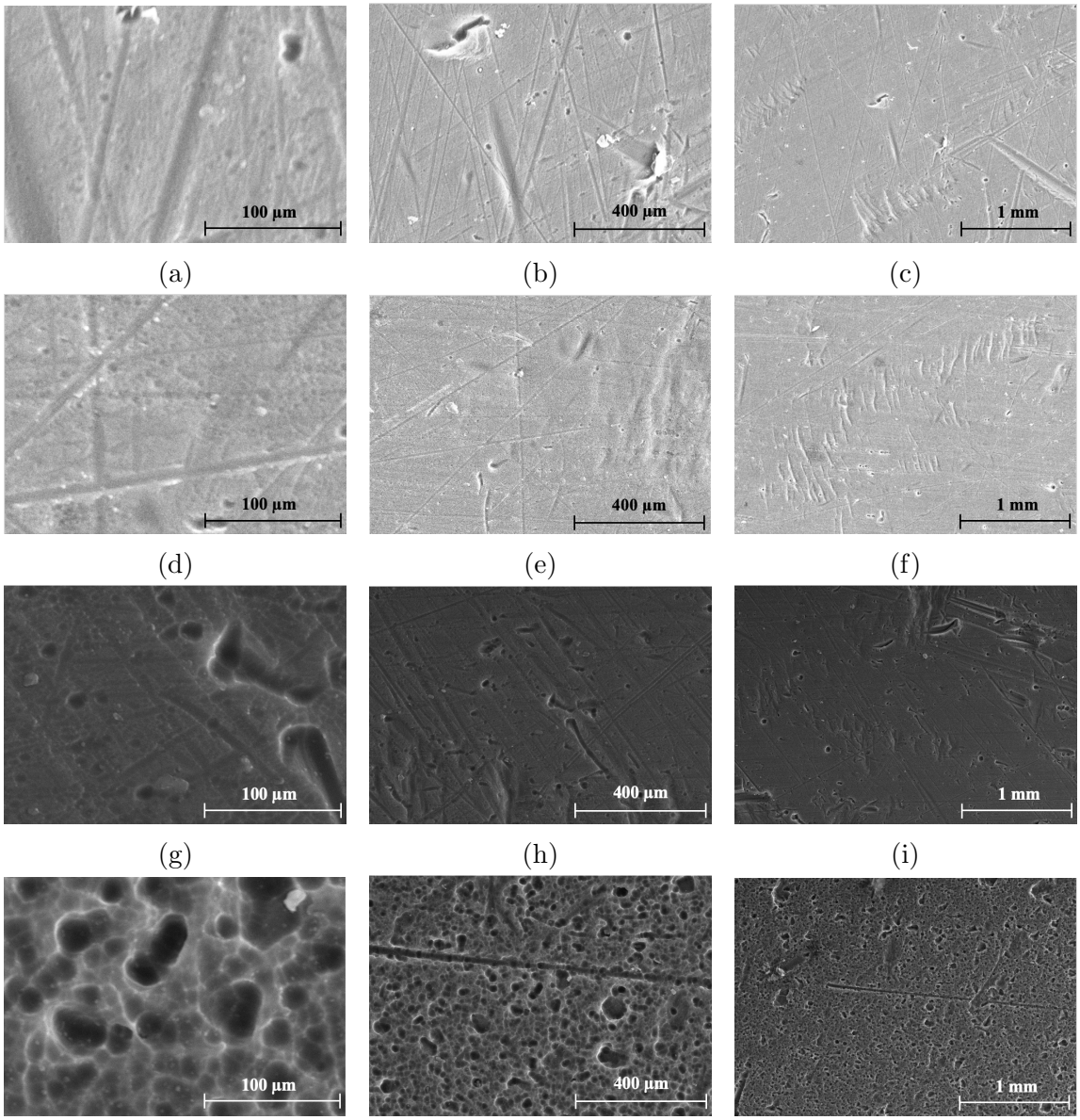

Figure 4.41: SEM images of coated aluminium samples coated with 200 nm titanium, (a - c): 20 nm TiN (#43), (d - f): 20 nm HfO_2 (#44), (g - i): 5 nm TiO_2 (#45), (j - l): 5 nm TiO_2 (#47) and 10 nm gold before electrochemical measurements. Notice the scale difference.

Corrosion Measurements

The current responses of samples no. 43 and 44 when exposed to potentials between -0.8 - 1 V in a simulated PEM fuel cell environment are shown Figure 4.42 and 4.43, respectively. As can be seen from the figures, the polarisation curves were very similar.

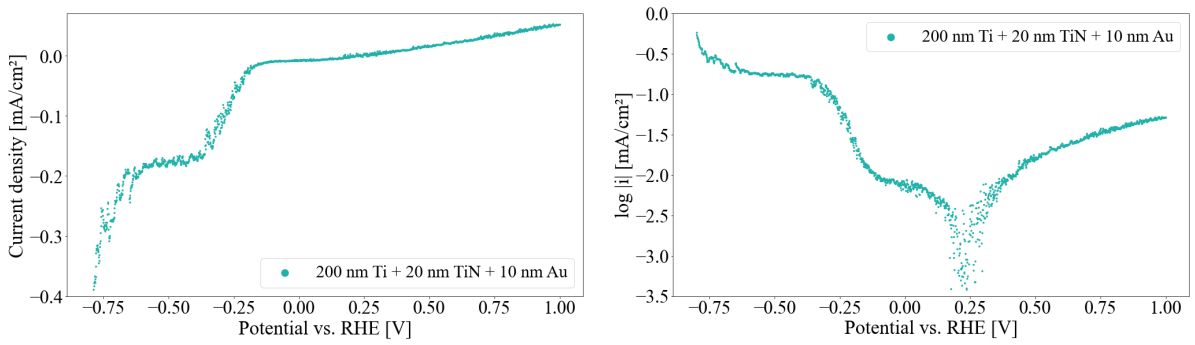

(a) (b)

Figure 4.42: Polarisation curve of coated aluminium, #43. The test was performed in 0.1 M Na_2SO_4 electrolyte, pH 3 at 70°C. Sweep rate: 1 mV s^{-1}, sweeping from -0.8 - 1 V. Current density plotted against potential (a) and log |i| against potential (b).

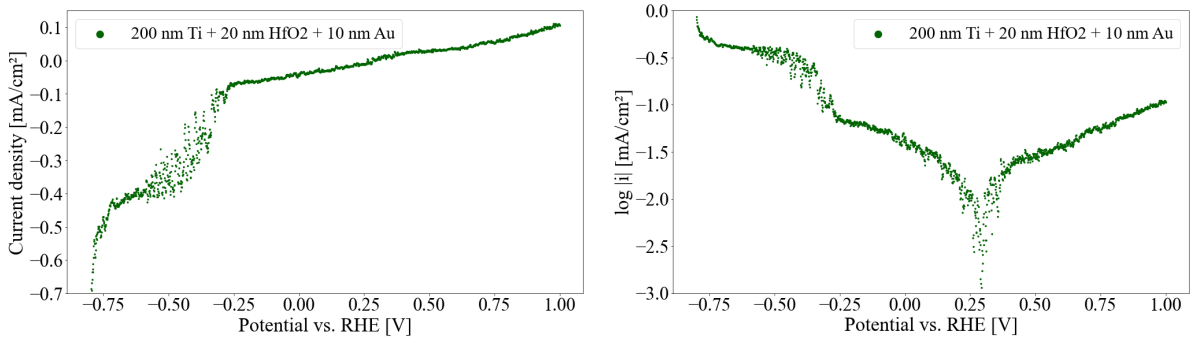

(a) (b)

Figure 4.43: Polarisation curve of coated aluminium, #44. The test was performed in 0.1 M Na_2SO_4 electrolyte, pH 3 at 70°C. Sweep rate: 1 mV s^{-1}, sweeping from -0.8 - 1 V. Current density plotted against potential (a) and log $|i|$ against potential (b).

The polarisation curves of the samples coated with 200 nm titanium, 5 nm TiO_2 (#45, #46, and #47) or 4 nm TiO_2 (#48) are shown in Figure 4.44. The lowest current density and corrosion potential were measured on sample no. 45 (pink). The current response on the sample tested in pH 5 electrolyte (#46, blue) was more even, and did not increase rapidly at a certain potential. This may be due to lower concentration of protons in the electrolyte and thus less hydrogen evolution.

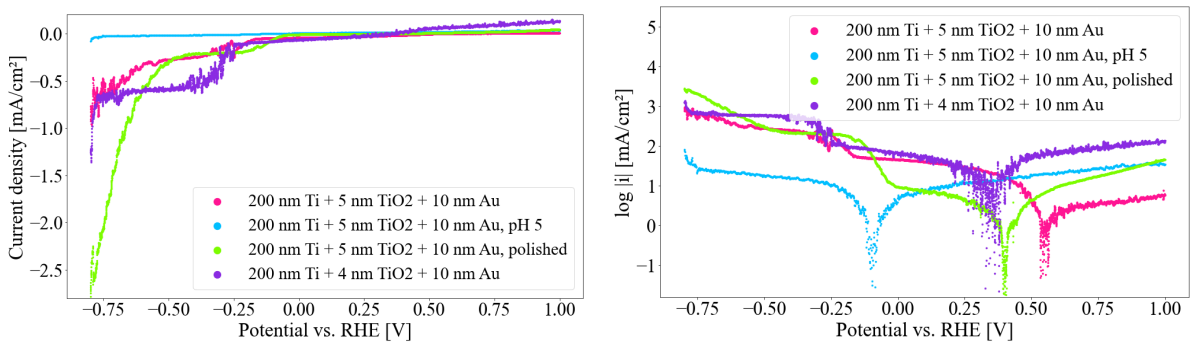

(a) (b)

Figure 4.44: Polarisation curves of coated aluminium, #45 (pink), #46 (blue), #47 (green), and #48 (purple). The tests were performed in 0.1 M Na_2SO_4 electrolyte at 70°C. One of them was tested in electrolyte adjusted 5, while the rest was tested in pH 3 electrolytes. Sweep rate: 1 mV s^{-1}, sweeping from -0.8 - 1 V. Current density plotted against potential (a) and log |i| against potential (b).

After performing linear sweep voltammetry on the samples above, a constant potential of 1 V was applied for 24 hours. The resulting current transients are shown in Figures 4.45, 4.46, and 4.47. From Figure 4.45 it can be seen that there was a large increase in current density during the first five hours of testing on sample no. 43. After testing, the coating layer was worn off underneath the gasket, while the rest of the layer adhered to the substrate. The electrolyte may have reached the sample underneath the gasket and resulted in a local environment where crevice corrosion occurred. As more crevices were formed, the higher the corrosion current.

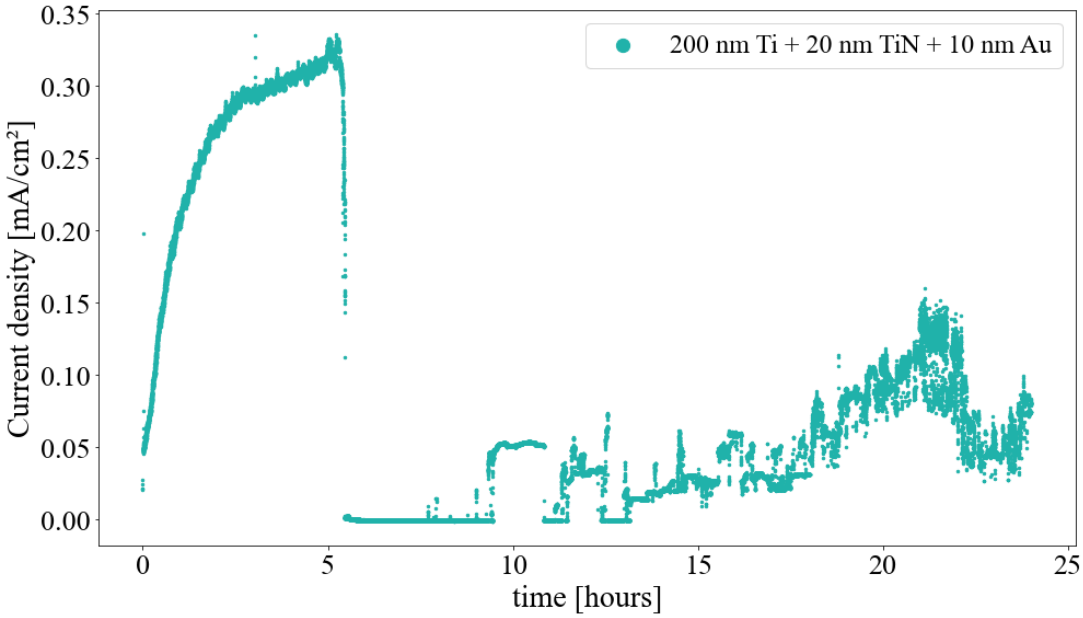

Figure 4.45: Chronoamperometric scan on coated aluminium, #43, in 0.1 M Na_2SO_4, pH 3 at 70°C. The potential was kept at 1 V for 24 hours.

The current density on sample no. 44 increased linearly with time as can be seen in Figure 4.46. A small hole in the coating was observed after a few hours of testing. This hole expanded over time, and thus led to an increased area where corrosion processes could take place.

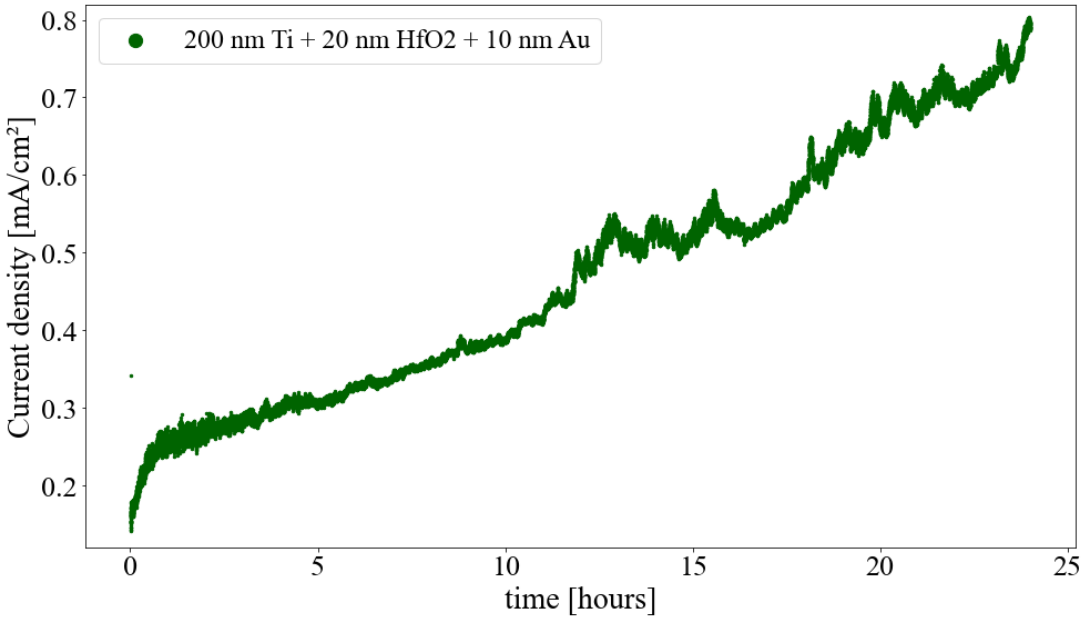

Figure 4.46: Chronoamperometric scan on coated aluminium, #44, in 0.1 M Na_2SO_4, pH 3 at 70°C. The potential was kept at 1 V for 24 hours.

There was a significant difference in measured current densities on the samples coated with 5 nm TiO_2 underneath the gold layer (#45, #46, and #47) compared to the one with 4 nm TiO_2 (#48). The coating on sample no. 48 fell off during testing. The coatings on samples no. 45, 46, and 47 did not fail, but they were worn off in the O-ring area.

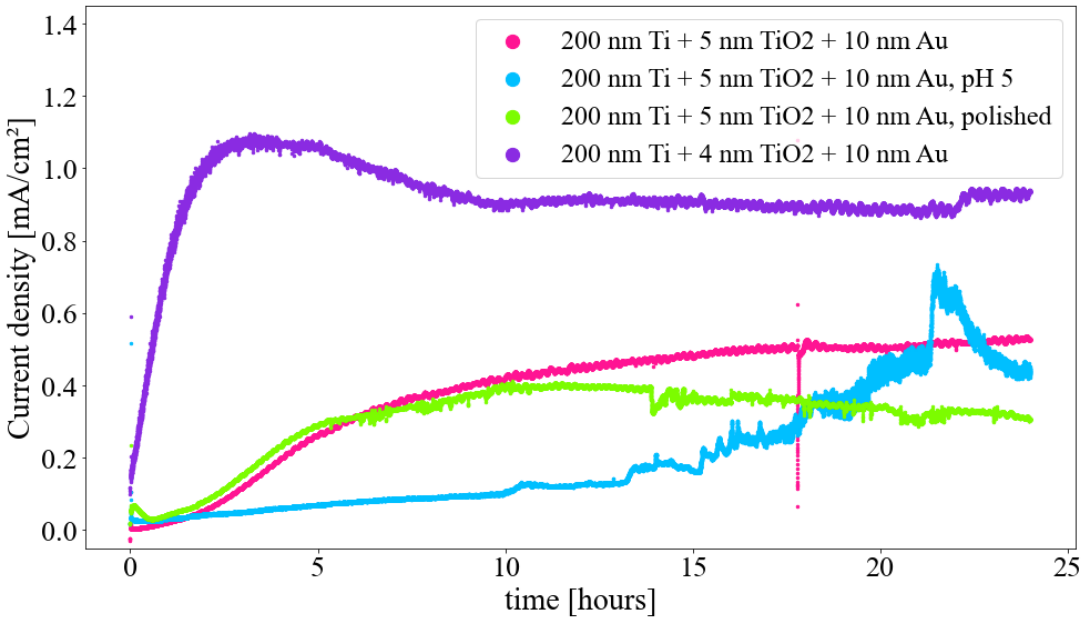

Figure 4.47: Chronoamperometric scans on coated aluminium, #45 (pink), #46 (blue), #47 (green), and #48 (purple), in 0.1 M Na_2SO_4, pH 3 at 70°C. The potential was kept at 1 V for 24 hours.

Interfacial Contact Resistance

Measured interfacial contact resistances before and after corrosion measurements were performed are given in Table 4.14. The sample no. 48 obtained the lowest contact resistance. However, this coating was not able to withstand the conditions and fell off during electrochemical measurements. No clear trend in increasing/decreasing ICR after electrochemical experiments was observed among the samples. Partial coating failure can have caused uncertainty in the measurements.

Table 4.14: Interfacial contact resistance of coated aluminium samples at a compaction pressure of 140 N cm^{-2}, before and after corrosion measurements were performed. Coating materials and thickness are specified in the table.

Sample no.	**Coating/characterisation**	**ICR at 140 N cm^{-2} [mΩ cm^2]**
43	200 nm Ti + 20 nm TiN + 10 nm Au	34.9±6.9
	After LSV & CA, 24 h	50.8±10.1
44	200 nm Ti + 20 nm HfO_2 + 10 nm Au	68.5±13.6
	After LSV & CA, 24 h	60.3±12.0
45	200 nm Ti + 5 nm TiO_2 + 10 nm Au	23.4±4.7
	After LSV & CA, 24 h	26.0±5.2
46	200 nm Ti + 5 nm TiO_2 + 10 nm Au	27.0±5.4
	After LSV & CA (pH 5), 24 h	23.4±4.7
47	200 nm Ti + 5 nm TiO_2 + 10 Au, polished	25.6±5.1
	After LSV & CA, 24 h	23.2±4.6
48	200 nm Ti + 4 nm TiO_2 + 10 nm Au	21.3±4.2
	After LSV & CA, 24 h	49.8±9.9

Surface Characterisation after Corrosion Measurements

EDS analysis suggested surface compositions according to Table 4.15 after corrosion measurements were performed. For all samples, the amount of gold before (Table 4.13) and after corrosion measurements were almost the same. This indicates little wear of coating in the detected area.

Table 4.15: EDS results of coated aluminium samples after corrosion measurements were completed.

Sample no.	**Coating**	**Al**	**Ti**	**Au**	**O**	**N**	**Hf**	**C**	**S**
43	200 nm Ti + 20 nm TiN + 10 nm Au	64.7%	16.1%	4.2%	5.0%	0.6%	-	9.3%	-
44	200 nm Ti + 20 nm HfO_2 + 10 nm Au	49.0%	15.6%	4.6%	14.4%	-	6.1%	8.2%	-
45	200 nm Ti + 5 nm TiO_2 + 10 nm Au	60.3%	19.0%	5.0%	12.1%	-	-	-	3.3%

The sample surfaces were pictured after corrosion measurements were completed and are shown in Figure 4.48. On sample no. 44 there were some flakes/sheets on the surface. On samples no. 45 and 47, some pits were observed. Some scratches were present on sample no. 43. Sample no. 47 was similar as it was before corrosion measurements.

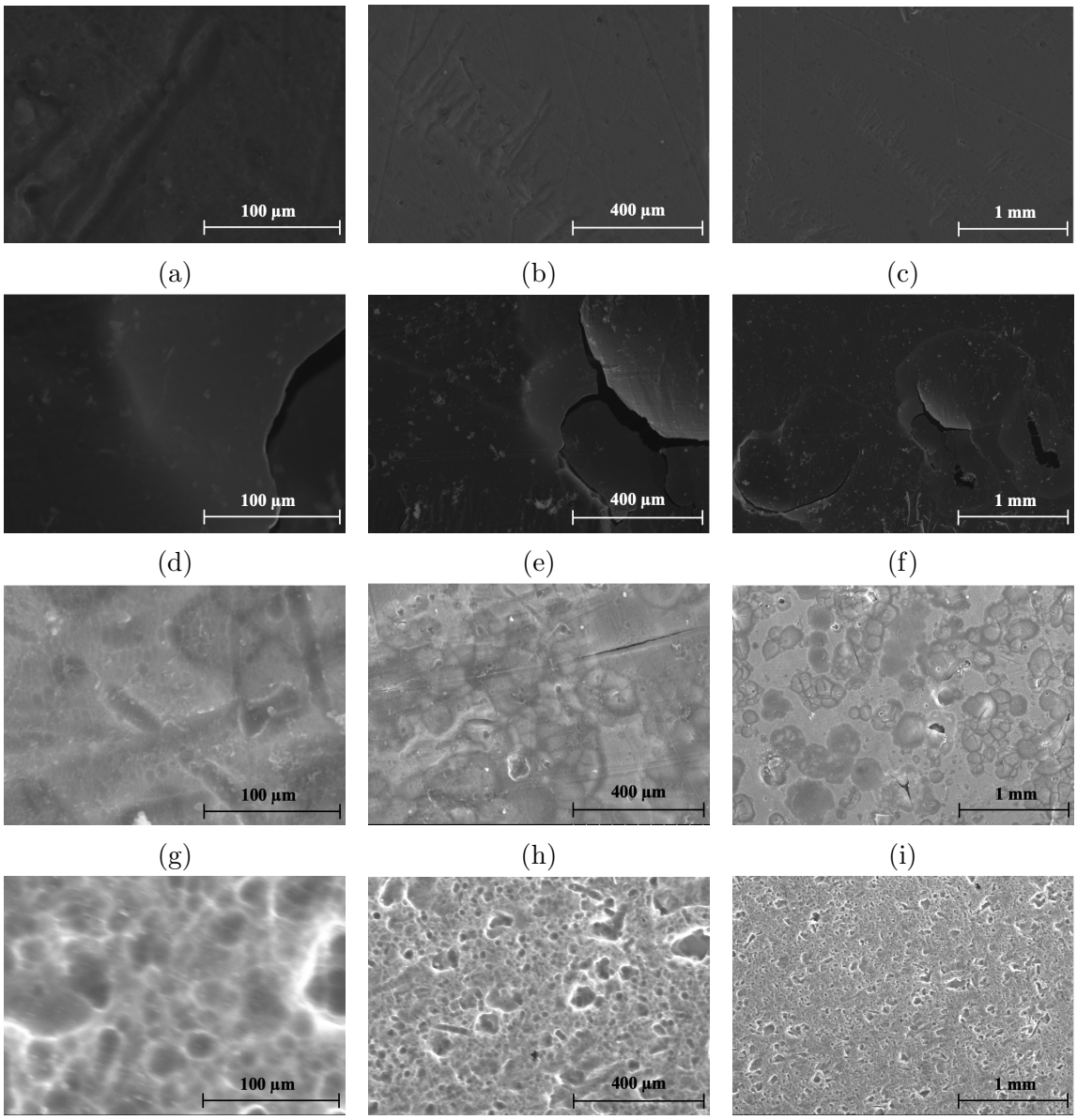

Figure 4.48: SEM images of aluminium samples coated with 200 nm titanium, (a - c): 20 nm TiN (#43), (d - f): 20 nm HfO_2 (#44), (g - i): 5 nm TiO_2 (#45), (j - l): 5 nm TiO_2 (#47) and 10 nm gold after electrochemical measurements. Notice the scale difference.

Chapter 5

Discussion

Various individual coating layers and multilayer coatings have been investigated and tested to optimise a coating solution that protects aluminium substrates from corrosion in a simulated PEMFC environment. Different parameters have proven to affect the overall performance of the coating. These, as well as the coating performance and test conditions are discussed in the following sections.

5.1 Evaluation of Pre-Treatment Procedure

By studying the different sample surfaces using SEM, it is clear that the final surface morphology is determined mainly by the pre-treatment procedure (Fig. 4.5 - 4.8). Various coating techniques have been performed, but none of the coating layers appears to affect the morphology of the surface. The pre-treatment procedure has therefore proved to be of particular importance.

5.1.1 Variable Cleaning Intervals

Increased immersion time in the alkaline cleaning solution led to an increased amount of pits on the surface due to uneven dissolution of the oxide layer. SEM pictures of the zincated samples immersed in the alkaline cleaner for variable intervals prior to zincating, shown in Figure 4.5 - 4.8, revealed that the shortest immersion time led to the most even surface. When immersing aluminium in alkaline solutions, the oxide dissolves due to attacks by hydroxides. In areas where the oxide has been dissolved, bare aluminium is exposed to the alkaline solution. Hydroxides are then able to attack aluminium resulting in aluminium oxidation. As described in Subsection 2.3.2, these two actions happen simultaneously. Thus, oxide dissolution occurs in some areas while aluminium dissolves in others. Larger amounts of aluminium dissolve in areas where the oxide was removed rapidly, resulting in an uneven surface with many pits.

By reducing the immersion time, the dissolution of bare aluminium can be reduced. However, this can also lead to an incomplete oxide removal and thus high interfacial contact resistance. According to the measured ICR, a shorter immersion time did not influence the contact resistance. It was therefore concluded that a shorter immersion time would result in less attacks of bare aluminium and the same amount of oxide dissolved as a longer immersion time.

5.1.2 Variable pH of Alkaline Cleaner

Reducing the pH of the alkaline cleaning solution did not lead to a more uniform oxide dissolution. The sample surfaces obtained almost the same amount of pits independently of solution pH. Pits were present on all the surfaces pictured in Figure 4.4, and the number of pits did not decrease although the pH of the cleaning solution was reduced. Reducing the pH leads to a lower concentration of hydroxide ions. Thus, reducing the pH leads to fewer hydroxides available to attack the oxide. However, according to the results, it seems like the amount was high enough to attack both the oxide and the bare aluminium spots.

5.1.3 Polishing

Two samples (sample no. 36 and 47) were polished prior to coating application. Polishing was thought to reduce the probability of obtaining coating-defects/incomplete coating coverage. Although the SEM pictures (Fig. 4.1d - 4.1f) showed other surface characteristics than unpolished samples, the polished samples did not show enhanced corrosion protection of significant level in the simulated PEM fuel cell environment. Assuring a flat and even surface without asperities is essential when coating-defects are undesirable. Complete coating coverage is challenging to achieve if the asperity is higher than the coating thickness. This results in non-covered spots in the coating, where water/electrolyte can reach the underlying substrate and initiate coating failure.

5.2 Coating Performance

5.2.1 Contact Resistance of Coated Substrates

The majority of the samples in this work showed an increase in contact resistance after performing electrochemical measurements. Oxide formation probably took place on the sample surfaces during electrochemical testing, despite the high currents. Since the electrical resistivity of oxides is high (Table 2.1), oxide formation on the sample surfaces results in increased ICR. However, aluminium oxide is not stable in the testing environment and should, therefore, according to theory (Fig. 2.7), not be present on the surfaces post electrochemical tests. Another possible explanation for the increase in measured ICR

is coating failure. When measuring the ICR on samples where the coating is partly removed, the number of contact points between the GDL and the sample is greatly reduced, leading to a decrease in contact area between the sample and the GDL. It is a well-known phenomenon that the ICR decreases as the applied compaction pressure increases due to the increased contact area between the sample and the GDL [72]. Thus, when this area is reduced due to partial coating removal, the increase in ICR post corrosion tests may be caused by this phenomenon. Since the GDL is a cloth/paper, it may deform when exposed to an applied compaction pressure. Depending on how much of the coating layer that is worn off, the reduction in contact area may not be significant to affect the ICR measurements.

All the aluminium samples with Ni(P)Cr coatings investigated by Marzo et al. [40] showed an increase in ICR after potentiodynamic polarisation tests. For metallic bipolar plates, the ICR is determined by both surface composition, and its morphology [73]. According to Han et al. [72] the roughness of the bipolar plate can be adjusted to the surface roughness of the gas diffusion layer and thereby significantly reduce the ICR. A low ICR was expected if morphology was the determining factor for the Ni-P-Cr coated sample, which obtained the lowest roughness. However, this sample showed the most significant increase in ICR and the highest corrosion resistance thanks to oxide formation. Thus, the morphological factor did not compensate for the high resistive nature of the surface oxide [40].

The interfacial contact resistance increased considerably when an oxide layer was applied but decreased when a second layer of conductive material was applied on top of the oxide. This was observed on the samples coated with either titanium oxide or aluminium oxide before titanium or gold was deposited by e-beam evaporation. Possible explanations for these measurements are surface structure and roughness. Titanium/gold can be deposited in the bottom of the pits on a surface containing pits, leading to shorter pathways for the current and thus reducing the resistance. Additionally, a second layer can reduce surface roughness. Shorter pathways for the current and reduced roughness results in lower contact resistance. Finally, improved contact resistance when a new coating layer is added can also indicate that good enough adhesion not to impact the conductivity between coating layers is achieved.

In contrast to the samples obtaining higher ICR after electrochemical tests, the samples having oxides as the main coating layer showed a decrease in ICR after corrosion tests. The decreasing ICR-values post electrochemical tests indicate oxide dissolution during corrosion tests. Aluminium oxide is not stable in pH 3 solutions (Figure 2.7). Titanium oxide, however, is supposed to be stable in pH 3 environments, even when potentials between 0 and 1 V are applied [11]. According to the reduction in contact resistance,

parts of the layer have been removed, and there is no clear reason why.

5.2.2 Corrosion Behaviour of Coated Substrates

In this study, the corrosion potential of aluminium substrates shifted towards more positive values when coatings were applied. The measured corrosion potential of uncoated aluminium in pH 3 electrolyte was -750 mV (Figure 4.2b (pink)), while the lowest corrosion potential of coated aluminium was around -375 mV (Fig. 4.28b (blue) and 4.34b). Two of the coated samples, no. 34 and 45, obtained corrosion potentials above 0.5 V (Figure 4.27b and 4.44b (pink)), which were the samples with the highest corrosion potentials during this work. This may be due to complete coating coverage on sample no. 45. Sample no. 34 showed very good corrosion resistance in the simulated PEMFC environment. This may be explained by proper adhesion achieved thanks to the activation of the substrate during magnetron sputtering. Another factor that may have enhanced sample no. 34's corrosion resistance can be the fact that Al and TiN have more similar coefficients of linear expansion compared to Al and Ti (Table 2.1). Marzo et al. [40] also found that coating application on aluminium led to an increase in corrosion potential, increasing from -741.2 $mV_{Ag/AgCl}$ for uncoated aluminium to values between -344 and -207 $mV_{Ag/AgCl}$ for coated aluminium substrates.

The main cathodic reaction in acidic deaerated solutions is the hydrogen evolution reaction. However, in pH 3 solutions, where oxygen is present, HER and ORR are of the same magnitude [63]. The exchange current density of HER is strongly affected by the condition of the surface i.e. the quality of the coating [40]. The electrolyte solution, temperature and concentration also affect the exchange current density of HER [63]. Polarisation curves were, during this work, recorded in acidic deaerated solutions, and HER was therefore expected to be the main cathodic reaction. The variety of the exchange current density of HER and coating materials on aluminium makes it hard to determine a clear trend in measured corrosion potentials. These factors also make it complicated to compare with results reported in the literature.

Although the coated samples obtained higher corrosion potentials than uncoated aluminium, they showed similar current responses as uncoated aluminium when exposed to a constant potential of 1 V for 1 hour or 24 hours. The exceptions are the samples coated with TiN and Ti + TiO_2, sample no. 34 and 38, respectively. Sample no. 38 was only tested for 1 hour, and the current density increased linearly with time. The maximum current density was reached by the end of the scan ($\sim$74 µA cm^{-2}). At this point, the coating was still intact. However, as the current continued increasing throughout the scan, it would probably continue to increase if the scan had been running for longer than 1 hour. The current response of sample no. 34 showed increasing values during the first 3

hours before it stabilised at low values (Figure 4.36). The higher corrosion current at the beginning of the scan indicates corrosion processes occurring on the sample. According to the EDS analysis performed post corrosion tests (Table 4.11), oxygen was present, and there was almost no nitrogen left on the surface. Thus, it is likely that titanium has oxidised from Ti^{3+} in TiN to Ti^{4+} in TiO_2. The increase in ICR (4.10) also underpins this. The samples coated with gold on top of the TiN-layer, sample no. 35 and 36, were expected to show improved performance in terms of both contact resistance and corrosion resistance. However, these coatings failed during potential hold for 24 hours.

Coated stainless steel and coated aluminium substrates performed differently in the simulated PEM fuel cell environment. The current responses of coated stainless steel substrates were much lower than those of aluminium substrates tested during this work. Additionally, the shape of the current transients differed. As can be seen from Fig. 4.13 and 4.17b, the corrosion currents of coated stainless steel were high during the first minutes of the scans before they decreased considerably and stabilised. This is classic characteristics of uncoated and coated stainless steel during potentiostatic tests in simulated PEM fuel cell environments [74, 75]. Coated aluminium substrates on the other hand, did not show any specific characteristics during potential hold. However, some of the samples showed current transients with a small initial drop before it increased relatively rapidly and after that stabilised (Fig. 4.9, 4.12 (green and blue) and 4.17a). The initial drop in current density observed on stainless steel is caused by the formation of a passive film on the bare/coated surface that is stable in the PEMFC environment [76, 77]. There is no sign of local corrosion as the current does not change significantly when first stabilised. It seems like a passive film starts to form on the coated aluminium samples as well, and therefore an initial drop in current is observed. However, after some minutes, the rapid increase in current density indicates aluminium oxidation, most likely due to insufficient surface coverage or coating-defects.

The behaviour of titanium oxide and aluminium oxide in the simulated PEMFC environment differs. Al_2O_3-coated samples showed similar performance as uncoated aluminium during 1 hour of potential hold (Figure 4.3 (pink) and 4.25 (pink and blue)). When applying Al_2O_3 on top of TiO_2, titanium oxide is left on the surface, although aluminium oxide dissolves, providing some corrosion protection. This was shown in terms of lower current response (Figure 4.25 (green)). Among the TiO_2-coated samples, a thicker titanium oxide layer resulted in lower corrosion currents indicating better coverage of substrate. This result may indicate that a certain thickness of the ALD-layers is necessary in order to cover an uneven surface completely.

5.3 Coating Failure

Most of the coatings failed during electrochemical experiments. This was probably in most cases due to significant corrosion and dissolution of substrate material during electrochemical testing. Some of the coatings also experienced delamination as a result of bad adhesion. Coating failure was either initiated directly on the area exposed to the electrolyte or underneath the O-ring/gasket of the sample holder.

Coating failure was initiated in the area exposed to the electrolyte, especially on samples with titanium deposited by e-beam evaporation as the outer layer. This outcome was observed independently of the adhesion layer, zinc, Al_2O_3 or TiO_2, applied prior to titanium deposition. It was also observed when titanium was applied directly on aluminium. This may be due to poor quality of the e-beam layer. Havigh et al. [39] discovered the same when they applied a multilayer coating on aluminium (AA1050) consisting of titanium and carbon deposited by a physical vapour disposition technique. These findings are probably due to incomplete surface coverage and poor adhesion between the substrate and the coating layer. If pits were present when titanium was applied and the pits/trenches were deeper than the applied titanium thickness, titanium was most likely deposited only in the bottom of the trench, as illustrated in Figure 5.1. Bare aluminium is then directly exposed to the electrolyte, leading to oxidation of aluminium. Thus, the corrosion products could push the titanium coating away from the surface, exposing larger areas of aluminium to the electrolyte.

Figure 5.1: Simple sketch of the cross-section of an aluminium substrate containing pits, coated with titanium. Only partial coverage of titanium in the pits.

Combining e-beam evaporation and atomic layer deposition to deposit multilayer coatings was thought to result in a denser coating without pathways for electrolyte ions to reach the underlying substrate. ALD is known for its ability to coat irregularly shaped geometries, as described in Subsection 2.3.1. Suppose the film deposited by e-beam evaporation is incomplete. In that case, the titanium oxide layer deposited by ALD is thought to coat these incomplete spots, thus resulting in complete coverage of the aluminium substrate as shown in Figure 5.2. Experiments showed that the layer deposited by ALD had to be of a certain thickness to show an effect. Thickness ranging from 1 nm to 5 nm were

tested. However, the coatings failed unless the thickness was 5 nm, corresponding to 100 molecular layers of titanium oxide.

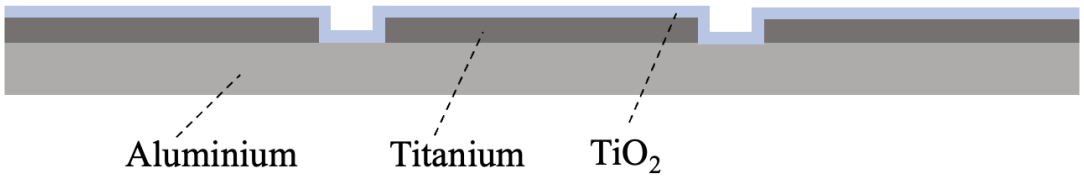

Figure 5.2: Simple sketch of the cross-section of aluminium coated with titanium and titanium oxide.

Some of the samples experienced that the coating was worn off in the area where the O-ring had been in contact with the sample surface. This may be due to the compaction pressure the coating is subjected to when the lid, with the O-ring mounted in, is tightened onto the sample. The coating layer is impaired during this action. When exposed to acidic aqueous conditions, the layer is already weakened and extra vulnerable to small ions, such as H^+ that can penetrate the coating. To minimise this effect, a new lid was made. The new lid was made to function with a gasket instead of an O-ring. This was thought to distribute the compaction pressure more evenly when tightening the lid and avoiding the electrolyte reaching the sample's back. However, the new lid did not seem to overcome this challenge as the coating was worn off in the contact area between the gasket and the sample. Although the coating is subjected to a more evenly distributed compaction pressure by using a gasket instead of an O-ring, the coating is weakened during this action. Electrolyte can then migrate under the sample holder's lid and reach the weakened coating spots. This is sketched in Figure 5.3. Thus, crevice corrosion can occur, as described in Subsection 2.4.2. Eventually, as corrosion products are formed, a local environment underneath the gasket arises, which can be even harsher than the simulated PEMFC environment. According to the holes in the substrates, severe corrosion processes occurred under the gasket.

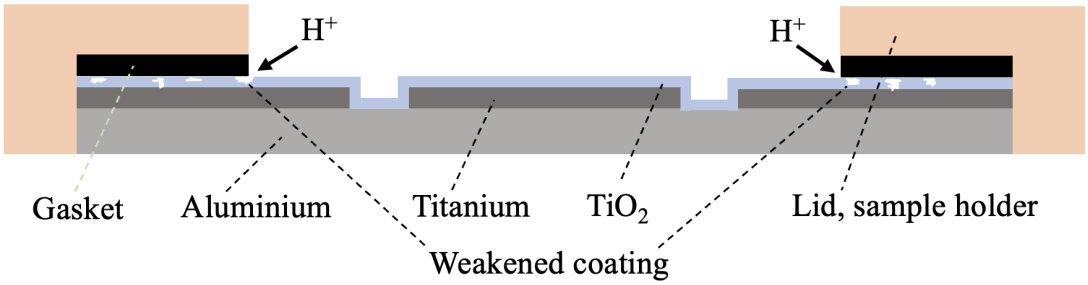

Figure 5.3: Simple sketch of the cross-section of aluminium coated with titanium and titanium oxide. Weak spots in coating, due to compaction pressure from the gasket and lid, included.

5.4 Prevention of Coating Failure

Two main causes for the coating failures observed during this work have been suggested and discussed. These two include weakened spots in the coating due to compaction pressure from the sample holder and coating-defects/incomplete coverage of substrate.

In order to determine whether or not the multilayer coating actually protects the aluminium substrate from corrosion, sources of error such as sample holder issues must be avoided. Since it did not yield improved results by replacing the O-ring with a gasket on the sample holder, another testing setup may be used. An alternative setup should focus on only exposing the coated surface to the electrolyte, not to any external forces. One possibility is to apply a non-conductive material, e.g. nail polish or beeswax, on the back and edges of the sample, thus ensuring testing on coated areas only.

When desired to minimise coating-defects, the pre-treatment procedure is a key factor. By removing the naturally formed oxide layer on aluminium and replacing it with a continuous and solid layer, stronger and more stable bonds are facilitated [78]. The surface should be as homogeneous and even as possible to avoid pits/asperities since such features make it hard to achieve complete coating coverage. Proper, strong bonds between the substrate and the coating material are also crucial [79]. Surface roughness leads to a larger surface area to which the coating material can adhere. The bonding strength between the substrate and coating material depends on the coating technique. Among the coating techniques applied during this work, ALD and magnetron sputtering are the two techniques in which the substrate is activated during deposition facilitating stronger bonds (Subsection 2.3.1). During e-beam evaporation, on the other hand, the substrate is not activated, and the bond strength is determined by the lattice match between the substrate and the deposition material. Various coating thickness were applied. Thicker coatings were expected to smooth out irregularities resulting from the pre-treatment procedure and thus perform better in terms of corrosion resistance. However, thick coatings deposited by e-beam evaporation contained visible defects. It is hard to obtain strong and stable bonds to a thick layer deposited by e-beam evaporation. Since it is a physical technique, depositing thick layers might lead to uneven nucleation and build-up of atoms. The thicker the coating, the longer distance from the substrate to the coating material, resulting in weak bonds to the outer part of the coating layer.

An additional factor that may have caused coating failure is too harsh testing conditions. Two samples were exposed to somewhat milder conditions in the form of increased electrolyte pH (pH 5). This pH-increase did not seem to have a large impact on the coated sample, as coating failure underneath the gasket occurred anyway. However, for uncoated aluminium, increased electrolyte pH led to lower corrosion currents. During testing in a

three-electrode cell, local pH variations under the gasket can be responsible for coating failure on the coated sample. As described in Subsection 2.5.2, the bipolar plate is immersed in an acidic and warm electrolyte and exposed to high potentials during ex-situ corrosion tests. Ex-situ testing potentials have shown to be higher than the potentials experienced by the BPP in an operating PEM fuel cell. In-situ, the BPP only experiences contact with acidic droplets, not full immersion in acidic media. Additionally, the bipolar plate is not exposed to compaction pressure from a gasket/O-ring as it was during ex-situ tests. Therefore, more realistic testing conditions can be a way to avoid coating failure and thereby be able to study a more realistic behaviour of the coated substrates.

Chapter 6

Conclusion

Various multilayer coatings have been applied on aluminium substrates. The aim was to achieve a coating that was and remained highly conductive while being able to resist corrosion attacks in the aggressive PEMFC environment. Zincated aluminium coated with 200 nm titanium (#9, #10, and #11), aluminium coated with 300 nm (#13) and 1.5 µm titanium (#18) respectively, as well as the Al-samples coated with TiN + Au (#35 and #36) and Ti + TiO_2 (#41 and #42) were all able to meet the area specific resistance target of below 10 mΩ cm^2, outlined by the DOE prior to corrosion tests. Therefore, it can be concluded that coated aluminium substrates are suitable as BPPs concerning conductivity. However, after performing corrosion tests, none of the samples obtained ICR below 10 mΩ cm^2.

Aluminium coated with titanium nitride was the only sample obtaining a corrosion current close to the target of below 1 µA cm^{-2}. However, during the first three hours of the scan, the current peaked at 33 µA cm^{-2}, which should be avoided. In addition, this sample did not meet the area specific resistance target. Therefore, titanium nitride coatings applied by magnetron sputtering should be further investigated and modified to avoid a sudden increase in current density during electrochemical tests and minimise the contact resistance.

The other samples were not close to the corrosion resistance target and obtained high currents due to incomplete coating coverage/coating defects and thus corrosion of the underlying substrate. This was observed in form of coating failure during polarisation. The acidity of the electrolyte combined with the high potentials during testing exposed the samples to very harsh conditions. As soon as the coating contained an imperfection/weakened spot, the electrolyte reached the substrate and resulted in aluminium dissolution. Electron beam evaporation resulted in incomplete layers that did not create strong enough bonds to the substrate. This was probably due to a lack of substrate activation during deposition. Applying dense ALD layers on top of e-beam layers improved the corrosion resistance to some extent, as it may have sealed some of the weak spots in the e-beam

layer. Coating layers deposited by magnetron sputtering performed better than e-beam layers, probably due to substrate activation during magnetron sputtering and thus improved adhesion. However, the corrosion currents were high, which could have been caused by weakened coating spots underneath the O-ring/gasket or adhesion loss between the substrate and coating layer as the electrolyte reached the underlying substrate through imperfections in the coating layer. Therefore, it can be concluded that both poor coating quality and testing setup may have caused coating failure.

Chapter 7

Further work

Since the main challenge is obtaining a coating that does not fail when exposed to conditions similar to those inside a PEMFC, the main focus for further work should be achieving a dense coating without defects. First, a pre-treatment procedure that provides an adhesive surface without deep pits/trenches and asperities should be developed. Magnetron sputtering has shown to yield layers of higher quality compared to e-beam evaporation, and titanium-based coatings deposited by magnetron sputtering should be further investigated. Titanium nitride deposited directly on aluminium showed very good corrosion resistance, although the contact resistance was too high. A gold top layer increased the conductivity considerably but the titanium and gold coatings failed during experiments. Potentially, the gold top layer could avoid oxide formation on the surface to some extent and thus reduced contact resistance over time. Therefore, a thin conductive layer on top of titanium nitride should be further investigated.

There is some uncertainty about whether or not coating failures occur due to weak coating layers or due to the formation of a local environment under the lid of the sample holder. The local environment in addition to weakened coating spots in the contact area between the coating and the gasket that were formed when mounting the lid, can act as starting points for coating failure. Therefore, a new testing setup should be developed and tested. Studying the cross-section of the coating using SEM to see the coverage of each coating layer can be useful. It might also make it possible to study the porosity of the various layers. ICR measurements will probably also be more reliable if coating failure is avoided as it will result in less uncertainty regarding decreased contact points and increased roughness due to partial coating removal. Roughness measurements can also be performed to check if there is a relation between ICR and roughness.

Another possibility is to look into other aluminium alloys. This work has only investigated AA1080 substrates. There might be some alloys more suitable for coating application as they facilitate better adhesion to coating materials. Or maybe another alloy will show enhanced corrosion resistance in the PEMFC environment thanks to alloying elements

increasing the corrosion resistance.

During ex-situ electrochemical measurements, the coated aluminium substrates were fully immersed in pH 3 electrolytes, and high potentials, maybe even higher than actually experienced by the BPP in-situ, were applied. For aluminium bipolar plates to become a reality, a deeper understanding of the environment they will be exposed to, and their behaviour in this environment is required. In-situ tests are necessary to achieve such an understanding. Such insight can also make it easier to mimic realistic conditions for ex-situ testing. For in-situ tests, flow field patterns must be etched or stamped. When implementing flow field patterns in the substrates, this can provide information about degrading in the channels compared to the areas in contact with the GDL. Although the parallel-serpentine flow field geometry is very reliable due to its suitable pressure drop, it does not mean this is the preferred choice for aluminium BPPs. In-situ tests of aluminium BPPs with different flow field patterns and various degrees of humidity can reveal under which conditions coated aluminium is suitable for BPP applications.

Bibliography

[1] "*Fuel Cell and Hydrogen Energy Association, FCHEA: Transportation.*" `https://www.fchea.org/transportation`, accessed: 23.05.2022.

[2] T. Kadyk, C. Winnefeld, R. Hanke-Rauschenbach, and U. Krewer, "Analysis and Design of Fuel Cell Systems for Aviation," *Energies*, vol. 11, p. 375, 2 2018.

[3] L. Peng, P. Yi, and X. Lai, "Design and manufacturing of stainless steel bipolar plates for proton exchange membrane fuel cells," *International Journal of Hydrogen Energy*, vol. 39, 12 2014.

[4] Y. Song, C. Zhang, C.-Y. Ling, M. Han, R.-Y. Yong, D. Sun, and J. Chen, "Review on current research of materials, fabrication and application for bipolar plate in proton exchange membrane fuel cell," *International Journal of Hydrogen Energy*, vol. 45, pp. 29832–29847, 11 2020.

[5] Y. Leng, D. Yang, P. Ming, and C. Zhang, "A comparative study of corrosion resistance evaluation of bipolar plate materials for proton exchange membrane fuel cell," *eTransportation*, vol. 10, p. 100139, 11 2021.

[6] H. Tsuchiya, "Mass production cost of PEM fuel cell by learning curve," *International Journal of Hydrogen Energy*, vol. 29, pp. 985–990, 8 2004.

[7] "*U.S Department of Energy: DOE Technical Targets for Polymer Electrolyte Membrane Fuel Cell Components.*" `https://www.energy.gov/eere/fuelcells/doe-technical-targets-polymer-electrolyte-membrane-fuel-cell-components`, accessed: 11.02.2022.

[8] US Drive Partnership, "Fuel Cell Technical Team Roadmap," 2017.

[9] M. A. Mustaparta, "Multilayer Coated Aluminium Bipolar Plates for Light-weight Fuel Cells," 2021.

[10] M. Muñoz-Portero, J. García-Antón, J. Guiñón, and R. Leiva-García, "Pourbaix diagrams for titanium in concentrated aqueous lithium bromide solutions at 25°C," *Corrosion Science*, vol. 53, pp. 1440–1450, 4 2011.

[11] S. Prasad, M. Ehrensberger, M. P. Gibson, H. Kim, and E. A. Monaco, "Biomaterial properties of titanium in dentistry," *Journal of Oral Biosciences*, vol. 57, pp. 192–199, 11 2015.

[12] A. L. Dicks and D. A. J. Rand, *Fuel Cell systems explained, Chapter 3.* Hoboken: Wiley, third ed., 2000.

[13] U. Lucia, "Overview on fuel cells," *Renewable and Sustainable Energy Reviews*, vol. 30, pp. 164–169, 2 2014.

[14] X. LI and I. SABIR, "Review of bipolar plates in PEM fuel cells: Flow-field designs," *International Journal of Hydrogen Energy*, vol. 30, 3 2005.

[15] A. Z. Weber, S. Balasubramanian, and P. K. Das, "Proton Exchange Membrane Fuel Cells," pp. 65–144, 2012.

[16] "*Fuel Cell Store: Membrane Electrode Assemblies (MEA).*" `https://www.fuelcellstore.com/fuel-cell-components/membrane-electrode-assembly`, accessed: 10.02.2022.

[17] A. L. Dicks and D. A. J. Rand, *Fuel Cell Systems Explained, Chapter 4.* Hoboken: Wiley, third ed., 2000.

[18] H. Wang and J. A. Turner, "Reviewing Metallic PEMFC Bipolar Plates," *Fuel Cells*, vol. 10, 4 2010.

[19] U. Chakraborty, "Fuel crossover and internal current in proton exchange membrane fuel cell modeling," *Applied Energy*, vol. 163, 2 2016.

[20] S. Peighambardoust, S. Rowshanzamir, and M. Amjadi, "Review of the proton exchange membranes for fuel cell applications," *International Journal of Hydrogen Energy*, vol. 35, 9 2010.

[21] S. Karimi, N. Fraser, B. Roberts, and F. R. Foulkes, "A Review of Metallic Bipolar Plates for Proton Exchange Membrane Fuel Cells: Materials and Fabrication Methods," *Advances in Materials Science and Engineering*, vol. 2012, 2012.

[22] "*Fuel Cell Store: End Plates.*" `https://www.fuelcellstore.com/fuel-cell-components/plates/end-plates`, accessed: 17.02.2022.

[23] P. T. Nguyen, T. Berning, and N. Djilali, "Computational model of a PEM fuel cell with serpentine gas flow channels," *Journal of Power Sources*, vol. 130, 5 2004.

[24] K. McCay, *Tin and Tin Alloys for Low Cost Bipolar Plates in PEM Fuel Cells.* PhD thesis, Department of Materials Science and Engineering, NTNU, Trondheim, 2020.

[25] J. André, L. Antoni, and J.-P. Petit, "Corrosion resistance of stainless steel bipolar plates in a PEFC environment: A comprehensive study," *International Journal of Hydrogen Energy*, vol. 35, 4 2010.

[26] H. Tawfik, Y. Hung, and D. Mahajan, "Metal bipolar plates for PEM fuel cell—A review," *Journal of Power Sources*, vol. 163, 1 2007.

[27] N. F. Asri, T. Husaini, A. B. Sulong, E. H. Majlan, and W. R. W. Daud, "Coating of stainless steel and titanium bipolar plates for anticorrosion in PEMFC: A review," *International Journal of Hydrogen Energy*, vol. 42, 4 2017.

[28] O. Alo, I. Otunniyi, H. Pienaar, and S. Iyuke, "Materials for Bipolar Plates in Polymer Electrolyte Membrane Fuel Cell: Performance Criteria and Current Benchmarks," *Procedia Manufacturing*, vol. 7, 2017.

[29] F. G. Boyacı San and O. Okur, "The effect of compression molding parameters on the electrical and physical properties of polymer composite bipolar plates," *International Journal of Hydrogen Energy*, vol. 42, 9 2017.

[30] T. Bohackova, J. Ludvik, and M. Kouril, "Metallic Material Selection and Prospective Surface Treatments for Proton Exchange Membrane Fuel Cell Bipolar Plates—A Review," *Materials*, vol. 14, 5 2021.

[31] A. Hermann, T. Chaudhuri, and P. Spagnol, "Bipolar plates for PEM fuel cells: A review," *International Journal of Hydrogen Energy*, vol. 30, 9 2005.

[32] R. A. Antunes, M. C. L. Oliveira, G. Ett, and V. Ett, "Corrosion of metal bipolar plates for PEM fuel cells: A review," *International Journal of Hydrogen Energy*, vol. 35, 4 2010.

[33] A. Samu, K. Pertti, I. Jari, and K. Pasi, "Bipolar plate, method for producing bipolar plate and PEM fuel cell.," *United State Patent Appl 20090142645*, 2009.

[34] R. B. Ross, *Metallic materials specification handbook*. London: Spon, fourth ed., 1992.

[35] S.-J. Lee, C.-H. Huang, and Y.-P. Chen, "Investigation of PVD coating on corrosion resistance of metallic bipolar plates in PEM fuel cell," *Journal of Materials Processing Technology*, vol. 140, pp. 688–693, 9 2003.

[36] C. Vargel, *Corrosion of Aluminium*. Elsevier, 2004.

[37] D. Landolt, *Corrosion and surface chemistry of metals, Chapter 8*. EPFL Press, first edition ed., 2007.

[38] Haynes W. M., *CRC Handbook Chemistry and Physics*. CRC Press, 2016.

[39] M. Dabiri Havigh, A. Hubin, and H. Terryn, "Assessment of Carbon-Titanium Multilayer Coatings on Aluminum as Bipolar Plates in PEM Fuel Cells," *Journal of The Electrochemical Society*, vol. 168, p. 061503, 6 2021.

[40] F. Marzo, M. Alberro, A. Manso, X. Garikano, C. Alegre, M. Montiel, A. Lozano, and F. Barreras, "Evaluation of the corrosion resistance of Ni(P)Cr coatings for bipolar plates by electrochemical impedance spectroscopy," *International Journal of Hydrogen Energy*, vol. 45, pp. 20632–20646, 8 2020.

[41] A. E. Fetohi, R. Abdel Hameed, K. El–Khatib, and E. R. Souaya, "Study of different aluminum alloy substrates coated with Ni–Co–P as metallic bipolar plates for PEM fuel cell applications," *International Journal of Hydrogen Energy*, vol. 37, 7 2012.

[42] A. G. G. Gutiérrez, M. A. Pech-Canul, and P. J. Sebastian, "Zincating Effect on Corrosion Resistance of Electroless Ni-P Coating on Aluminum Alloy 6061," *Fuel Cells*, vol. 17, pp. 770–777, 12 2017.

[43] G. Lu and G. Zangari, "Corrosion resistance of ternary NiP based alloys in sulfuric acid solutions," *Electrochimica Acta*, vol. 47, pp. 2969–2979, 7 2002.

[44] A. E. Fetohi, R. A. Hameed, and K. El-Khatib, "Development of electroless Ni–P modified aluminum substrates in a simulated fuel cell environment," *Journal of Industrial and Engineering Chemistry*, vol. 30, pp. 239–248, 10 2015.

[45] E. Khan, C. F. Oduoza, and T. Pearson, "Surface characterization of zincated aluminium and selected alloys at the early stage of the autocatalytic electroless nickel immersion process," *Journal of Applied Electrochemistry*, vol. 37, pp. 1375–1381, 10 2007.

[46] K. Seshan (Editor), *Handbook of Thin-Film Technology*. Berlin, Heidelberg: Springer Berlin Heidelberg, 2015.

[47] G. Cao and Y. Wang, *Nanostructures and Nanomaterials*. World Scientific Pubishing Co. Pte. Ltd, 2nd edition ed., 2011.

[48] "*AJA International Inc: Magnetron Sputtering*." `https://www.ajaint.com/what-is-sputtering.html`, accessed: 23.05.2022.

[49] S. Swann, "Magnetron sputtering," *Physics in Technology*, vol. 19, pp. 67–75, 3 1988.

[50] S. M. George, "Atomic Layer Deposition: An Overview," *Chemical Reviews*, vol. 110, pp. 111–131, 1 2010.

[51] S.-M. Moon and S.-I. Pyun, "The corrosion of pure aluminium during cathodic polarization in aqueous solutions," *Corrosion Science*, vol. 39, 2 1997.

[52] P. Deepa and R. Padmalatha, "Corrosion behaviour of 6063 aluminium alloy in acidic and in alkaline media," *Arabian Journal of Chemistry*, vol. 10, pp. S2234–S2244, 5 2017.

[53] I. Boukerche, S. Djerad, L. Benmansour, L. Tifouti, and K. Saleh, "Degradability of aluminum in acidic and alkaline solutions," *Corrosion Science*, vol. 78, pp. 343–352, 1 2014.

[54] S.-K. Lee, J.-H. Lee, and Y.-H. Kim, "Nucleation and Growth of Zinc Particles on an Aluminum Substrate in a Zincate Process," *Journal of Electronic Materials*, vol. 36, 10 2007.

[55] B. R. Strohmeier, W. T. Evans, and D. M. Schrall, "Preparation and surface characterization of zincated aluminium memory-disc substrates," *Journal of Materials Science*, vol. 28, pp. 1563–1572, 3 1993.

[56] J. K. Solberg, *Teknologiske metaller og legeringer*. Trondheim: Institutt for materialteknologi, 2017.

[57] Y. A. Dobrovol'skii, A. E. Ukshe, A. V. Levchenko, I. V. Arkhangel'skii, S. G. Ionov, V. V. Avdeev, and S. M. Aldoshin, "Materials for bipolar plates for proton-conducting membrane fuel cells," *Russian Journal of General Chemistry*, vol. 77, pp. 752–765, 4 2007.

[58] C. K. Jin, M. G. Jeong, and C. G. Kang, "Fabrication of titanium bipolar plates by rubber forming and performance of single cell using TiN-coated titanium bipolar plates," *International Journal of Hydrogen Energy*, vol. 39, pp. 21480–21488, 12 2014.

[59] Lide D. R., *CRC Handbook Chemistry and Physics*. CRC Press, 1994.

[60] Z. H. Cen, B. X. Xu, J. F. Hu, R. Ji, Y. T. Toh, K. D. Ye, and Y. F. Hu, "Temperature effect on titanium nitride nanometer thin film in air," *Journal of Physics D: Applied Physics*, vol. 50, p. 075105, 2 2017.

[61] M. N. Solovan, V. V. Brus, E. V. Maistruk, and P. D. Maryanchuk, "Electrical and optical properties of TiN thin films," *Inorganic Materials*, vol. 50, pp. 40–45, 1 2014.

[62] H. Husby, "Carbon composite coatings for metallic bipolar plates," 2012.

[63] E. Bardal, *Korrosjon og Korrosjonsvern*. Trondheim: Tapir Akademisk Forlag, 1994.

[64] K. Nisancioglu, *Corrosion basics and engineering*. Trondheim: NTNU.

[65] Z. Szklarska-Smialowska, "Pitting corrosion of aluminum," *Corrosion Science*, vol. 41, pp. 1743–1767, 8 1999.

[66] H. Wang, "Stainless steel as bipolar plate material for polymer electrolyte membrane fuel cells," *Journal of Power Sources*, vol. 115, 4 2003.

[67] G. Hinds and E. Brightman, "Towards more representative test methods for corrosion resistance of PEMFC metallic bipolar plates," *International Journal of Hydrogen Energy*, vol. 40, pp. 2785–2791, 2 2015.

[68] J. Hjelen, *Scanning elektron-mikroskopi*. Trondheim: SINTEF, 1989.

[69] J. I. Goldstein, D. E. Newbury, P. Echlin, D. C. Joy, C. E. Lyman, E. Lifshin, L. Sawyer, and J. R. Michael, "The SEM and Its Modes of Operation," in *Scanning Electron Microscopy and X-ray Microanalysis*, Boston, MA: Springer US, 2003.

[70] "*Matweb: 1080 Aluminium Composition Spec.*" `https://www.matweb.com/search/datasheet.aspx?matguid=8a8ea4665b034127a0dbfbe798cd5c3a&ckck=1`, accessed: 19.01.2022.

[71] S. Lædre, O. E. Kongstein, A. Oedegaard, F. Seland, and H. Karoliussen, "Measuring In Situ Interfacial Contact Resistance in a Proton Exchange Membrane Fuel Cell," *Journal of The Electrochemical Society*, vol. 166, pp. F853–F859, 8 2019.

[72] D.-H. Han, W.-H. Hong, H. Choi, and J. Lee, "Inductively coupled plasma nitriding of chromium electroplated AISI 316L stainless steel for PEMFC bipolar plate," *International Journal of Hydrogen Energy*, vol. 34, pp. 2387–2395, 3 2009.

[73] T.-M. Wen, K.-H. Hou, C.-Y. Bai, M.-D. Ger, P.-H. Chien, and S.-J. Lee, "Corrosion behaviour and characteristics of reforming chromized coatings on SS 420 steel in the simulated environment of proton exchange membrane fuel cells," *Corrosion Science*, vol. 52, pp. 3599–3608, 11 2010.

[74] S. Jannat, H. Rashtchi, M. Atapour, M. A. Golozar, H. Elmkhah, and M. Zhiani, "Preparation and performance of nanometric Ti/TiN multi-layer physical vapor deposited coating on 316L stainless steel as bipolar plate for proton exchange membrane fuel cells," *Journal of Power Sources*, vol. 435, p. 226818, 9 2019.

[75] Y. Yang, L.-j. Guo, and H. Liu, "Corrosion characteristics of SS316L as bipolar plate material in PEMFC cathode environments with different acidities," *International Journal of Hydrogen Energy*, vol. 36, pp. 1654–1663, 1 2011.

[76] L. Wang, J. Sun, P. Li, B. Jing, S. Li, Z. Wen, and S. Ji, "Niobized AISI 304 stainless steel bipolar plate for proton exchange membrane fuel cell," *Journal of Power Sources*, vol. 208, pp. 397–403, 6 2012.

[77] K. M. Kim, J. H. Kim, Y. Y. Lee, and K. Y. Kim, "Electrodeposition of ruthenium oxide on ferritic stainless steel bipolar plate for polymer electrolyte membrane fuel cells," *International Journal of Hydrogen Energy*, vol. 37, pp. 1653–1660, 1 2012.

[78] O. Lunder, B. Olsen, and K. Nisancioglu, "Pre-treatment of AA6060 aluminium alloy for adhesive bonding," *International Journal of Adhesion and Adhesives*, vol. 22, pp. 143–150, 1 2002.

[79] F. Ashrafizadeh, "Adhesion evaluation of PVD coatings to aluminium substrate," *Surface and Coatings Technology*, vol. 130, pp. 186–194, 8 2000.

Appendix A

Electrolyte Calculations

Electrochemical experiments were performed in 0.1 M Na_2SO_4 electrolyte. The electrolyte solution was prepared in a 3 L measuring flask. To make a solution with volume, V, and a given concentration, c, the number of moles, n, is calculated by Eq. A.1

$$n = c \cdot V. \tag{A.1}$$

When $V = 3$ L and $c = 0.1$ mol L^{-1}, the number of moles needed is

$$n = 0.1 \text{ mol } L^{-1} \cdot 3 \text{ L} = 0.3 \text{ mol}.$$

The mass in grams, m, is given by Eq. A.2

$$m = Mm \cdot n, \tag{A.2}$$

where Mm is the molar mass.

The molar mass of sodium sulphate is 142.04 g mol^{-1}. Thus,

$$m = 142.04 \text{ g mol}^{-1} \cdot 0.3 \text{ mol} = 42.612 \text{ g},$$

42.612 g Na_2SO_4 was added to 3 L deionised water and mixed.

Appendix B

Contact Resistance

The measured voltage when applying compaction pressures varying from 33 - 250 N cm^{-2} while passing a constant current of 1.5 A through the sample, was used to calculate the interfacial contact resistance and plotted as a function of applied pressure. The ICR plotted as a function of compaction pressure for the aluminium sample coated with 20 nm TiN (sample no. 34), before and after corrosion tests, is shown in Figure B.1 as an example. This was done for all samples and the reported values, given in tables, in Chapter 4 were 140 Ncm^{-2} as marked in the figure.

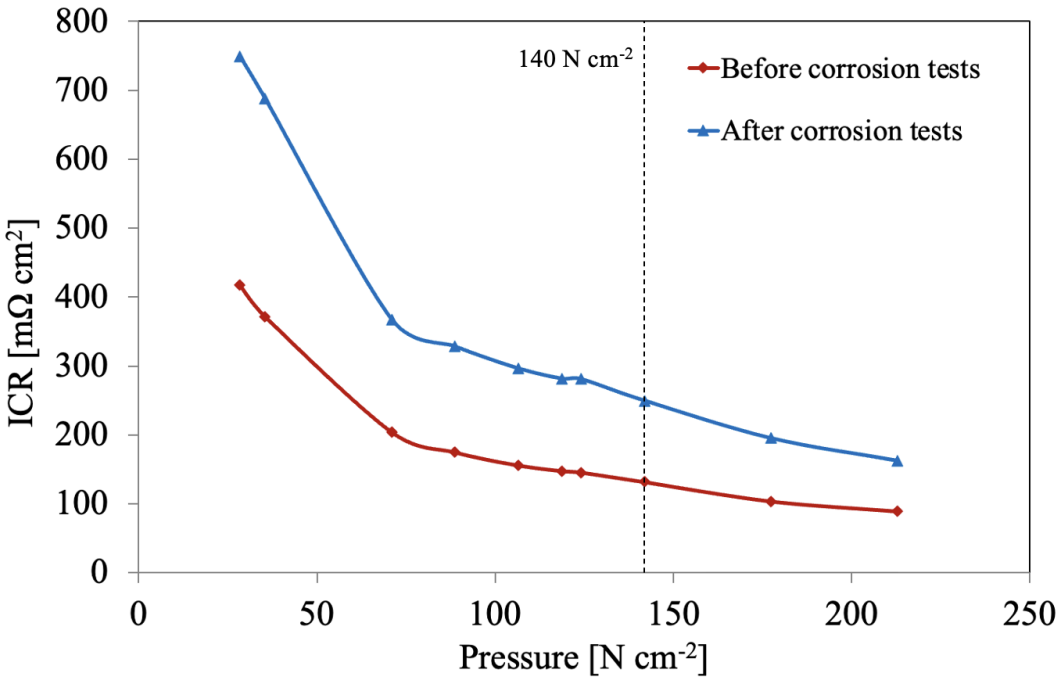

Figure B.1: Interfacial contact resistance plotted as a function of applied compaction pressure for the aluminium sample coated with 20 nm TiN, before and after corrosion tests were performed.

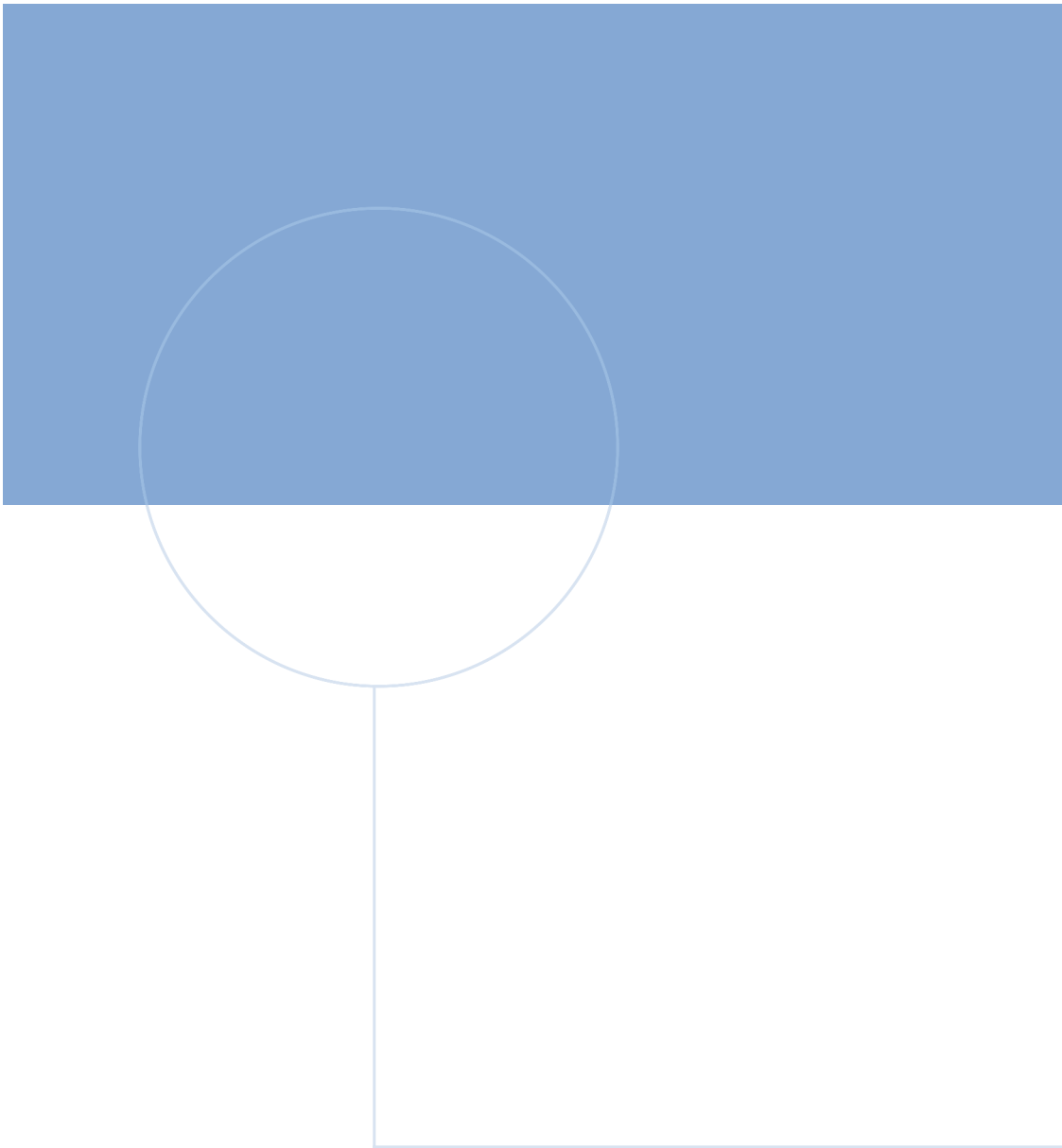

NTNU

Norwegian University of
Science and Technology